Magnetic properties of individual iron filled carbon nanotubes and their application as probes for magnetic force microscopy

Dissertation

zur Erlangung des akademischen Grades
Doctor rerum naturalium (Dr. rer. nat.)

vorgelegt der Fakultät Mathematik und Naturwissenschaften
der Technischen Universität Dresden von

Diplom-Naturwissenschaftlerin Franziska Wolny

geboren am 14.03.1980 in Karl-Marx-Stadt

Die Dissertation wurde in der Zeit vom 01.09.2006 bis 31.10.2010 am
Leibniz-Institut für Festkörper- und Werkstoffforschung (IFW)
Dresden angefertigt.

1. Gutachter:
Prof. Dr. B. Büchner, Technische Universität Dresden

2. Gutachter:
Prof. Dr. P. C. Hammel, Ohio State University

eingereicht am 16.12.2010

Tag der Verteidigung 09.06.2011

Table of Contents

Table of contents 5

Recurring abbreviations and symbols 9

List of Figures 11

Introduction and motivation 14

1 Introduction to carbon nanotubes 19

- 1.1 Structure and properties of carbon nanotubes . . . 19
- 1.2 Synthesis of carbon nanotubes . . . 22
- 1.3 Filled carbon nanotubes . . . 23

2 Review of the magnetism of iron nanowires 25

- 2.1 Relevant aspects of ferromagnetism . . . 25
  - 2.1.1 Energetic considerations . . . 26
  - 2.1.2 Magnetic domains . . . 29
  - 2.1.3 Magnetic hysteresis . . . 31
- 2.2 Properties of iron . . . 33
- 2.3 Magnetic properties of ensembles of ferromagnetic nanowires . . . 34

3 Methods 37

- 3.1 FeCNT growth by chemical vapor deposition . . . 37
- 3.2 Electron microscopy . . . 39
  - 3.2.1 Scanning electron microscopy . . . 39
  - 3.2.2 Focused ion beam . . . 40
  - 3.2.3 Transmission electron microscopy . . . 40
- 3.3 Scanning probe microscopy . . . 41
  - 3.3.1 Fundamental principles of scanning probe microscopy . . . 41
  - 3.3.2 Dynamic mode scanning probe microscopy . . . 44
  - 3.3.3 Introduction to magnetic force microscopy . . . 46

3.3.3.1 Quantitative magnetic force microscopy 48
3.3.3.2 The point probe approximation 51
3.3.3.3 Approaches for alternative kinds of MFM probes . . . 53

4 Magnetic properties of individual FeCNT 57
4.1 MFM investigations of individual FeCNT 58
4.1.1 Sample preparation 58
4.1.2 MFM measurement 59
4.1.3 Determination of the switching field of individual FeCNT 60
4.1.4 Combined TEM and MFM investigations on a FeCNT 62
4.1.5 Creation of a domain wall in a FeCNT 63
4.2 Cantilever magnetometry measurements of an individual FeCNT 66

5 FeCNT as probes for MFM 73
5.1 Preliminary considerations on MFM probes 73
5.2 Probe preparation 76
5.2.1 Attachment of an individual FeCNT to a conventional AFM probe 76
5.2.2 Tailoring fabricated tips with a focused ion beam 78
5.2.3 Tailoring fabricated tips by localized electron-beam induced oxidation 79
5.3 MFM measurements with FeCNT MFM probes 81
5.4 Magnetic resolution of FeCNT MFM probes 84
5.5 Behavior of FeCNT MFM probes in external magnetic fields 85
5.5.1 Experimental procedure 86
5.5.2 In-plane field MFM measurement results 87
5.5.3 Micromagnetic simulation of an iron nanowire in external fields 89

6 Calibration of FeCNT probes for quantitative MFM 93
6.1 Calibration device 93
6.1.1 Device design 93
6.1.2 Device fabrication by electron beam lithography 96
6.1.3 Current voltage characteristic of the parallel gold line structures 98
6.2 Influence of electrostatic forces on the measured phase shift signal . . . 100
6.3 Calibration of a conventional MFM probe 102
6.4 Calibration of a FeCNT MFM probe 105
6.5 Calibration of a FeCNT probe using multilayer stripes 108
6.6 Application of the calibration results for quantitative MFM 110
6.7 Quantitative MFM on permalloy dots using a FeCNT probe 112
6.7.1 Probe calibration 112

6.7.2 Quantitative MFM data evaluation 116
6.7.3 Evaluation of the FeCNT field gradient 118

Summary and outlook **121**

Bibliography **125**

List of Publications **137**

Acknowledgements **139**

RECURRING ABBREVIATIONS AND SYMBOLS

AFM	atomic force microscope
BSED	back-scattered electron detector
CCD	charge-coupled device
CNT	carbon nanotube
CVD	chemical vapor deposition
EBL	electron beam lithography
FeCNT	iron filled carbon nanotube
FIB	focused ion beam
MFM	magnetic force microscope
MRFM	magnetic resonance force microscope
MWCNT	multi-walled carbon nanotube
SEM	scanning electron microscope
SPM	scanning probe microscope
SWCNT	single-walled carbon nanotube
TEM	transmission electron microscope

symbol	**description**	**unit**
A	exchange stiffness constant	J/m
b	distance between the two parallel lines of the calibration structure	m
B	magnetic flux density	T
d	distance of the point monopole from the MFM tip apex	m
f	cantilever resonance frequency	Hz
H	magnetic field	A/m
H_c	coercive field	A/m
H_k	anisotropy field	A/m
I	current	A
j	current density	$\mathrm{A/m^2}$
k	cantilever spring constant	N/m
K	anisotropy energy	$\mathrm{J/m^3}$
K_n	n-th uniaxial anisotropy constant	$\mathrm{J/m^3}$
K_s	shape anisotropy energy	$\mathrm{J/m^3}$
m	magnetic dipole moment	$\mathrm{A\,m^2}$
M	magnetization	A/m
M_s	saturation magnetization	A/m
q	magnetic monopole moment	A m
Q	cantilever quality factor	
$\Delta\Phi$	phase shift of the cantilever oscillation	degrees
ω	angular frequency	rad/s
μ_0	magnetic constant (permeability of free space)	$\mu_0 = 4\pi \cdot 10^{-7}\,\mathrm{N/A^2}$
k_B	Boltzmann constant	$k_B = 1,38 \cdot 10^{-23}\,\mathrm{J/K}$

LIST OF FIGURES

1.1 Structure of a carbon nanotube. 20
1.2 Schematic drawing of a two stage CVD furnace for the fabrication of FeCNT from ferrocene. 23
1.3 Schematic showing a possible growth mechanism for iron filled carbon nanotubes from ferrocene as a precursor. 24

2.1 Origin of the magnetic shape anisotropy. 28
2.2 Reduction of the magnetostatic energy by the formation of domains. . . 30
2.3 Sketch of a typical hysteresis loop. 31
2.4 Schematic hysteresis loop $M(H)$ for different angles θ between the external field and the easy axis of a single domain particle. 32
2.5 Coercivity of ferromagnetic nanowires. 35

3.1 SEM micrographs of FeCNT produced by thermal CVD. 38
3.2 TEM micrographs of individual FeCNT. 38
3.3 Kleindiek micromanipulator setup in a SEM. 40
3.4 Schematic showing the principle of a scanning probe microscope and a force vs. distance curve. 42
3.5 Schematic resonance curve of a harmonic oscillator and its shift due to attractive or repulsive forces. 46
3.6 Nanoscan hr-MFM. 47
3.7 Topography and magnetic contrast of a magnetic hard disk. 48
3.8 Schematic showing the interaction between a magnetic probe and longitudinal recording media. 49
3.9 Schematic sketch of the point probe model. 52
3.10 Schematic showing different MFM probe designs. 54

4.1 Hysteresis curve of an ensemble of FeCNT. 57
4.2 Gold markers facilitate the orientation on a silicon substrate. 58
4.3 SEM and MFM image of a partially filled FeCNT. 59

4.4 Series of MFM images taken after applying an increasing magnetic field antiparallel to the original iron wire magnetization. 60
4.5 MFM study of FeCNT embedded in a polymer. 61
4.6 Parallel TEM and MFM investigations on the same FeCNT. 62
4.7 SEM and MFM image of a long single domain FeCNT. 64
4.8 Introduction of a domain wall in a FeCNT by bending and applying an external magnetic field. 65
4.9 Sample preparation for cantilever magnetometry. 67
4.10 Frequency shift hysteresis loop for a FeCNT attached to a cantilever. . 68
4.11 Temperature dependent switching behavior of a FeCNT. 69

5.1 Schematic comparison between a magnetically coated MFM probe and an extended dipole probe. 74
5.2 SEM micrographs of FeCNT MFM probes. 77
5.3 TEM micrograph of a FeCNT attached to a silicon cantilever. 77
5.4 FeCNT cut with the FIB. 79
5.5 Localized electron-beam assisted etching of a FeCNT. 80
5.6 Removal of the empty carbon shell at the end of a FeCNT. 81
5.7 MFM test of four different FeCNT MFM probes. 82
5.8 High resolution MFM scan of a magnetic hard disc made with a FeCNT MFM probe. 84
5.9 MFM scan of iron nanoparticles made with a FeCNT MFM probe. . . . 85
5.10 Sample and probes used for the in plane field MFM measurements. . . 87
5.11 MFM scans of the Co/CoO nanodots taken at the different values of the external magnetic field. 88
5.12 Micromagnetic simulation of the hysteresis curve of a FeCNT probe. . . 91

6.1 Schematic drawing of parallel current carrying lines. 94
6.2 SEM micrograph of contact pads and parallel gold lines produced by EBL. 96
6.3 SEM images of parallel gold lines produced by EBL. 97
6.4 AFM images of parallel gold lines produced by EBL. 98
6.5 Electrical circuit to protect the gold lines from electrostatic potentials. 98
6.6 Current-voltage curve of parallel gold lines. 99
6.7 Topography image and MFM scan of two parallel lines carrying current I. 100
6.8 Shielding of the electrostatic interaction. 101
6.9 Bias sweep to determine the sample surface potential. 102
6.10 Line scans at different heights above the sample surface across two current carrying lines with b=630 nm. 103

6.11 Phase shift vs. height curves measured with a coated MFM probe for different line separations b. 104
6.12 Phase shift vs. height curves measured with a FeCNT MFM probe for different line separations b. 106
6.13 Comparison of the fitted monopole moment and its position for a conventional probe and a FeCNT probe. 107
6.14 Schematic of $(\mathrm{Co/Pt})_7$ stripes with varying width used for the MFM probe calibration to investigate the dependence of the probe parameters on the domain size. 108
6.15 MFM measurement and fitted curves of a $(\mathrm{Co/Pt})_7$ stripe performed with a conventional MFM probe and a FeCNT MFM probe. 109
6.16 Fitted probe monopole moment q and its position d for a conventional probe and a FeCNT probe in comparison with literature values. 110
6.17 MFM measurement and simulation of a (Co/Pt)/Ru multilayer. 111
6.18 SEM images of the FeCNT probes in use and schematic of the monopole model. 113
6.19 MFM images and simulation of a Py disk in different probe sample distances. 114
6.20 MFM response and simulation for two different FeCNT probes at different probe sample distances z. 117
6.21 Magnetic field gradient near the Py dot measured at different probe-sample distances using FeCNT probe J2. 118
6.22 Effective and theoretical magnetic field gradient close to the tip of FeCNT J2. 119

INTRODUCTION AND MOTIVATION

Since several years there is growing interest in the synthesis and properties of magnetic nanoparticles because of the wide range of possible applications. Due to their nanoscale dimensions such particles and wires have great potential for the development of magnetic recording media with increased storage density.[1,2] Another interesting field of application is the medical sector. Magnetic nanoparticles are already used as contrast agent for magnetic resonance imaging.[3] Carbon nanostructures filled with magnetic material can be used for hyperthermia treatment of cancer and provide an alternative to chemotherapy.[4,5] Furthermore, magnetic nanostructures constitute interesting materials for new sensors.[6,7]

Carbon nanotubes can be thought of as formed by a single or multiple concentric rolled up graphene layers with diameters from 1 to 150 nm. They posses extraordinary properties. Their elastic modulus was found to be in the order of 1TPa which is the highest measured for any material so far. The nanotube's aspect ratio (length:diameter) of 10 to 1000 and more depending on the synthesis method is one of the reasons that CNT are attractive as possible sensors for scanning probe techniques. It has already been shown[8] that carbon nanotubes reveal great potential as probes for atomic force microscopy (AFM).

Carbon nanotubes filled with a ferromagnetic material (e.g. iron filled carbon nanotubes, FeCNT) combine the interesting properties of **nanoscaled magnets** and mechanically stable carbon nanotubes. They can be grown with a high filling ratio via chemical vapor deposition (CVD) and their properties can be adjusted to some extent by varying the growth conditions. The magnetic properties of the enclosed nanowire are in part determined by its small size and elongated shape. The carbon shells act as a protective container for the magnetic filling preventing oxidation and mechanical damage. Thus the magnetic properties of the filling remain unchanged for a long time enabling possible applications as sensors or actuators. For these purposes, the magnetic properties of these structures need to be investigated in detail. Since the synthesis of FeCNT yields a distribution of filling lengths and diameters with different resulting magnetic properties, such as switching fields and domain formation, it is not always possible to derive the properties of an individual FeCNT from magnetic bulk measurements. For this purpose methods like micro-Hall or micro-SQUID magnetometry need to be applied.[9] A popular method to obtain spatially resolved information on the magnetic properties of magnetic nanostructures is **magnetic force microscopy** (MFM). MFM is a scanning probe technique used to image the magnetic stray field perpendicular to a sample's surface.[10,11] It is employed in industry as well as in research and development to investigate the magnetic properties of, e.g., magnetic recording media,[12] magnetic nanostructures[13] and magnetic thin film structures[14]. With high aspect ratio probes, it is currently possible to achieve a high lateral magnetic resolution of up to 10 nm.[15]

In this work, magnetic force microscopy will be used to investigate the magnetic properties of individual FeCNT. It can give insight into the nanowire's magnetic domain structure, and by performing MFM while or after applying a defined external magnetic field it is possible to determine the magnetic switching fields of individual iron nanowires. Furthermore, the MFM tip or a suitable AFM tip can be used to bend the nanowire and observe the influence of the changed shape on the magnetic behavior. The second part of this work will focus on the fabrication and application of FeCNT themselves as probes for MFM. It will be shown that these probes exhibit several advantages compared to conventional probes.

MFM probes usually consist of a conventional scanning force microscopy probe (a silicon or silicon nitride cantilever with a sharp pyramidal tip at its front end), which is covered by several nanometers of hard magnetic material. The magnetic coating is then magnetized along the pyramid axis, leading to an interaction between the tip's magnetic moment and the sample stray field. This arrangement is relatively easy to fabricate and yields good MFM images, but it also has several disadvantages. The metallic coating is subject to oxidation, which makes it necessary to store the probes in a vacuum or apply a protective layer. Furthermore, the magnetic coating can easily be damaged when scanning the sample surface. For magnetic imaging applications, an additional disadvantage is that the active magnetic volume of the tip coating has a complex shape. Because of this, the effective magnetic tip coating involved in the tip-sample-interaction depends on the geometry of the sample stray field.[16–18] This makes it hard to **quantitatively** evaluate the MFM data. Moreover, additional moments along the sides of the pyramid reduce the achievable **magnetic resolution**. All these aspects lead to the conclusion that the ideal MFM probe would have a sharp tip and a high aspect ratio for good topographic imaging, great mechanical strength, oxidation protection, and a defined magnetic moment perpendicular to the sample surface. The latter might be a dipole moment spatially confined in three dimensions or a monopole moment given by a nanowire (i.e., confined in two dimensions). Iron-filled carbon nanotubes exhibit all of these mentioned properties, which makes them excellent candidates for MFM tips. Other nano-objects like magnetically-coated nanotubes[19] or spherical magnetic particles[20] have already been used for MFM imaging. However, the elongated, cylinder-like iron nanowires contained in the carbon nanotubes have the advantage that they form very defined dipoles. To a close approximation, only the monopole at the end of the nanowire that is close to the surface interacts with the sample stray field. This creates the possibility of **straightforward quantitative MFM measurements** that are independent of the sample stray field geometry.

This thesis is divided into six chapters. The first chapter will briefly discuss selected properties of carbon nanotubes. Some basic concepts of magnetism in the nano- and microscale are presented in chapter two. In the third chapter, the characterization and fabrication methods used are described with the focus on scanning force microscopy. Results on the magnetic properties of individual carbon nanotubes obtained by MFM and cantilever magnetometry are discussed in chapter four. In the fifth chapter it will be shown how iron filled carbon nanotubes can be applied as sensors for MFM. Results on the calibration of such FeCNT MFM sensors for quantitative MFM measurements will be presented in chapter six.

1 Introduction to carbon nanotubes

Carbon nanotubes (CNT) present an additional modification of carbon next to diamond, graphite (graphene) and fullerenes. The unique mechanical, electrical and chemical properties of CNT have attracted much interest since their discovery in 1991.[21] The intrinsic properties as well as the possibility for a large variety of functionalizations lead to a multitude of potential applications. The main focus of this work is on the properties of the ferromagnetic filling of carbon nanotubes. Nevertheless the main characteristics of CNT themselves will be presented in this chapter as well.

1.1 Structure and properties of carbon nanotubes

Carbon nanotubes can be described as hollow cylinders of carbon with a diameter in the nanometer range and a length that can vary from nanometers to centimeters depending on the synthesis method. The resulting aspect ratio (length:diameter) can take values anywhere from 10 to 10^8 which is significantly larger than what can be achieved with any other material.[22] This gives already a first impression of the unique properties of this fascinating nanostructure. The structure of a CNT can be derived from the graphite structure by imagining a graphene sheet (graphene being one two-dimensional layer of carbon atoms in graphite) that is rolled up to a cylindrical form. Nanotubes composed of only one of such cylinders are called single-walled carbon nanotubes (SWCNT). The nanotube ends often have the shape of fullerene-like caps (Fig. 1.1). The carbon atoms in a graphene layer are sp^2 hybridized, two $2p$ orbitals mix with the $2s$ orbital of atomic carbon. This results in three coplanar orbitals with a 120° angle between them that create strong σ bonds between the hexagonally arranged carbon atoms. The remaining $2p$ orbital is oriented perpendicular to this plane and forms the π bond (double bonds) between every second pair of carbon atoms.

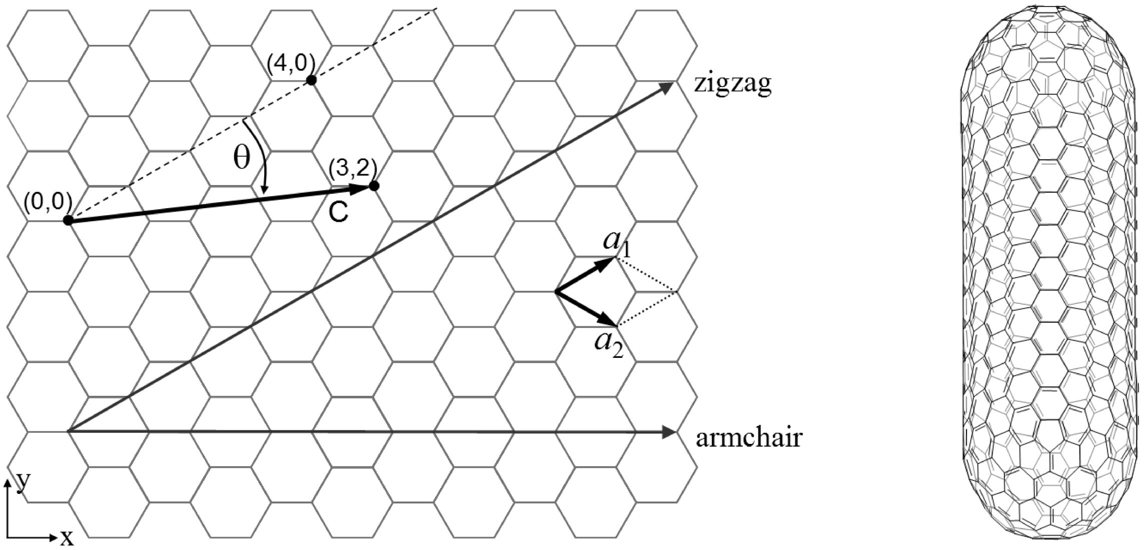

Figure 1.1: Left: Hexagonal lattice of a graphene sheet. The unit vectors a_1 and a_2 define the unit cell which contains two carbon atoms. **C** is the chiral vector and θ the chiral angle that define the structure of each SWCNT. The special types zigzag and armchair are shown by arrows. Right: Sketch of a single walled CNT.

The structure of a single walled CNT can be described by the chiral vector **C**, a vector between two crystallographically equivalent sites of the graphene lattice:

$$\mathbf{C} \; = n\mathbf{a}_1 + m\mathbf{a}_2 =: (n, m) \tag{1.1}$$

$\mathbf{a}_1$ and $\mathbf{a}_2$ denote the unit vectors of the two-dimensional lattice, n and m are integers.[23] The unit cell thus contains two carbon atoms (two-atomic base). The tube is formed by rolling up the graphene sheet such that two points connected by the chiral vector coincide (Fig. 1.1). A pair (n, m) or the chiral vector θ defines a SWCNT of a certain chirality. The zigzag structure corresponds to each pair $(n, 0)$ and a chiral angle of 0°, armchchair CNT are defined by the indices (n, n) and the maximum possible angle θ=30° ($n \neq 0$). All cases in between are the so-called chiral SWCNT. The diameter of the resulting nanotube is given by

$$d_{SWCNT} = \frac{|\mathbf{C}|}{\pi} = \frac{a\sqrt{n^2 + 2nm + m^2}}{\pi} \tag{1.2}$$

where $a = \sqrt{3} \cdot 1.42\,nm = 2.46\,nm$ is the lattice constant of graphene with the distance between two carbon atoms being 1.42 nm.

The electronic properties of SWCNT can be deduced from the energy dispersion of graphene. In graphene, the valence and conduction bands touch at the six K points in the hexagonal two-dimensional Brillouin zone creating a zero-gap semiconductor.

In the case of SWCNT, the band structure depends strongly on the chiral vector **C** of the individual nanotube. A simple equation can predict the behavior of a specific SWCNT:

$$n - m = 3N \tag{1.3}$$

where N is an integer.[24] If this relation is true, the nanotube is metallic (e.g., armchair CNT), otherwise it is semiconducting. A SWCNT can be regarded as a nearly perfect one-dimensional electronic conductor enabling many potential applications such as nanotube based transistors.[25] During SWCNT synthesis, all chiralities are produced leading to mixed samples of metallic and semiconducting nanotubes.[23]

Carbon nanotubes exhibit a tremendous mechanical and chemical stability. The elastic modulus can be in the order of 1 TPa depending on the synthesis method. Additionally, CNTs can be bent, elongated or compressed to a large extend without fracture. In most cases, the CNT goes elastically back to its original shape.[26] Their extraordinary strength and elasticity make CNT an ideal ingredient for very robust composite materials.

Multi-walled carbon nanotubes (MWCNT) are composed of two or more coaxial carbon cylinders with intershell coupling between neighboring shells. The cylinders are spaced like the individual graphene layers in graphite (3.4 Å). The resulting MWCNT diameter can range from several nm up to more then 100 nm. The above mentioned properties are shared by SWCNT and MWCNT to a large extent. However, the electronic properties of MWCNT depend strongly on the structure of the specific sample. MWCNTs are theoretically predicted to be metallic. Experimentally, both ballistic and diffusive electron transport have been reported.[27,28] With an increasing number of shells, most often combined with a larger amount of defects, the diffusive transport mechanism dominates.

Several experimental techniques to determine the elastic modulus of MWCNT have been developed, it is most often found to be lower than in the case of SWCNT. Poncharal et al. observed static and dynamic deflections of MWCNT through an electrostatic excitation.[29] The elastic bending modulus was found to decrease sharply from about 1 to 0.1 TPa when the MWCNT's diameter increases from 8 nm to 40 nm. This is on the one side due to wavelike distortions during the nanotube bending, on the other side thicker MWCNT often contain more defects which reduce the mechanical stiffness. This result was confirmed by the experiments of Lee et al.[30] who used force-displacement curves recorded in an atomic force microscope for stiffness measurements. The elastic modulus showed a difference of nearly two orders of magnitude for a doubled MWCNT diameter. Nevertheless the nanotube's stiffness is still larger or at least comparable to other materials like steel (200 GPa) or silicon (100 GPa).

1.2 SYNTHESIS OF CARBON NANOTUBES

Carbon nanotubes can be synthesized using a multitude of techniques. One of the most popular is the arc-discharge method which uses a high temperature (>2000°C) discharge between two graphite electrodes to sublimate the carbon.[31] The result is a complex mixture of SWCNT, MWCNT, amorphous carbon and graphite which requires further purification. In the laser ablation technique, a rod composed of a graphite/catalyst mixture is vaporized by a laser pulse.[32] It yields primarily bundles of SWCNT.

The most promising technique for a large-scale production of CNT is chemical vapor deposition (CVD) using hydrocarbon precursors. Carbon-containing gases such as methane, ethane or acetylene are catalytically decomposed at the surface of metal particles at reaction temperatures of 500-1200°C.[23,33] The spectrum of possible catalyst materials is very broad, iron, cobalt and nickel are among the most often used.[34] The catalytic action of the metal leads to the controlled growth of carbon nanotubes. Despite extensive experimental and theoretical studies on the subject, the growth mechanism is still not completely understood. The most popular growth model suggests that carbon in the gas phase is dissolved in the liquid catalyst particles until saturation is reached. The excess carbon is then segregated at the particle surface in the form of fullerene-like caps that develop into nanotubes.[35] This process is controlled by the diffusion of carbon within the catalyst particle. Process parameters such as temperature, pressure, gas flow rate, reactor geometry, catalyst particle size and of course the type of hydrocarbon and catalyst material crucially influence the structure of the resulting carbon nanotube. By choosing the appropriate growth conditions, length, thickness and morphology of the CNT product can be controlled to a certain extent. In general, a mixture of MWCNT of varying diameter is much more easily to synthesize than their single-walled counterparts.

While the laser ablation and arc-discharge method yield a loose powder of CNT, CVD can be used to grow "‘forest-like"’ oriented layers of nanotubes on a substrate. A popular arrangement is to use metal-coated silicon wafers. At the high reaction temperatures, the coating layer breaks up into small particles which then act as nanotube nucleation sites as described earlier. The simultaneous growth of nanotubes with a large density on the substrate surface leads to a reduction of the degrees of freedom during growth and a mutual support and alignment.[36] This effect can be enhanced by applying an electric field during growth.[37] In plasma enhanced CVD, a high frequency electric field is used to ionize the carrier gas. The resulting electric field perpendicular to the substrate surface strongly enhances the nanotube alignment.[38]

1.3 Filled carbon nanotubes

In the last years there was an increasing interest in filling different materials into the hollow core of carbon nanotubes. Due to their nanoscale size, carbon nanotubes filled with ferromagnetic materials are considered to have potential applications in various fields reaching from sensor devices to medical treatments. In addition, the carbon shells provide an effective barrier against oxidation and consequently ensure a long-term stability of the ferromagnetic core.

Various methods for the filling of carbon nanotubes have been explored including capillary infiltration using wet-chemical techniques,[39] arc discharge[40] and chemical vapor deposition.[34] Among these, CVD is again the most promising technique to produce filled carbon nanotubes in large quantities for low cost industrial applications. The thermal decomposition of ferrocene combined with a catalyst-coated substrate surface is a favorable way to produce aligned iron filled carbon nanotubes (FeCNT) in a good quality with high yields. Ferrocene ($Fe(C_5H_5)_2$) is an organometallic chemical "sandwich" compound consisting of a central iron atom coordinated by two cyclopentadienyl rings on opposite sides. During the FeCNT synthesis, ferrocene acts both as a source for carbon and iron. Fig. 1.2 shows a schematic drawing of a two stage CVD furnace for the fabrication of FeCNT from ferrocene. In the first hot zone which is kept at ~180°C, ferrocene is sublimated and subsequently carried by a noble gas stream to the second hot zone where the molecule is decomposed at temperatures of ~600-1000°C. To enable an aligned growth of FeCNT, a silicon substrate coated with a couple of nanometers of iron catalyst is used. The metal layer breaks up into semi-liquid is-

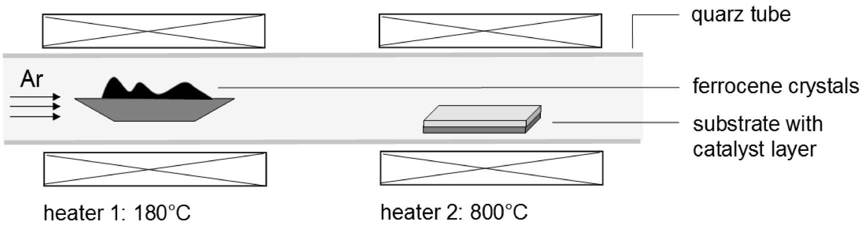

Figure 1.2: Schematic drawing of a two stage CVD furnace for the fabrication of FeCNT from ferrocene. The carrier gas Ar transports the sublimated ferrocene from the sublimation zone into the reaction zone.

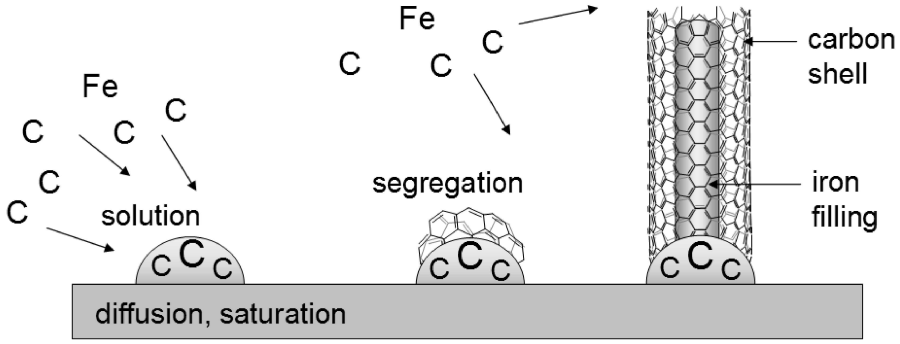

Figure 1.3: Schematic showing a possible growth mechanism for iron filled carbon nanotubes from ferrocene as a precursor.

lands upon heating on which the ferrocene molecules can decompose more easily due to the catalytic action. The growth process then resembles the mechanism described in the previous section, but now the iron which is present in the furnace atmosphere is incorporated into the CNT during growth (Fig. 1.3). This leads to the growth of multi-walled CNT filled with iron nanowires. The nanotube length, the diameter of the iron filling and the filling ratio can by varied to a certain extent by adjusting the CVD process parameters. These include the furnace temperature, the gas flow rate, the substrate position in the furnace and the amount of precursor material used. However, the growth of FeCNT is not as easy to control as for hollow CNT since the catalyst material (iron) is also present in the gas phase, not only on the substrate. This can lead to a deposition of FeCNT or carbon coated iron particles all over the furnace or on already grown nanotubes. The details of the CVD process used to fabricate the FeCNT in this work will be explained in more detail in section 3.1.

2 Review of the magnetism of iron nanowires

Magnetic nanostructures are a technologically relevant area of research with many possible applications in magnetic recording, sensing and spin electronics.[41] In addition, they are scientifically interesting as they can be considered as model systems to study magnetic reversal and interaction processes in low-dimensional magnetic structures. Recent research has led to a broad variety of low-dimensional systems such as nanoparticles, nanowires, nanodots and antidot structures.[42] Among these, ferromagnetic nanowires exhibit unique and tunable magnetic properties that are very different from those of bulk ferromagnets, thin films or spherical particles.[43] Some of these properties will be highlighted in this chapter.

2.1 Relevant aspects of ferromagnetism

Magnetism can arise from two different origins, the orbital motion of the electron and the electron spin of incompletely filled orbitals. In metals like Fe, Co or Ni, the magnetic moment m is largely given by the spin. If there is a non-zero magnetic moment in the atom, an external magnetic field H tends to orient the intrinsic atomic magnetic moment along its own direction. The resulting positive moment parallel to the field is the Langevin paramagnetic moment. The magnetization M of the material is defined as the magnetic moment per unit volume. An external field can only align the moments of a paramagnet very weakly. Already at room temperature the thermal energy is large relative to the magnetic energy.[42,44,45]

Much stronger effects can arise from the exchange interaction between atomic moments. In some materials, the formation of an atomic magnetic ordering is energetically favorable. This ordering can be stable even in the absence of an external field. If the atomic moments are aligned parallel within spatial domains, the material is ferromagnetic. In that case, the alignment of all atomic moments leads to a saturation magnetic moment. The effect of the exchange interaction can be expressed in terms of an exchange field whose magnitude is often much larger than that of an external field. As mentioned before, the alignment due to the exchange field can be disturbed by a thermal excitation of the moments. Above a certain temperature (Curie temperature T_C) the spin order and thus the spontaneous magnetization is destroyed, the sample changes to the paramagnetic state.

2.1.1 Energetic considerations

The local magnetization $\mathbf{M}(\mathbf{r})$ of a magnetic material is determined by its magnetic energy $E(\mathbf{M}(\mathbf{r}))$. It can be obtained by finding the minima of E as a function of the external field H. There are four main contributions to the magnetic energy, the exchange energy E_{ex}, the magnetocrystalline anisotropy energy E_{mc}, the magnetostatic energy (shape anisotropy) E_D and the Zeeman energy E_Z:[42,44,46]

$$E = E_{ex} + E_{mc} + E_D + E_Z \tag{2.1}$$

The short-range **exchange interaction** is a quantum mechanical effect which can lead to an alignment of neighboring spins. It is the main cause for a long range magnetic order and can be described by

$$E_{ex} = \int A \left(\nabla \frac{\mathbf{M}}{M_s}\right)^2 dV = \int A \left[\left(\nabla \frac{M_x}{M_s}\right)^2 + \left(\nabla \frac{M_y}{M_s}\right)^2 + \left(\nabla \frac{M_z}{M_s}\right)^2\right] dV \tag{2.2}$$

where A denotes the exchange stiffness constant, M_s the saturation magnetization and V the sample volume. The exchange stiffness is a measure of the force acting to keep the spins aligned. It is related to the exchange integral J, the magnitude of the individual spins and geometric factors associated with the crystal structure of the magnetic material.[43,44]

The energy of a magnet depends on the orientation of the magnetization with respect to the crystal axes. This tendency to align the magnetization preferably along one particular crystallographic axis is called **magnetocrystalline anisotropy**. Its origin is the coupling of the spin part of the magnetic moment to the shape and orientation of the electronic orbital (spin-orbit coupling) and the interaction of the orbitals with their environment (crystal field). If an atom with an asymmetric electronic charge distribution is placed in an asymmetric local crystal field (crystal of low symmetry), the atomic orbitals have an energetically favorable orientation within the crystal field. In materials with a strong spin-orbit coupling the torque on a spin in an external magnetic field which deviates from the magnetocrystalline easy axis may also act on the orbital moment. A large field can then even cause large anisotropic strains (magnetostriction). In the case of a uniaxial anisotropy (i.e. for cobalt), the magnetocrystalline anisotropy may be represented by a series expansion of the form[47]

$$E_{mc} = \sum_n K_n V sin^{2n}\theta \tag{2.3}$$

where the K_n are the anisotropy constants and θ is the angle between the magnetization vector and the crystallographic easy axis. Odd powers can be omitted since by symmetry the positive and negative θ directions are crystallographically and magnetically equivalent.[45] The most simple expression for a magnet of low symmetry (triclinic or monoclinic) with volume V is

$$E_{mc} = K_1 V sin^2\theta \tag{2.4}$$

with the first uniaxial anisotropy constant K_1. Anisotropy expressions for crystals of higher symmetry usually contain higher order terms. In the case of a cubic anisotropy as in iron, the determination of the magnetocrystalline anisotropy contribution is more complicated. The crystal axes are the directions of easy magnetization, the body diagonals correspond to the magnetic hard axes. The anisotropy energy of iron in an arbitrary direction of the magnetization with respect to the cubic axes is expressed with the corresponding directional cosines $\alpha_1, \alpha_2, \alpha_3$. Due to restrictions imposed by the cubic symmetry, the first terms contributing to the anisotropy energy are the 4^{th} and 6^{th} order terms:[47]

$$E_{mc} = K_1 V(\alpha_1^2\alpha_2^2 + \alpha_2^2\alpha_3^2 + \alpha_3^2\alpha_1^2) + K_2 V(\alpha_1^2\alpha_2^2\alpha_3^2) \tag{2.5}$$

In the case of iron, the second term of Eq. 2.5 is small and often only the first term is considered (K_1=4.6·10^4 J/m^3, K_2=1.5·10^4 J/m^3 at room temperature[47,48]).

It is often convenient to express anisotropies in terms of anisotropy fields. For the example in Eq. 2.4 the expression would be $\mu_0 H_k = 2K_1/M_s$. Materials with a high magnetic anisotropy that can keep the magnetization in a desired direction are often used as permanent magnets. For magnetic recording materials with intermediate anisotropies are preferred.

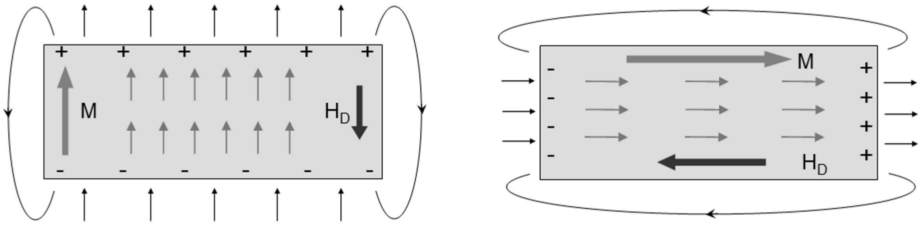

Figure 2.1: Origin of the magnetic shape anisotropy (schematic). The homogeneous sample magnetization **M** in a single domain particle leads to the creation of free magnetic poles at the sample extremities. These lead to an internal demagnetizing field $\mathbf{H}_D$. Depending on the magnetization direction, the amount of magnetic surface charges can be larger (left) or smaller (right) leading to a corresponding magnetostatic energy difference.

At the surface of a ferromagnetic body the magnetization **M** diverges. If the magnetization has a component perpendicular to the surface plane, free magnetic charges are formed (Fig. 2.1). The closing path between these virtual "monopoles" is through the body, a **demagnetizing field $\mathbf{H}_D$** opposite to the magnetization is formed. Fig. 2.1 shows two differently magnetized elongated single domain bodies. If the magnetization is oriented along the short axis (left image), many magnetic poles are created on the large top and bottom surfaces creating a large demagnetizing field. If the body is magnetized along its long axis, only a few magnetic surface charges are formed on the small faces resulting in a smaller demagnetizing field. When this example is extended to an infinite plate magnetized in plane or a rod magnetized along its axis, there is no demagnetizing field at all. This **shape anisotropy** makes it easier to magnetize the object along its long axis than along its short axis. Depending on the shape of the magnet, $\mathbf{H}_D$ can be a very complicated function of position. However, there are a few simple cases. For an ellipsoidal magnet,

$$\mathbf{H}_D = -N\mathbf{M} \tag{2.6}$$

where N is the demagnetization tensor.[44] If the ellipse is uniformly magnetized along one of its axes, N can be diagonalized and only contains the elements N_x, N_y and N_z. For a sphere, $N_x = N_y = N_z = \frac{1}{3}$ yielding $\mathbf{H}_d = -\mathbf{M}/3$. If the magnetization of a very long cylindrical rod parallel to x lies along the rod axis, the magnetic charges at its ends are very far away from each other. Thus the demagnetizing factors are $N_x = 0, N_y = N_z = \frac{1}{2}$. This case can be considered when dealing with ferromagnetic nanowires. The magnetostatic energy E_D associated with a particular magnetization direction can be expressed as

$$E_D = -\frac{1}{2}\mu_0 V\mathbf{M}\cdot\mathbf{H}_D = \frac{1}{2}\mu_0 VNM_s^2 \tag{2.7}$$

with the demagnetization factor N along the direction of magnetization. For long wires, the associated shape anisotropy field can be expressed as $\mu_0 H_k = 2K_s/M_s = \frac{1}{2}\mu_0 M_s$ with the shape anisotropy energy $K_s = E_D/V = \frac{\mu_0}{4}M_s^2$. Shape anisotropy is mostly important in nanoscale objects. In a macroscopic magnet this mechanism is substituted by domain formation.

The last term in Eq. 2.1 is the **Zeeman energy**, the magnetic potential energy of a magnetized object in an external magnetic field **H**:

$$E_Z = -\mu_0 V \mathbf{M} \cdot \mathbf{H} = -\mu_0 V M H cos\theta \tag{2.8}$$

with the angle θ between the magnetization and the external field. E_Z is minimized when the magnetization is aligned with the applied field.

Eq. 2.4, 2.7 and 2.8 are based on a simple model for single-domain magnets with homogeneous magnetization.[49]

2.1.2 Magnetic domains

A magnetic domain is a region of homogeneous magnetization. Within a ferromagnetic body, neighboring domains can be magnetized in different directions. Thus the atomic magnetic moments are aligned on a small scale, but the overall magnetization can still be zero if the domains compensate each other. Domain structures are formed to lower the magnetostatic energy (stray field energy) of a system. If a magnet is saturated in one direction (single domain state, left image in Fig. 2.2), magnetic poles are created at its ends and a large stray field outside the sample is necessary to close the field lines. If the magnetization is split in two domains (center image), the magnetostatic energy decreases by a factor of two as the stray field's spatial extension is reduced. Accordingly, N domains will reduce the energy of the saturated state by 1/N.[47] The most favorable domain configuration in terms of a minimized magnetostatic energy is schematically shown in the right image of Fig. 2.2. So-called closure domains are formed at the end faces of the magnet and prevent the creation of free poles at the surface. Consequently, the flux circuit is completed within the magnet, no stray field develops and the magnetostatic energy associated with this state is zero. However, it must be noted that changing the magnetization direction in a new domain and creating a domain wall which separates the two domains costs energy. The exchange interaction between two neighboring spins is minimized when these are oriented parallel and maximized when they are antiparallel. Thus a minimized exchange energy in the transition region between two domains favors a very small deviation angle between

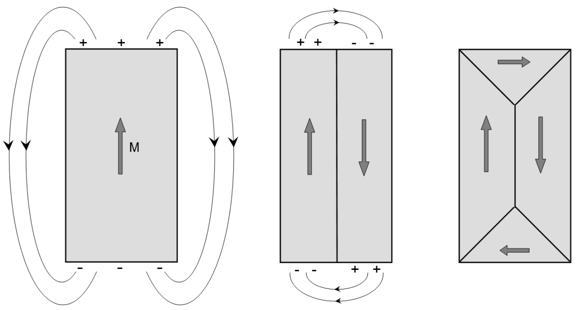

Figure 2.2: Reduction of the magnetostatic energy by the formation of domains. Left: Single domain state associated with a large stray field. Middle: The formation of two domains lowers the magnetostatic energy. Right: Closure domains reduce magnetic surface charges and the correlated stray field.

neighboring spins resulting in very large domain walls. In contrast, in the case of a magnetocrystalline anisotropy this scenario increases the anisotropy energy as the spin orientation along one certain axis is favored and as few spins as possible should deviate from the crystalline easy axis. An intermediate state must be found. In the case of a 180° Bloch wall, the domain wall thickness can be estimated using the anisotropy energy K and the exchange stiffness A:[42]

$$d_{DW} = \pi\sqrt{\frac{A}{K}} \tag{2.9}$$

A is usually in the order of 10^{-11} J/m leading to a domain wall thickness of approximately 50 nm for low anisotropy materials such as iron (K_1=4.6·10^4 J/m^3) and 4 nm for hard magnetic systems as FePt (K_1=7·10^6 J/m^3).[50] The domain wall energy density $e_{DW} = 4\sqrt{AK}$ is then in the order of 3 to 40 mJ/m^2. The corresponding values for iron can also be found in table 2.1. The number of domains has reached its maximum when the creation of a new domain wall costs more energy than the gain in magnetostatic energy. Especially when considering micro- or nanoscale magnets, the domain wall energy is a crucial parameter that can favor a single domain state. An evaluation of the relevant energy contributions reveals that spherical particles with a size smaller than the critical size

$$D_{crit} = \frac{36}{\mu_0}\frac{\sqrt{AK}}{M_s^2} \tag{2.10}$$

prefer the single domain state.[42] In very hard magnetic materials, D_{crit} can exceed 1 µm. The critical size is an equilibrium property. In contrast, hysteresis is a non-equilibrium phenomenon caused by energy barriers. Furthermore, equilibrium domains are qualitatively different from the nonuniform magnetization states occurring during magnetization reversal. Thus the single domain size can deviate from the calculated value if hysteresis phenomena occur. For non-spherical magnets, the critical size increases with a decrease in the demagnetizing factor and increasing aspect ratio (length/diameter). Cobalt and iron nanowires with an aspect ratio of 10 can be ex-

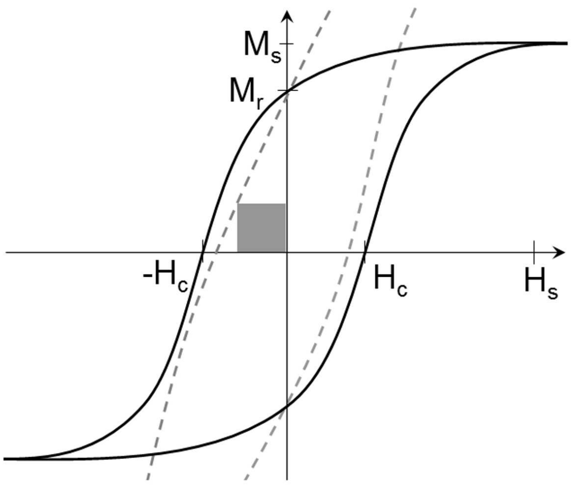

Figure 2.3: Sketch of a typical hysteresis loop, magnetization M versus magnetic field H. The dashed grey line represents the corresponding $B-H$ loop. The gray area represents the magnetic energy product $(B \cdot H)_{max}$. M_s: saturation magnetization, all spins of the sample are aligned along H, M_r: remanent magnetization at zero field after saturation, H_c: coercive field, needed to reduce the magnetization to zero after saturation, H_s: field needed to reach magnetic saturation (saturation field).

pected to be single-domain for diameters less than about 140 nm, nickel with its smaller saturation magnetization forms single-domain nanowires for diameters less than about 600 nm.[43]

A second fundamental length scale is the exchange length given by[42]

$$l_{ex} = \sqrt{\frac{A}{\mu_0 M_s^2}} \tag{2.11}$$

It is the length below which atomic exchange interactions dominate typical demagnetizing fields. This parameter determines the transition from coherent rotation to incoherent nucleation as a magnetization reversal mechanism. In perfect wires, this transition occurs at the so-called coherence diameter $d_{coh} = 7.31\, l_{ex}$ which is for Fe, Co and Ni 11, 15 and 25 nm respectively.

2.1.3 Magnetic hysteresis

Magnetic hysteresis refers to the history dependence of the magnetization on the external magnetic field. The magnetic system needs to overcome field-dependent energy barriers to reach an energy minimum determined by a material's anisotropy.[42] In zero field, thermal fluctuations are usually too weak to overcome these barriers in macroscopic bodies. The hysteresis loop, the function $M(H)$ or $B(H) = \mu_0(H + M)$, is obtained by averaging over the local magnetization $\mathbf{M}(\mathbf{r})$. Many complex factors such as the magnet's microstructure, orientation, shape and defects influence the result. Fig. 2.3 shows a sketch of a typical hysteresis curve of a multi domain body or an assembly of single domain particles with the parameters that can be obtained from it. A hysteresis curve usually displays the magnetization component parallel to the external

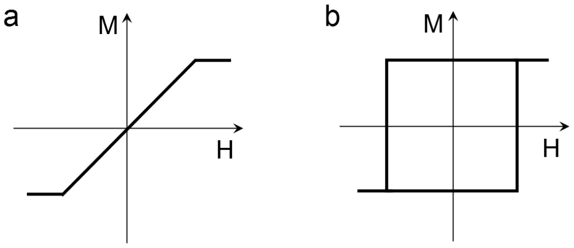

Figure 2.4: Schematic hysteresis loop $M(H)$ for different angles θ between the external field and the easy axis of a body with uniaxial anisotropy: a) θ=90° (hard axis), b) θ=0° (easy axis).

field. When the field is increased from zero to the saturation field H_s, the system is in a magnetically saturated state M_s. When the field is driven back to zero, a remanent magnetization M_r remains. Only at the reversed field H_c the sample magnetization is zero before it changes sign. The hysteresis curve is due to an irreversible behavior while the sample magnetization is reversed. This is due to energy barriers that hinder the reversal, e.g., a hindered domain wall motion. The energy loss created by this effect is given by the area inside the loop. A measure for it is the energy product $(B \cdot H)_{max}$ (gray area in Fig. 2.3). The energy product increases with the coercivity H_c which is often used to classify a magnetic material. Materials with a low coercivity ($H_c < 10^3$A/m) are called soft magnetic and often used as transformers where a small energy loss is required. High coercivity materials are called hard magnetic as the magnetization is more stable against reversal. They are preferably used as permanent magnets, e.g., in electric motors and generators.[45]

When an opposing external magnetic field is applied, the sample magnetization can reverse either by rotating in the field direction or by moving domain walls such that domains magnetized along the field are expanded. If the material possesses any kind of uniaxial anisotropy, the reversal mechanism depends strongly on the alignment of the external field with the magnet's easy axis (magnetization direction favored by the anisotropy). The hysteresis behavior can be estimated by evaluating the magnetic energy of the system in the external field and finding the equilibrium value defined by $\partial E/\partial\theta = 0$ and $\partial^2 E/\partial\theta^2 > 0$.[45] For a simple model, one can consider a particle with domain walls parallel to its easy axis. If the field is applied perpendicular to the easy axis, it exerts a torque on the magnetization which consequently rotates continuously with the field. This results in a slanted hysteresis loop with no coercivity (Fig. 2.4 a). If the field is applied along the magnet's easy axis, there is no torque on the domain magnetization, but on the canted spins in the domain wall. These can rotate to align with the field thus shifting the wall in favor of the aligned domain. As usually the domain walls are pinned in some way and the nucleation of a new domain wall in a single domain particle requires energy, this process can only start after an energy barrier is overcome. When this happens, the magnetization of the particle reverses abruptly at the so called switching field. This results in a rectangular hysteresis loop with a large remanent magnetism and a coercivity depending on the size of the energy barrier (Fig. 2.4 b).

The dependence of a single nanowire's switching field on the angle θ between the external magnetic field and the wire axis is often measured to obtain information on the mechanism of the magnetization reversal within a nanowire.[43] A reversal by coherent rotation or curling can be distinguished by the shape of the resulting curve. Coherent rotation means that all spins rotate simultaneously parallel to each other towards the external field thus minimizing the exchange energy. In curling mode neighboring magnetic moments do not need to be parallel which permits the formation of configurations with no net magnetization along the wire's hard axis minimizing the demagnetization energy. These reversal mechanisms will not be discussed in detail here as the samples studied in this work rather suggest a reversal via the introduction of a domain wall (section 4.2). However, the nucleation of the first small section of reversed magnetization in a nanowire might be explained by a curling mechanism (see Lipert et al.[9])

Hysteresis loops of a polycrystalline sample or an ensemble of particles usually average over a distribution of easy directions. The resulting curve is then rounded and the extracted parameters are only valid for the whole ensemble, not the individual grains or particles.

2.2 PROPERTIES OF IRON

Iron can occur in three different modifications, some of their properties are shown in table 2.1. At room temperature, the body-centered cubic crystal structure of α-iron (ferrite) is present. However, depending on the synthesis method also γ-iron can be found in the confining structure of a carbon nanotube. δ-iron is usually only found at very high temperatures. Table 2.1 also lists some intrinsic magnetic properties of α-iron:[42] the saturation magnetization M_s, the exchange stiffness A and the first and second anisotropy constants K_1 and K_2.

Table 2.1: Properties of iron.[51] mp - melting point, M_s - saturation magnetization (300 K),[43] A - exchange stiffness,[52] $K_{1,2}$ - magnetocrystalline anisotropy constants (300 K)[47,48], d_{DW} - domain wall thickness[46] (Eq. 2.9), l_{ex} - exchange length,(Eq. 2.11) d_{coh} - coherence length.

	α-iron	γ-iron	δ-iron
	ferromagnetic	paramagnetic	paramagnetic
stable until	1179 K	1674 K	1812 K (mp)
crystal structure	bcc	fcc	bcc
lattice constant	2.866 Å	3.647 Å	2.932 Å
density	7.87 g/cm^3	7.65 g/cm^3	
M_s	$1.7{\cdot}10^6$ A/m		
A	$1{\cdot}10^{-11}$ J/m		
K_1	$4.6{\cdot}10^4$ J/m^3		
K_2	$1.5{\cdot}10^4$ J/m^3		
d_{DW}	46,nm		
l_{ex}	1.7 nm		
d_{coh}	11 nm		

2.3 MAGNETIC PROPERTIES OF ENSEMBLES OF FERROMAGNETIC NANOWIRES

Many experimental studies have been conducted on the magnetic properties of ferromagnetic nanowires.[41,43,46,53] Most of them regard the properties of a large ensemble of nanowires, e.g., electrodeposited wires in a porous aluminum oxide membrane or Fe-CNT aligned on a substrate. It has to be noted that it is in many cases not possible to deduce the properties of an individual wire from these measurements. Nevertheless the results reveal interesting tendencies that will be discussed in this section.

The magnetic properties of transition-metal nanowire arrays produced by electrodeposition were reviewed by Sellmyer et al.[46] A typical hysteresis loop obtained of such an array of iron nanowires is shown in Fig. 2.5 a. The parallel and perpendicular sign refer to the direction relative to the film plane, meaning perpendicular and parallel to the nanowire axis. Both coercivity and remanence decrease significantly when measured perpendicular to the wire axis. This uniaxial anisotropy with the easy axis along the wire axis arises from their large shape anisotropy. This example also shows how

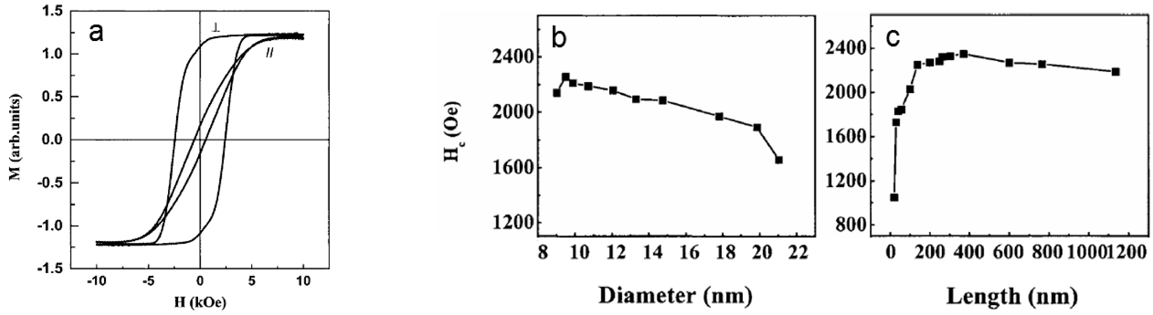

Figure 2.5: Coercivity of ferromagnetic nanowires. a) Hysteresis loop of an array of iron nanowires with the external field applied parallel or perpendicular to the film plane. b) Dependence of the corecivity of Co nanowires on the wire diameter and c) on the wire length. (All images taken from Sellmyer et al.[46])

the rectangular hysteresis loop for the field applied along the wire axis is smeared out due to the averaging effect over a large ensemble of nanowires with different switching fields and slightly different orientations.

Sellmyer et al. also investigated the influence of the length and diameter of cylindrical nanowires on their coercivity. Fig. 2.5 b and c show the coercivity of Co nanowires as a function of their diameter and length. For samples with varying diameter the length was kept constant at ~800 nm. The length dependence was measured with samples with 10 nm wire diameter. It can be seen that the coercivity decreases slightly with increasing wire diameter. In contrast, an increasing nanowire length initially leads to a steep increase of coercivity until a constant value is reached for an aspect ratio >1:20. This dependence of the coercive properties on the wire dimensions can be used to tailor nanowires with specific magnetic properties.

3 Methods

In this chapter, some methods that were used for the fabrication and characterization of samples are briefly introduced. The focus will be on scanning probe microscopy as this technique is of main interest in this work.

3.1 FeCNT growth by chemical vapor deposition

The FeCNT material used in this work is synthesized by thermal CVD using solid powder ferrocene as a precursor. A two zone furnace with separate sublimation and reaction zones is used (see section 1.3).[54] Silicon wafers with a 10 nm aluminum layer and a 2 nm iron layer on top were chosen as supporting substrate for the FeCNT growth in the reaction zone. It was suggested in works of other groups[55,56] that the aluminum buffer layer improves the alignment of the growing iron-filled carbon nanotube arrays and helps to produce a smaller distribution of tube diameters.

For the FeCNT synthesis, the ferrocene is sublimated in the sublimation zone for 10 minutes at 150°C and with a constant argon flow rate of 150 sccm. Meanwhile, the substrate is kept at a temperature of 300°C to prevent the condensation of ferrocene in the reaction zone. After the sublimation reaches a constant level, the temperature of the reaction zone is increased from 300°C to 800°C at a heating rate of 0.6 K/s. This heating rate is chosen based on the fact that such relatively high heating rates support the aligned growth of carbon nanotubes in the initial stage of the growth process.[57] At temperatures above 600°C, ferrocene starts to decompose[58]. The resulting carbon species interact with the iron catalyst layer and form carbon nanotubes and other iron and carbon containing structures on the substrate. Iron atoms and clusters stemming from decomposed ferrocene produce the iron filling of the nanotubes during their growth.[59] The high iron to carbon ratio of the precursor leads to carbon nanotubes with a long, continuous filling.[60] However, this high ratio also leads to a decoration of the already grown FeCNT with carbon coated iron or iron carbide particles (Fig. 3.2 c). This can be a disadvantage for the application of the FeCNT.

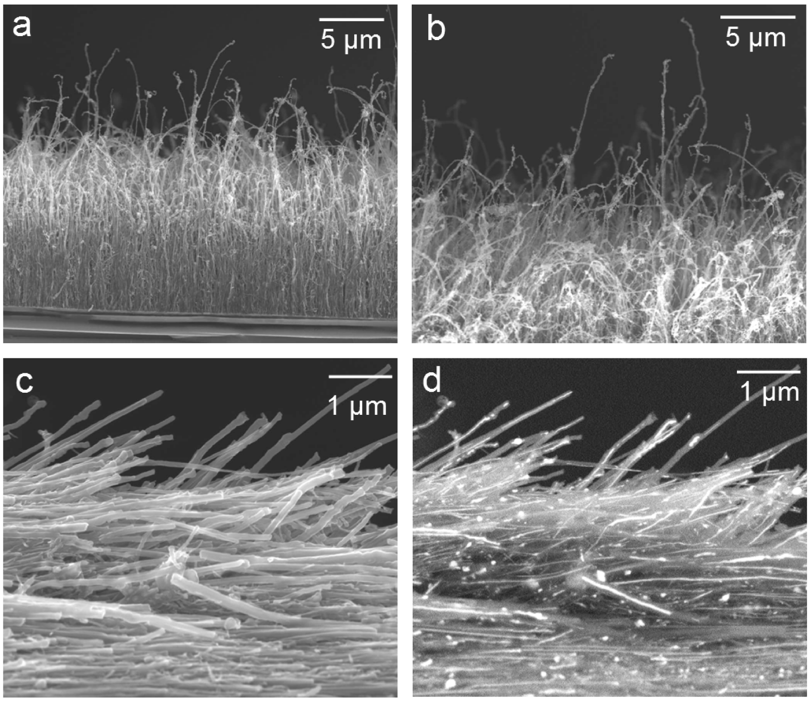

Figure 3.1: SEM micrographs of FeCNT produced by thermal CVD on a catalyst coated silicon substrate. a) As grown FeCNT on the substrate. b) Upper part of the FeCNT forest. Small iron containing particles decorate the exposed FeCNT ends. c) Lower part (close to the substrate) of the FeCNT, the FeCNT have been scraped off the surface for this image. d) BSED image of the region shown in b). The iron filled nanotube parts are of lighter color.

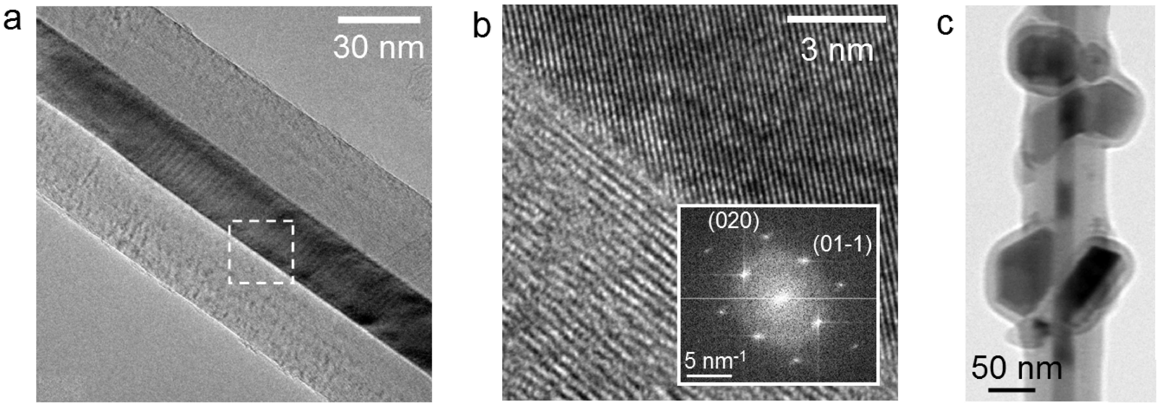

Figure 3.2: TEM micrographs of individual FeCNT. a) Section of a FeCNT with a 25 nm wide filling. b) Zoomed in image of the boxed area in a). The crystalline iron filling and carbon shells are clearly visible. Inset: Selected area electron diffraction pattern of the α-iron filling. c) Section of a FeCNT that is decorated with carbon coated iron particles.

SEM images show that this preparation method yields multiwall carbon nanotubes with lengths between 10 and 25 μm and a continuous iron filling of several microns in at least one section of each tube (Fig. 3.1). The nanotube diameters lie in the range of 50-100 nm. The iron core diameters were estimated in transmission electron microscopy investigations to be 15-50 nm (Fig. 3.2 a). With high resolution selected area electron diffraction measurements, the filling of the produced FeCNT could be identified as α-iron (Fig. 3.2 b).

3.2 ELECTRON MICROSCOPY

3.2.1 Scanning electron microscopy

In scanning electron microscopy (SEM) images are obtained by raster scanning the surface of the sample of interest with a beam of electrons. The incident primary electron beam interacts with the atoms at the conductive sample's surface in different ways. This leads to signals including secondary electrons, back-scattered electrons and characteristic X-rays giving information about the sample's surface topography, composition and other properties such as electrical conductivity. The achievable magnification ranges from 100 times to more than 500000 times depending on the instrument in use.[61,62]

The most common imaging mode collects low-energy (<50 eV) secondary electrons that are ejected from the K-orbitals of the sample atoms by inelastic scattering interactions with the incident electrons. Due to their low energy, these electrons originate within a few nanometers from the sample surface. They are detected by an Everhart-Thornley detector. Back-scattered electrons (BSE) are beam electrons that are reflected from the sample atoms by elastic scattering. The intensity of the BSE signal is strongly related to the atomic number of the specimen, thus BSE images can provide information about the distribution of different elements in the sample. Characteristic X-rays are emitted when the electron beam removes an inner shell electron from an atom of the sample, causing a higher energy electron to fill the shell and release energy in the form of X-rays. These can be used to identify elements in the sample.

In this work, an FEI Nova NanoSEM 200 with acceleration voltages of 5-30 kV is used to image the FeCNT samples. Furthermore, the fabrication of FeCNT sensors is conducted in the SEM as will be explained in section 5.2. For this purpose, the SEM is equipped with a Kleindiek three-axis micromanipulation system (Fig. 3.3).

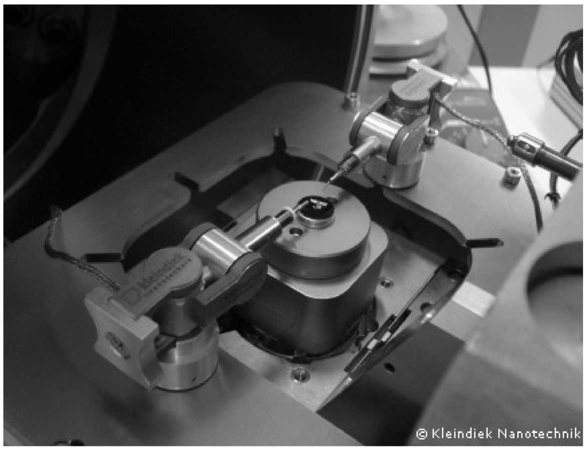

Figure 3.3: Kleindiek micromanipulator setup in a SEM (in this work only one manipulator was used).

3.2.2 Focused ion beam

Focused ion beam (FIB) is a SEM-based technique for the localized analysis, deposition, and ablation of materials with a focused beam of ions (usually gallium). Most often, a FIB is incorporated in a system with both electron and ion beam columns. The electron beam is then used for imaging to avoid excessive damage to the sample. The gallium primary ions hit the sample surface and sputter a small amount of material. The ablation can be controlled via the beam current and exposure time allowing a milling precision in the sub-micron range. Furthermore, a FIB can also be used to deposit material via ion beam induced deposition.

In section 5.2 FIB is used to cut off unwanted parts of FeCNT MFM probes.

3.2.3 Transmission electron microscopy

In transmission electron microscopy (TEM), a beam of high energy electrons (10 keV up to several MeV corresponding to wavelengths in the pm range) is transmitted through a very thin sample. Special electron lenses working with electric and magnetic fields are used to direct the electron beam. The optical path resembles that of an optical microscope, however, the image formation is different. Due to a strong absorption and scattering with the specimen atoms via Coulomb forces, the sample's thickness is limited to approximately 100 nm.[61]

Here, a FEI Tecnai F30 is used for the structural investigation of FeCNT. The instrument also enables high resolution selected area electron diffraction measurements to investigate the sample's crystallographic structure.

3.3 SCANNING PROBE MICROSCOPY

3.3.1 Fundamental principles of scanning probe microscopy

Scanning probe microscopy (SPM) refers to all techniques that scan the surface of the sample of interest with a probe adapted to the particular aims of the investigation. The probe is operated via an electronic control unit with the probe sample interaction as feedback parameter. The resolution of SPM is limited by the shape and size of the probe, special probes can achieve atomic resolution. The scan range in SPM can be as small as a few nanometers in scanning tunneling microscopy (STM) or larger than 100 µm in atomic force microscopy (AFM). The wide variety of possible measurement conditions and modes makes SPM an important tool in all fields of micro- or nanotechnology. Specialized SPM techniques give information on several local properties of surfaces such as the topography, the material's elasticity and hardness, electrostatic potentials, density of states and magnetic stray fields.

Scanning tunneling microscopy was the first SPM technique invented in 1981 by G. Binnig and H. Rohrer.[61,63] It is based on the quantum mechanic tunneling of electrons between a metal tip and a conducting sample over a distance of ∼1 nm. The position of the probe relative to the surface is controlled by piezo actuators, a technique which is employed in all other SPM methods as well. After the success of STM that enabled atomic resolution of conducting surfaces in 1982, many more SPM techniques were developed in the following years. The most diverse method is probably atomic force microscopy invented in 1986[64] due to the possibility to image different interaction forces. These forces include:

- **Short range forces**
  At tip-sample distances comparable to the extension of electronic wave functions (below 2 Å), these wave functions can overlap leading to repulsive forces due to the Pauli exclusion principle. If the distance between tip and sample is very small and there is no more electronic screening of the ionic atom cores, an additional repulsive force can occur. In the Lennard-Jones-Potential, these forces are described by the $(\text{distance})^{-12}$ term. First AFM instruments used the so called contact mode (static mode) which is based on the repulsive short range force between probe and sample.

- **Van der Waals forces**
  Van der Waals forces are dipolar forces based on statistical fluctuations in the electron distribution of the involved atoms (dispersion forces). They are much

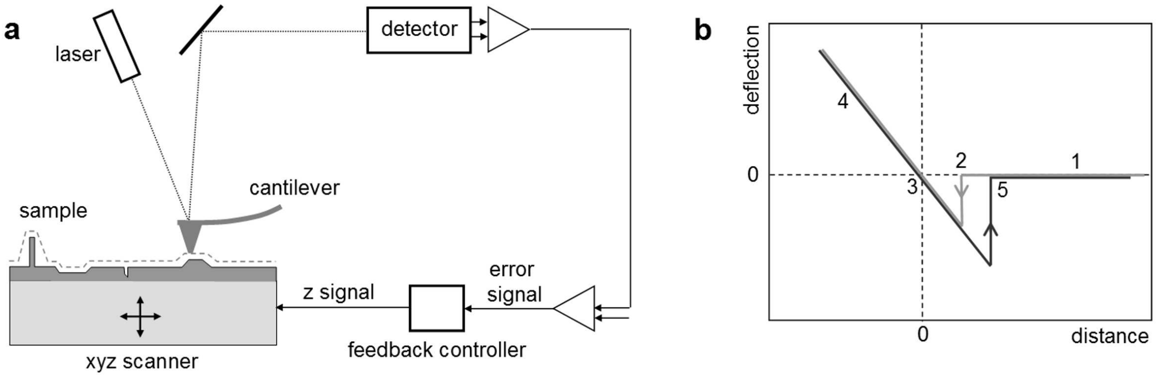

Figure 3.4: a) Schematic showing the principle of a scanning probe microscope, e.g., an AFM.[45,61] The resolution of SPM is limited by the shape of the probe. b) Schematic graph of a cantilever deflection vs. distance curve in AFM.

weaker than the short range forces (in the order of 10^{-13} N) but act over several nanometers depending on size and shape of the tip. The corresponding potential is proportional to $(\text{distance})^{-6}$. Van der Waals forces are detected in non-contact mode (dynamic mode) AFM.

- **Electrostatic forces**
  Electrostatic forces are caused by localized charges on the sample surface or SPM probe or by a work function difference. Their magnitude and distance dependence $(\text{distance})^{-2}$ are given by the Coulomb law. The long range electrostatic force can be used to estimate the surface topography at distances of hundreds of nm by applying a bias between tip and sample. A bias can also be used to cancel electrostatic interactions.

- **Magnetic forces**
  Magnetic forces are detected by a ferromagnetic SPM probe. The force acts between the probe's magnetic moment and the magnetic stray field close to the sample's surface. The magnetic forces are longer range than van der Waals and short range forces, however, their range depends strongly on the decay length of the stray field. Magnetic force microscopy (MFM) measurements are usually performed further away from the surface (10-100 nm) to eliminate topographic influences. Magnetic forces can be repulsive and attractive depending on the distribution of charges and dipoles in probe and sample.

The technique of MFM will be explained in detail in the following sections. Additional forces, e.g., capillary forces in humid environment, can occur depending on the measurement conditions.

In scanning force microscopy, the force-sensing probe usually consists of a miniaturized cantilever beam clamped at one side and a probe tip mounted at the other end.[65] Originally, electrochemically etched metal wires were used as cantilevers. An increasing demand for cantilevers with integrated sharp tips led to the development of microfabrication techniques based on silicon or silicon compounds. Nowadays a variety of cantilevers with different geometries, mainly beam- and V-shaped with pyramidal tips, are commercially available. According to Hooke's law it is advantageous to have a low spring constant for high force detection sensitivity. However, a low spring constant increases the noise due to a thermal excitation of the cantilever. Additionally, if the magnitude of the detected attractive force gradient gets close to the cantilever's spring constant, the cantilever position becomes unstable. It can then stick to the sample surface without the necessary restoring force (jump to contact). At last, a low spring constant also leads to a low resonance frequency which reduces the vibrational sensitivity and SPM maximum scan rate. Thus a certain minimum spring constant is needed. Commercial cantilevers have a spring constant in the order of $10^{-2}...10^{2}$ N/m, and a resonance frequency in the range of 10 to 500 kHz.[66]

Fig. 3.4 a shows the simplified working principle of an AFM. A sharp tip at the end of a microfabricated cantilever beam is scanned line by line over the sample surface. AFM cantilevers are usually made from silicon or silicon nitride with an etched pyramidal tip at the end. The interaction force leads to a bending of the cantilever. The cantilever position is detected through a laser reflection off the cantilever's back side onto a four quadrant photodetector. This signal is then fed back into the scan unit to control the sample stage or perpendicular probe movement. The resulting image is a convolution of the sample topology and the shape of the tip. The forces acting between probe and sample at different distances can be seen in a deflection vs. distance curve (Fig. 3.4 b). To obtain such a curve, the deflection of the cantilever is plotted against its distance from the sample surface. In Fig. 3.4 b, the different stages of the curve are numbered. At large distances, there is no interaction (1) and thus no deflection of the cantilever. When the force constant of the attractive force between sample and probe overcomes the cantilever's spring constant, the probe snaps towards the sample surface (2). Upon further approach, the cantilever regains its unbent shape (3) before pressing onto the surface (4). When the probe is retracted, it sticks longer to the sample surface due to adhesive forces before snapping out of contact (5). Such curves can be used to determine the sensitivity of the detector (volts per nm bending) and to determine the exact position of the sample surface (corresponding to point 3) which will be useful in the calibration experiments described later on.

As mentioned before, AFM measurements can be performed in the static or dynamic mode. In the static mode (contact mode), the cantilever is scanned over the sample surface similar to the needle of a record player. In the repulsive regime (stage 4 in

Fig. 3.4 b), the deflection of the cantilever according to Hooke's law is detected and used as the feedback signal. With an appropriate probe, atomic resolution can be achieved.

All AFM and MFM measurement presented in this work are based on the dynamic mode. The cantilever is excited to oscillate close to its resonance frequency of generally several kHz by a piezo drive. Interactions between probe and sample lead to changes in the probe's oscillatory behavior which are displayed as the signal. The following section will discuss this method in more detail.

3.3.2 Dynamic mode scanning probe microscopy

In the limit of small oscillation amplitudes, the cantilever can be described as a damped driven harmonic oscillator. The corresponding equation of motion for an oscillation along z is[45,65]

$$m\ddot{z} + m\frac{\omega_0}{Q}\dot{z} + k_0 z = F(z) + F_{ex}cos(\omega t) \tag{3.1}$$

with the excitation force F_{ex}, the angular frequency of the driving force $\omega = 2\pi f$ and the interaction force $F(z)$. The free $(F = 0)$ cantilever's properties are described by its spring constant k_0, its angular resonance frequency $\omega_0 = \sqrt{\frac{k_0}{m}}$ and the quality factor Q of its vibration. Q is related to the damping factor γ through $Q = m\omega_0/2\gamma$. The damping factor reflects the dissipative influence of the cantilever environment and other sources of dissipation on its vibrational behavior. Q can take values well below 100 in liquids and more than 100,000 in ultra high vacuum due to the much narrower resonance peak. It can also be expressed as $Q = \frac{f_0}{\delta f}$ with δf being the width of the resonance peak at its maximum amplitude devided by $\sqrt{2}$, e.g. obtained from the resonance curve (Fig. 3.5, left). The original spring constant k and resonance frequency ω_0 of a cantilever with a rectangular cross section can be calculated from the cantilever geometry (length L, width W and thickness T), the elastic modulus E and the density ρ. Wolter et al.[67] give the following expressions:

$$\begin{aligned} k_0 &= \frac{E\,W\,T^3}{4\,L^3} \\ f_0 &= 0.162\,\frac{T}{L^2}\sqrt{\frac{E}{\rho}} \\ \Rightarrow k_0 &= \rho\,LWTf_0^2/0.105 \end{aligned} \tag{3.2}$$

The gradient of the force $F(z)$ between probe and sample induces a change of the cantilever's effective spring constant such that

$$k_{eff} = k_0 - \frac{\partial F}{\partial z}. \tag{3.3}$$

An attractive probe-sample interaction with $\frac{\partial F}{\partial z} > 0$ will effectively soften the cantilever, a repulsive interaction with $\frac{\partial F}{\partial z} < 0$ will make it stiffer. The changed spring constant will modify the cantilever's resonance frequency to

$$\omega_{eff} = \sqrt{\frac{k_0 - \frac{\partial F}{\partial z}}{m}} = \omega_0\sqrt{1 - \frac{1}{k_0}\frac{\partial F}{\partial z}}. \tag{3.4}$$

If the force gradient is much smaller than the cantilevers spring constant ($\frac{\partial F}{\partial z} \ll k_0$), the above equation can be simplified to

$$\omega_{eff} = \omega_0\left(1 - \frac{1}{2k_0}\frac{\partial F}{\partial z}\right) \tag{3.5}$$

leading to a measured frequency shift $\Delta f = f_{eff} - f_0$ of

$$\Delta f = -\frac{f_0}{2k_0}\frac{\partial F}{\partial z}. \tag{3.6}$$

This frequency shift dependence on the interaction force gradient leads to a shift of the cantilever's resonance curve (Fig. 3.5 left) and a decreased oscillation amplitude at the original resonance frequency. The resonance curve of a cantilever can be acquired by oscillating the cantilever with a fixed driving force while sweeping the frequency. Eq. 3.3 to 3.6 are based on the assumption that the force gradient is constant over all tip positions during the oscillation.[45] This is valid when using small oscillation amplitudes.

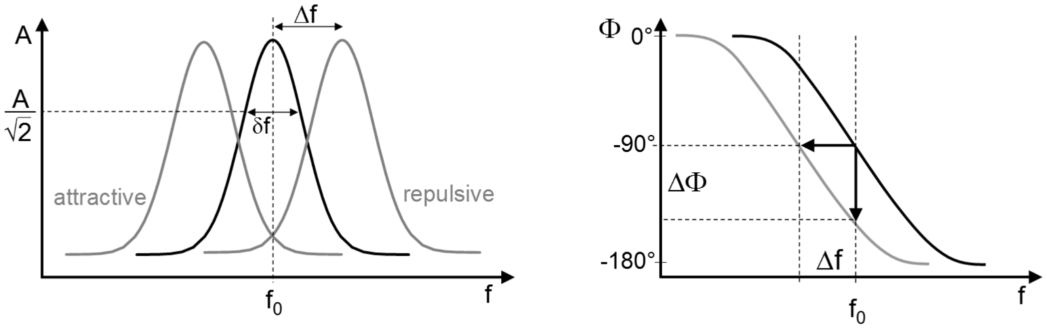

Figure 3.5: Left: Schematic resonance curve of a harmonic oscillator with its width δf (black line). Attractive/repulsive forces (gray lines) lead lo a shift of the whole curve. Right: Phase shift and frequency shift of the cantilever oscillation due to an attractive interaction. The smaller effective cantilever spring constant shifts the curve to a smaller resonance frequency. Both phase or frequency shift can be chosen as the SPM output signal.

The probe-sample force gradient also induces a phase shift $\Delta\Phi$ of the cantilever oscillation:

$$\Delta\Phi = -\frac{Q}{k_0}\frac{\partial F}{\partial z}. \tag{3.7}$$

This is schematically shown in the right graph of Fig. 3.5. Due to the negative sign in Eq. 3.7, an attractive force leads to a negative phase shift. Frequency shift, phase shift or the amplitude signal can be used to monitor the interactions between probe and sample. The choice depends for example on the measurement conditions and the desired information.

3.3.3 Introduction to magnetic force microscopy

Since its development in 1987[10,68], magnetic force microscopy (MFM) has become a powerful tool to obtain spatially resolved information on the magnetic stray fields associated with a sample's surface magnetization or current distribution. For MFM, the probe is usually coated with a ferromagnetic material to enable the magnetic interaction. The probe's magnetic moment then interacts with the magnetic strayfield of the sample leading to a change in the cantilever frequency or phase as described in the previous chapter. MFM is mainly employed for the investigation of magnetic recording media or write heads. Further applications include research on magnetic nanoparticles or superconductors. In MFM, the sample preparation requirements are very low compared to other magnetic imaging techniques. Measurements in different environments are possible (low temperature, vacuum, in liquids).

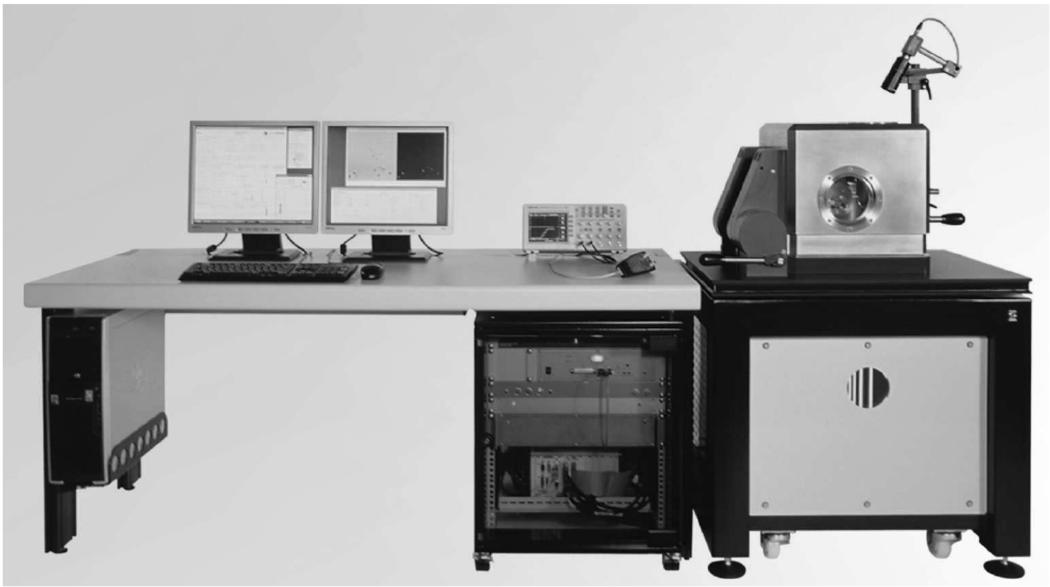

Figure 3.6: The Nanoscan hr-MFM.

In contrast to AFM, the tip-sample distance has to be large enough not to detect the topography but small enough to still detect the smaller (2-3 orders of magnitude) but longer range magnetic forces. The probe-sample distance is not as easy to control as in AFM because the interaction forces (and derivatives thereof) can change sign several times within one image. Thus a constant force feedback cannot be used. One way to solve this problem is to scan the sample in the so-called Lift Mode^{TM} where in a first scan, the topography is measured very close to the surface. This topography is then used to move the tip over the sample at a constant distance to the surface to measure the magnetic signal. Depending on the sample, this lift height is in the order of 10-100 nm. A second measurement option is to not control the tip-sample distance and scan the sample in a constant height, a flat plane above the surface. In this constant height mode, topographic, magnetic and electrostatic signals may be measured at the same time. It can thus be necessary to subtract these influences, e.g., by changing the magnetization direction of the probe in a second measurement. In a hardmagnetic sample, all contrast that stays unchanged is not of magnetic origin.

In this work, both methods have been used. The Veeco DI 3100 AFM uses the Lift Mode^{TM}. This instrument was mainly used for test measurements as it works in ambient condition and sample and probe change are easy. High resolution MFM measurements and calibration measurements were performed in a high vacuum (below 10^{-5} mbar) Nanoscan hr-MFM in constant height mode (Fig. 3.6). The instrument operates at room temperature and is mounted on an active vibration isolation table. All standard cantilevers can be used. Two controllers are used for the cantilever oscillation. The amplitude controller maintains a constant oscillation amplitude. The

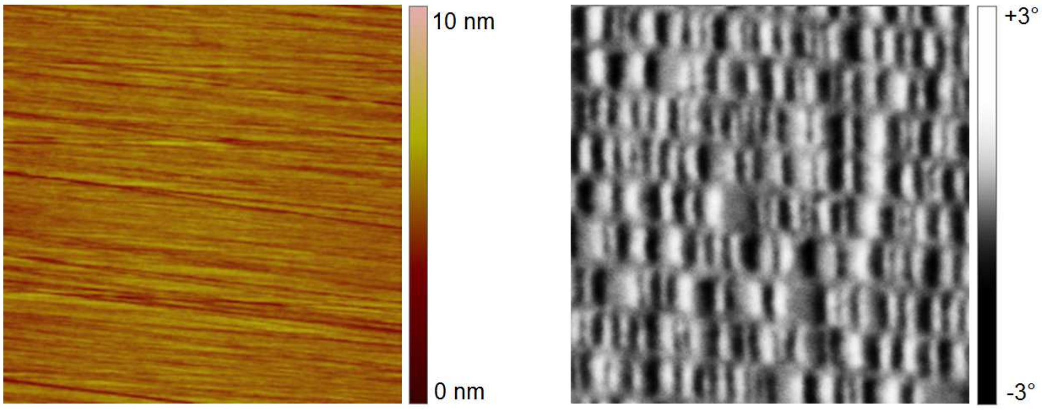

Figure 3.7: Topography (left) and magnetic contrast (phase shift, right) of a magnetic hard disk measured with Lift Mode^{TM} MFM. Scan range: 5 µm × 5 µm.

phase-locked loop controller monitors the phase of the oscillation and keeps the phase shift close to zero to keep the excitation frequency at the cantilever resonance. The maximum x, y, z scan range is 40 µm × 40 µm × 6 µm. For measurements in magnetic fields, it is equipped with several movable permanent magnets to achieve a perpendicular and an in-plane field option (see section 5.5).

As an example, Fig. 3.7 shows the topography (left, relative z piezo position) and magnetic contrast (right, phase shift of the cantilever vibration) of a magnetic hard disk measured with Lift Mode^{TM} MFM. The topography features scratch marks from the reading process. The MFM image shows dark and bright areas corresponding to negative and positive phase shift or attractive and repulsive magnetic forces between probe and sample. Fig. 3.8 explains the image formation process for the case of a longitudinal recording hard disk and the resulting stray field. Neighbouring data bits have opposing magnetization leading to a stray field component along z at the bit ends. The force gradient is detected in the direction of the cantilever oscillation along z. The tip is magnetized along z and detects parallel or antiparallel stray field components depending on its position. The resulting attractive or repulsive magnetic forces are reflected in the negative or positive MFM phase shift signal sketched on the bottom of Fig. 3.8.

3.3.3.1 Quantitative magnetic force microscopy

For quantitative MFM measurements, the interaction between the magnetic stray field of the sample and the MFM probe needs to be described. The term stray field describes the magnetic field outside the sample and is the only part of the total sample field to give rise to a magnetic contrast. Thus this is the only field of importance in the following considerations. The tip-sample interaction can be quantified by considering

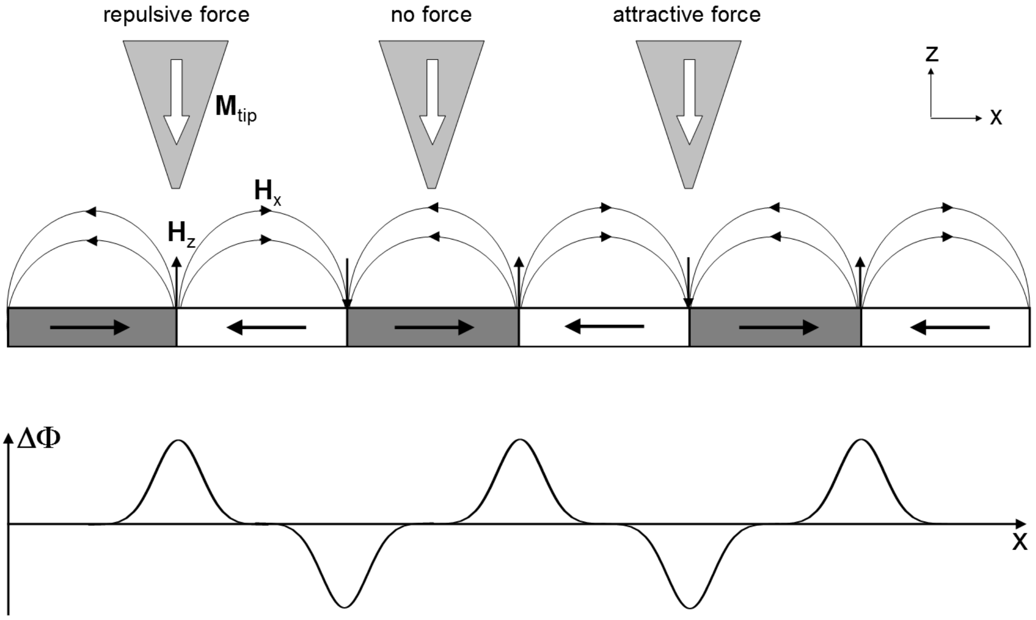

Figure 3.8: Top: Schematic showing the interaction between a magnetic probe and longitudinal recording media. A probe magnetization M_{tip} parallel to the sample stray field H_z leads to attractive forces, antiparallel magnetization leads to repulsion. In the case of a sample magnetic field perpendicular to the probe magnetization, there is no interaction. Bottom: Resulting phase shift signal.

the force $\mathbf{F}(\mathbf{r})$ on the probe which is located in the magnetostatic potential $\phi_s(\mathbf{r})$ of the sample:[65,69]

$$\phi_s(\mathbf{r}) = \frac{1}{4\pi}\left[\iint \frac{\mathbf{M}_s(\mathbf{r}')}{|\mathbf{r}-\mathbf{r}'|} d^2\mathbf{s}' - \iiint \frac{\nabla \cdot \mathbf{M}_s(\mathbf{r}')}{|\mathbf{r}-\mathbf{r}'|} d^3\mathbf{r}'\right] \tag{3.8}$$

$\mathbf{M}_s(\mathbf{r}')$ is the vector field of the sample magnetization, $\mathbf{s}$ is a normal vector on the sample surface. The first integral covers the magnetic surface potential of the sample, all surface charges created by magnetization components perpendicular to the sample surface. The volume integral contains the volume magnetic charges resulting from interior divergences of the sample magnetization vector field. The resulting stray field of the sample is then given by

$$\mathbf{H}_s(\mathbf{r}) = -\nabla \phi_s(\mathbf{r}) \tag{3.9}$$

In the following it is assumed that probe-sample interactions induce a frequency shift and not an energy transfer. This implies that the tip magnetization and the sample stray field do not influence each other. The magnetostatic free energy of a MFM probe in this stray field is

$$\Psi(\mathbf{r}) = \mu_0 \left[\iint \mathbf{M}_p(\mathbf{r}')\phi_s(\mathbf{r}')d^2\mathbf{s}' + \iiint \nabla \cdot [\phi_s(\mathbf{r}')\mathbf{M}_p(\mathbf{r}')] \, d^3\mathbf{r}' \right] \tag{3.10}$$

where $\mathbf{M}_p(\mathbf{r}')$ is the magnetization vector field of the MFM probe. In Eq. 3.10, $\mathbf{s}$ is a vector normal to the MFM probe surface. Here the two-dimensional integral taken over the probe surface describes the interaction of the probe's surface charges with the sample stray field, the three-dimensional integral describes the influence of divergences in the probe magnetization. The resulting magnetic force acting on the probe is then

$$\begin{aligned} \mathbf{F}(\mathbf{r}) &= -\nabla\Psi(\mathbf{r}) \\ &= -\nabla\mu_0 \left[\iint \mathbf{M}_p(\mathbf{r}')\phi_s(\mathbf{r}')d^2\mathbf{s}' + \iiint \nabla \cdot [\phi_s(\mathbf{r}')\mathbf{M}_p(\mathbf{r}')] \, d^3\mathbf{r}' \right] \end{aligned} \tag{3.11}$$

Inserted in Eq. 3.7 or Eq. 3.6 this expression describes the connection between the experimentally measured phase shift or frequency shift and the magnetostatic potential of the sample. For a quantitative evaluation of the experimental data, the magnetization vector field $\mathbf{M}_p(\mathbf{r}')$ of the MFM probe needs to be known in order to solve the integrals in Eq. 3.10. It is generally not possible to obtain the magnetization of a coated tip via micromagnetic calculations because the exact geometry of the ferromagnetic coating and its microcrystalline structure are not known. As a consequence, it is in general not possible to perform MFM in a quantitative way, e.g., to detect a stray field in absolute units.[65] Several approaches have been developed to cope with this problem.

In the case of simple tip and sample magnetization structures, the MFM response can be calculated analytically in direct space. Hartmann[70,71] proposed a simple model for the description of the magnetization of a MFM probe, the point probe model. This model attributes all effective magnetic probe moments to a point dipole or monopole within the probe volume, it will be discussed in more detail in section 3.3.3.2. Rugar et al.[12] used an analytical model to describe MFM data of longitudinal recording media. They also approximated the MFM probe by a point dipole. Wadas and Güntherodt[72] modeled the tip as a truncated pyramid and calculated the MFM signal depending on the tip geometry and tip-sample distance. Engel-Herbert et al.[73] simulated the MFM response for a realistic tip shape incorporating a distribution of magnetic dipoles. These analytic approaches usually require long computing times and are not able to describe complex magnetic probe or sample structures. On the other hand, when very small structures are to be analyzed, the precision of the analytical method is higher than for numerical methods.[73]

One challenge in the analytical reconstruction of MFM images is the three-dimensional spatial integration necessary to get the stray field from the magnetization and the force from the field. Hug et al.[74,75] simplified the procedure by a Fourier transformation of those fields and made use of the fact that their Fourier transforms are simply related by multiplicative functions called transfer functions. The Fourier components of the force acting on the tip can be calculated directly from those of the magnetic surface charges or vice-versa via the so-called tip transfer function. Alternatively, the Fourier components of the sample stray field are calculated by the field transfer function from those of the magnetic surface charge. Then a force transfer function is used to calculate the force from the stray field. The real space values are then obtained by Fourier transformation. In this approach, the MFM probe is calibrated by first measuring MFM images of a standard sample with a well defined magnetization. Using a discrimination level for the frequency shift, the normalized magnetization pattern is obtained from the measurement. This pattern is then used to calculate a force image using transfer functions which contain the probe parameters such as the tip to sample distance or the probe's point charge. The deviation of the calculated force image from the measured image is then minimized through a fit procedure in which the probe parameters are adjusted. Once the tip is calibrated, the size of the z component of the stray field of a perpendicularly magnetized sample with an arbitrarily complex domain pattern can be measured quantitatively.

Alternatively, probe and sample can be treated numerically by dividing both into small subcells.[76] Engel-Herbert et al.[73] used a discretization scheme to break up the tip-sample problem into cells and then calculate the energy of the magnetic tip-sample interaction. This numerical method allowed to simulate the MFM response of the domain structure of sub-micron sized ferromagnetic stripes exhibiting in-plane and out-of-plane magnetized areas. It offers shorter computing times and greater flexibility, opening the door for three-dimensional MFM response simulations.

3.3.3.2 The point probe approximation

Since detailed information about the internal microstructure of the MFM tip for a quantitative MFM data analysis are generally not experimentally available, U. Hartmann proposed the point probe model in 1989.[71] In this model, the magnetic volume of the probe which contributes to the MFM contrast formation, the effective magnetic moment, is described by an imaginary point probe within the real probe. In the case of pyramid shaped coated probes, the point probe is positioned along the pyramid axis at a distance d from the tip apex and can be described by an effective dipole moment

Figure 3.9: Schematic sketch of the point probe model. The effective tip magnetization is attributed to a point probe with a dipole moment m or monopole moment q at a distance d from the tip apex. z denotes the probe-sample distance.

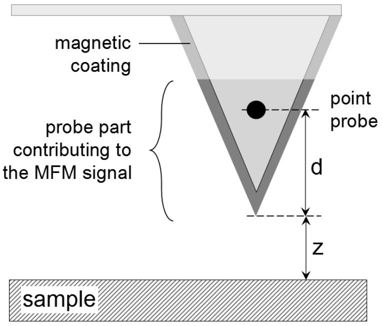

$\mathbf{m}$ or monopole moment q (Fig. 3.9). The monopole moment is defined as dipole moment per length unit. In the case of a cylindrical rod magnetized along its length with a homogeneous magnetization M_r, radius r and length l, the dipole moment can be expressed as $\mathbf{m} = M_r \cdot \mathbf{l}\pi r^2$, the monopole moment of one of the rod ends would be $q = M_r \cdot \pi r^2$.

Applying the point probe model, Eq. 3.11 can be simplified in the following way:[18,65]

$$\mathbf{F}(\mathbf{r}) = \mu_0(-q + m \cdot \nabla)\mathbf{H} \tag{3.12}$$

$\mathbf{H}$ is the sample stray field. Usually the MFM probe only detects the force gradient component parallel to the cantilever deflection, thus only the force component $F_n = \mathbf{n} \cdot \mathbf{F}$ is measured, where $\mathbf{n}$ is the normal unit vector of the cantilever surface. It is assumed here that the probe oscillates along the z axis. So the detected force can be expressed as

$$F_z(r) = \mu_0 \left[-q\, H_z + m_x \frac{\partial H_x}{\partial z} + m_y \frac{\partial H_y}{\partial z} + m_z \frac{\partial H_z}{\partial z} \right] \tag{3.13}$$

Eq. 3.13 contains a monopole component instead of the earlier magnetic surface and volume charges. In addition, the alternative dipole description has been introduced. The initial probe magnetization is set along z which is then the only remaining component of the probe's dipole moment ($m_x = m_y = 0$). Together with Eq. 3.7 this yields the following simple expression for the measured cantilever phase shift:

$$\Delta\Phi = -\mu_0 \frac{180}{\pi} \frac{Q}{k} \left[-q \frac{\partial H_z}{\partial z} + m_z \frac{\partial^2 H_z}{\partial z^2} \right] \tag{3.14}$$

The factor $180/\pi$ accounts for the phase shift being measured in degrees, not radians. Eq. 3.14 now provides the means to determine the probe monopole and dipole moment from the measured phase shift signal if the first and second derivative of the sample stray field are known. When applying this technique, Lohau et al.[17] found that the probe may only be described *either* by a point monopole *or* by a point dipole. This result may reflect the fact that the probe's magnetic moments must not be counted twice as monopole *and* dipole moments. Also, as mentioned before, a shift d of the respective point probe along the z axis needs to be taken into account. Lohau et al. found that both the point monopole description and the point dipole description can be employed equivalently in the case of a coated pyramidal probe and lead to a good fit of the experimental data. The final expressions for the point monopole model and the point dipole model are

$$\Delta\Phi_{monopole} = \mu_0\, q\, \frac{180}{\pi}\frac{Q}{k}\frac{\partial H_z}{\partial z} \tag{3.15}$$

$$\Delta\Phi_{dipole} = -\mu_0\, m_z\, \frac{180}{\pi}\frac{Q}{k}\frac{\partial^2 H_z}{\partial z^2} \tag{3.16}$$

With the help of these relations, a MFM probe can be calibrated for a quantitative analysis of the measured phase shift by determining its effective monopole or dipole moment. Once q or m are known, the gradient of the sample stray field can be obtained quantitatively from the MFM measurements. Different structures that provide a defined magnetic field such as current lines,[18,77] current rings,[17] or magnetic hard discs[12] have been applied to achieve this.

A drawback of the point probe approximation is that the above findings can only be used for quantitative MFM imaging as long as the determined effective probe moment and its position stay constant. However, these parameters can change easily in the case of a coated MFM probe when it is placed in a different sample stray field geometry. This consideration will be further explained in section 5.1. An example for a tip calibration procedure will be explained in the experimental part of this work (chapter 6).

3.3.3.3 Approaches for alternative kinds of MFM probes

A conventional MFM probe usually consists of a silicon cantilever with a sharp micron-scale pyramidal tip at its end which is coated with ferromagnetic material. The tip radius is usually in the range of 5-50 nm. The probe is then magnetized along the pyramid axis resulting in a magnetization parallel to the coating layers on the pyramid sides (Fig. 3.10 a). The maximum achievable resolution of commercially available coated probes ranges from 25 nm to 50 nm depending on the tip geometry and the

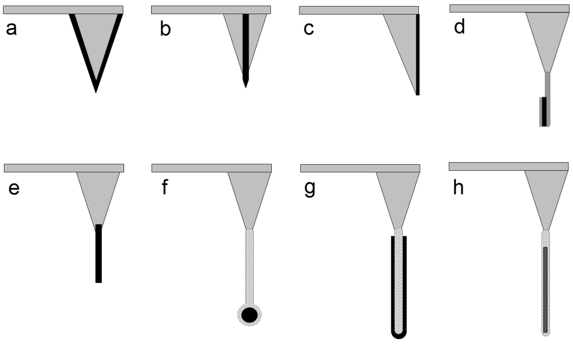

Figure 3.10: Schematic showing various MFM probe designs. a) conventional coated probe, b) FIB modified probe,[79] c) face-coated CantiClever,[80] d) electron beam deposited tip,[81,82], e) nickel nanowire based MFM probe,[83] f) CNT capped with a magnetic particle,[20] g) CNT coated with magnetic material,[19,84] h) FeCNT MFM probe.

properties of the coating.[78] This probe type is easy to fabricate in a batch process and yields good MFM images, but it also has several disadvantages. The metallic coating is subjected to oxidation, which makes it necessary to store the probes in a vacuum or apply a protective layer. Furthermore, the magnetic coating can easily be damaged when scanning the sample surface. Additional magnetic moments along the sides of the pyramid reduce the achievable magnetic resolution. Moreover, the active magnetic volume of the tip coating is not clearly defined which limits the possibilities for a quantitative MFM data evaluation. In the last decade, much experimental effort has been put into the development of improved MFM probes. The main driving force is to obtain a better magnetic resolution in order to gain insight on the properties of nanoscale magnetic features. Other aspects such as durability or the suitability of a probe for quantitative MFM are also considered. Some of these approaches will be presented in this section, an overview can be seen in Fig. 3.10 b-h.

Phillips et al.[79] used tapping mode cantilevers with a 30 nm thick cobalt film evaporated onto one face of the pyramidal tip. The majority of the Co film was then removed by FIB milling leaving a thin bar with a high aspect ratio (Fig. 3.10 b). MFM images with a resolution of 30 nm could be obtained with these FIB modified probes. A different MFM probe fabrication technique has been developed by Saito et al.[80] Their CantiClever MFM tips are prepared by depositing a thin magnetic layer on the narrow side of a silicon nitride tip plane. This results in an elongated magnetic bar with a flat tip end whose magnetization is parallel to the bar (Fig. 3.10 c). The CantiClever yields resolutions better than 30 nm.

Fischer et al.[81] grew a carbon needle on the tip of a conventional AFM cantilever via electron beam deposition. The needle was then selectively coated with ferromagnetic material by tilting the cantilever during deposition. Koblischka et al.[82] used a similar technique, but they coated one whole side of the needle and the pyramidal tip with ferromagnetic material. A carbon mask then covered part of this coating on the needle end. The remaining uncovered coating is etched off again by ion etching (Fig. 3.10 d). The obtainable resolution was in this case also in the range of 30 nm.

An alternative approach for MFM probe fabrication is the use of nanowires. Yang et al.[83] used nickel and cobalt nanowires produced by electrodeposition in an anodized alumina template. These were directly assembled onto the tip of a commercial AFM cantilever by dielectrophoresis (Fig. 3.10 e).

Many groups have put effort into using carbon nanotubes as tips for atomic force microscopy.[85–89] Due to the extraordinary mechanical properties of CNTs these probes have a very long lifetime. Also, their large aspect allows for a much more accurate imaging of topographic features such as deep trenches or nanoscale particles. CNT AFM probes are already commercially available now.[90] Some groups also tried using carbon nanotubes as probes for MFM. Arie et al.[20] used carbon nanotubes that are terminated by a ∼35 nm particle of Ni_3C prepared by catalytic decomposition of benzene (see sketch in Fig. 3.10 f). This probe yielded good MFM contrast and benefits from the mechanical stability of the CNT. However, due to lacking anisotropy the magnetization direction of the spherical particle at the tip is most probably not very stable. Deng et al.[19] and Kuramochi et al.[84] used probes equipped with carbon nanotubes and coated them with magnetic material (Fig. 3.10 g). These sensors show a magnetic resolution of about 10 nm which is among the best possible so far.

Many of the described designs are very promising due to their high resolution potential and the large magnetic shape anisotropy of the coating which leads to a stable probe magnetization. Also, the magnetic volume is more clearly defined then in the case of a coated MFM probe and a point monopole model could be well suited for quantitative data analysis. However, in most cases the magnetic coating is still subjected to oxidation and abrasion. This problem can be solved with the MFM probes based on FeCNT presented in this work (Fig. 3.10 h). They feature a defined magnetic volume of large shape anisotropy which is mechanically and chemically protected by the surrounding carbon shell. The properties of these probes will be discussed in detail in chapter 5.

4 Magnetic properties of individual FeCNT

As described in section 3.1, FeCNT are grown as a dense aligned forest perpendicular to the surface of a silicon substrate. However, the alignment of the nanotubes with respect to the substrate and to each other is not ideal. Within one sample, the length, diameter and perfection of the iron nanowires enclosed in the nanotube can vary to a large extent. In addition, spherical iron particles decorate some of the nanotubes. Consequently, the measurement of the magnetic properties of a whole sample does not necessarily reflect the properties of an individual nanowire, it rather presents an average over all occurring species. Fig. 4.1 shows the hysteresis loop of as-grown FeCNT on a substrate measured parallel and perpendicular to the substrate surface. A difference in coercivity and remanence is clearly visible. The magnetic easy direction is found parallel to the average nanotube axis, the hard direction perpendicular to it as expected from the wire's shape anisotropy. However, the curve is a result of the averaging effect over a large ensemble of nanowires with different switching fields and orientations. This clearly confirms the need to investigate individual FeCNT with localized measuring techniques to obtain information on their magnetic properties. In this chapter, such measurements performed by MFM and cantilever magnetometry will be presented.

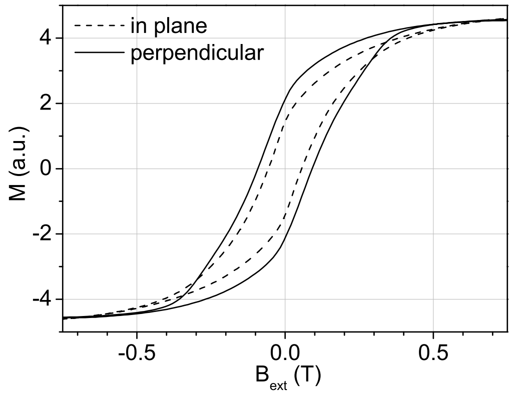

Figure 4.1: Hysteresis curve of an ensemble of FeCNT measured parallel to the sample plane (perpendicular to the nanotube axis, dotted line) and perpendicular to the sample plane (parallel to the nanotube axis, solid line). The curve represents an average over a large ensemble of nanowires with different switching fields and orientations.

4.1 MFM INVESTIGATIONS OF INDIVIDUAL FECNT

4.1.1 Sample preparation

In order to scan an individual FeCNT in the MFM, several steps of sample preparation are necessary. At first, the FeCNT need to be removed from the substrate. This is usually done by immersing the whole sample in ethanol followed by a short ultrasonification (∼30 s). The resulting solution contains FeCNT and other species from the as-grown sample, mainly bundled up in large agglomerates. In order to separate these, a further ultrasonification can be performed. However, it was found that extended ultrasonification tends to break the FeCNT into small pieces. In order to avoid this, a mechanical stirrer was used. Stirring for ∼1 min at 1000 rpm yielded a sufficiently good separation. Immediately after stirring, a drop of the solution was applied onto a clean silicon substrate with the help of a micropipette. After the evaporation of the ethanol, small bundles and ideally also individual FeCNT are distributed flat on the silicon surface. Heating the substrate can shorten the evaporation time and avoid the reagglomeration of FeCNT.

In the MFM, an external CCD camera only allows a coarse positioning of the sample with respect to the MFM probe. Finding an appropriate FeCNT without further information can be very time consuming. Because of this, the silicon substrate was first imaged in an SEM to locate individual FeCNT. In order to find the same FeCNT again in the MFM, silicon substrates with microscaled gold markers produced by photolithography were used. Fig. 4.2 a and b show such unambiguous marker structures that can also be seen with the CCD camera in the MFM. Once a filled CNT has been identified in the SEM using the BSE detector (Fig. 4.2 c and d), it can be found within a limited time in the MFM. The spacing between the markers is ∼25 µm, the

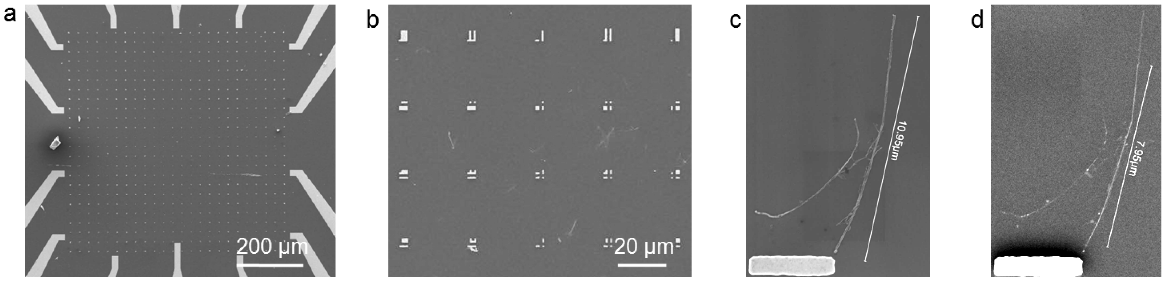

Figure 4.2: a) Silicon substrate with gold markers fabricated by photolithography. b) Close-up: Unique markers facilitate the orientation on the substrate. c) Two FeCNT laying flat close to a marker. d) BSED image revealing the iron filled part.

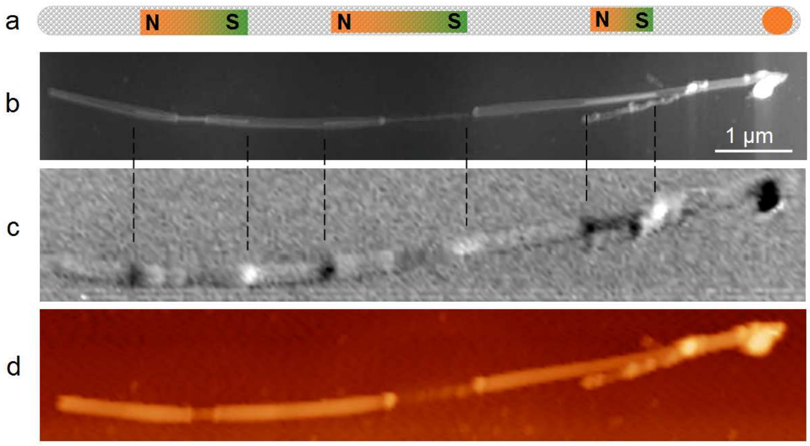

Figure 4.3: SEM and MFM image of a partially filled FeCNT. a) Schematic sketch of the FeCNT showing the position of the three separate enclosed iron nanowires. b) SEM image of the FeCNT, the iron filling is slightly visible. c) MFM image revealing the single domain configuration of the nanowires. d) AFM height image.

maximum scan range in the MFM is 40 µm, thus an orientation is possible already with the first coarse scan.

4.1.2 MFM measurement

All of the following measurements were performed in the Veeco DI 3100 AFM. The instrument yields a lower resolution than the high vacuum hrMFM, however, fast sample changes are possible. The individual FeCNT were imaged using conventional tapping mode AFM probes coated with 40 nm CoCrTa. Fig. 4.3 shows an individual FeCNT imaged in different modes. Fig. 4.3 b shows a SEM image of the ∼10 µm long FeCNT which is filled with three separate iron wires of different lengths. The sketch of the FeCNT in Fig. 4.3 a shows the position of the three enclosed wires. The right end of the tube is terminated by a large iron particle. Fig. 4.3 c displays the MFM scan taken in Lift Mode^{TM} at a tip-sample distance of 40 nm. The dotted lines between image b and c mark the positions of the nanowire ends. The left wire ends produce a black MFM contrast, the right ends a white contrast corresponding to a negative and positive phase shift respectively. The wire ends yield the maximum MFM signal. This signifies that the wires are magnetized along their long axis and consist of one **single magnetic domain**. Thus one can regard the nanowires as long nanoscale bar magnets as depicted in the sketch in Fig. 4.3 a. The magnetic field lines enter on one wire end and exit on the other end producing a z-component of the wire's stray field which is detected with the MFM probe magnetized along z. All three wires are magnetized in the same direction because a magnetic field was applied prior to the measurement. Directly after the growth this was not necessarily the case. The wires

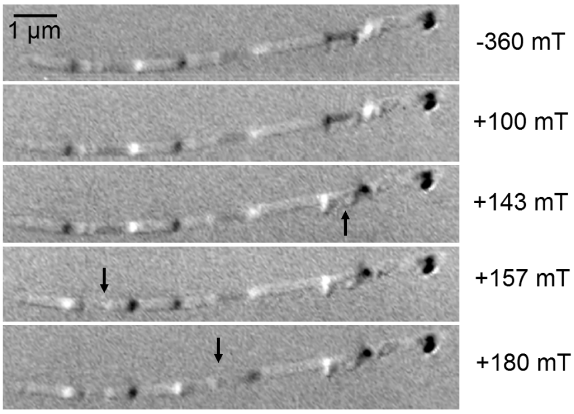

Figure 4.4: Series of MFM images taken after applying an increasing magnetic field antiparallel to the original iron wire magnetization. The three individual wires (arrows) switch their magnetization direction at different values of the external field.

within the FeCNT are spaced far enough from each other to be able to disregard any potential dipolar interactions between them. The resulting magnetic stray field at the wire end decays $\propto z^{-2}$ (in the monopole description of the wire end). At a wire diameter of ~30 nm the stray field at a distance of 1 µm smaller than 5 mT . Fig. 4.3 d shows the AFM height image of the FeCNT. Here it is clearly visible that parts of the FeCNT's shell have been removed, however, this does not have an influence on the results presented here. It rather states that although large parts of the shell have been removed, the iron core did not loose its magnetization due to oxidation.

4.1.3 Determination of the switching field of individual FeCNT

The switching field of a wire is defined as the field at which the wire magnetization is reversed. In the case of a rectangular hysteresis loop, it corresponds to the wire's coercivity. The switching field is an important feature to know for an application of FeCNT in sensing, magnetic data storage or other applications. In this section, the switching field of individual nanowires enclosed in FeCNT will be determined with MFM measurements performed after applying an external magnetic field. To do this, the nanowires within the FeCNT are first magnetized along one direction by applying a field of 0.4 T parallel to the tube axis using a calibrated electromagnet. Then an MFM image is taken. After this, the FeCNT is again exposed to a magnetic field, this time a weak field opposite to the original orientation. MFM scans and a further increase of the field in steps of ~20 mT are alternated until a switching is observed. Fig. 4.4 shows the resulting relevant images. The uppermost scan shows the initial magnetization of the wires. The right nanowire then changes its magnetization direction at a field between 100 and 143 mT, the left one between 143 and 157 mT and the middle one between 157 and 180 mT. The nanowires differ in length and diameter which might be a reason for the different switching fields. Also their orientation with respect to the external field varies slightly due to the curved nanowire.

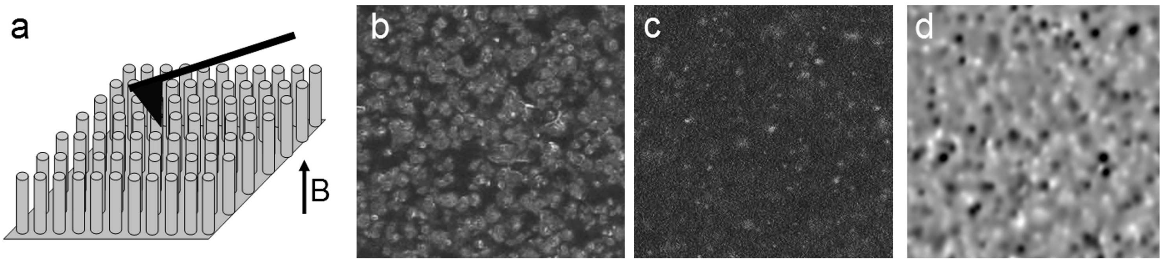

Figure 4.5: MFM study of FeCNT embedded in a polymer. a) Sketch of the experimental setup. b) SEM image showing the polished ends of the perpendicular FeCNT, 2 µm×2 µm. c) BSED image, the white dots represent the ends of filled FeCNT or iron particles, 2 µm×2 µm. d) MFM image showing the ends of iron nanowires magnetized in opposing directions as black and white dots (different area on the sample than shown in the previous images, 5 µm×5 µm).

In order to obtain more statistics on the switching fields of iron wires enclosed in CNT, a different sample was investigated. Fig. 4.5 a shows a sketch of an as-grown sample of FeCNT which has been embedded in a polymer matrix (tetraethoxysilane, TEOS) and polished down to approximately 5 µm remaining FeCNT length. The FeCNT are still aligned roughly perpendicular to the sample surface. In the SEM image in Fig. 4.5 b the open ends of the nanotubes can be seen. The BSED image of the same area (Fig. 4.5 c)shows some bright spots which represent the ends of filled FeCNT or iron particles. This flat surface can be scanned in the MFM to image the stray field gradient of the iron wire ends. Fig. 4.5 d shows such a scan, the white and dark spots represent wire ends of opposing polarity. The procedure described above to determine the switching field was performed with the external field applied parallel to the tube axes, perpendicular to the sample plane. Table 4.1 lists the measured field intervals and the number of FeCNT that switched their magnetization in the corresponding interval.

Table 4.1: Switching field distribution of FeCNT measured with MFM.

B (mT)	switched FeCNT
75-115	2
115-140	1
140-175	6
175-220	2
220-270	7

The range of switching fields is very large beginning at 75 mT and extending to 270 mT where most nanowires show a reversed magnetization. In further experiments, switch-

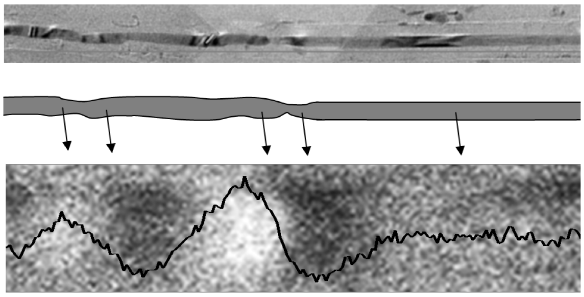

Figure 4.6: Parallel TEM and MFM investigations on the same FeCNT. Top: TEM image of a FeCNT section showing diameter variations of the iron core, image length 2.3 µm. Middle: Sketch emphasizing the diameter variations. Bottom: MFM scan of the same area revealing the associated magnetic stray field (superimposed: line scan).

ing fields of up to 400 mT could be observed, however, the majority of the investigated wires switched at fields between 100 and 300 mT. This value is much lower than the theoretically predicted shape anisotropy field ($\mu_0 H_k = 2K_s/M_s = \frac{1}{2}\mu_0 M_s$) of 1.1 T. This indicates that the reversal is not accomplished by a coherent rotation of the entire wire magnetization but rather by the nucleation and movement of one or more domain walls. However, in the MFM images only single domain states could be observed. In order to reliably investigate the reversal mechanism, other measurement techniques are more appropriate. Lipert et al.[9] used micro-Hall magnetometry to show the nucleation of the first small section of reversed magnetization in a nanowire via curling mode. Detailed information on the reversal mechanism of iron nanowires obtained by cantilever magnetometry measurements will be presented in section 4.2.

4.1.4 Combined TEM and MFM investigations on a FeCNT

As mentioned in section 2.3, the geometry of an iron nanowire has a great influence on its magnetic properties such as coercivity and switching field. Additionally, deviations from the ideal cylindrical structure can act as stray field sources or pinning centers for domain walls.[91] It is thus of great interest to correlate the MFM signal of an iron nanowire to its geometry. The resolution of the used SEM is too low for this purpose, a high resolution technique such as TEM needs to be used. However, there is the difficulty of finding a thin substrate for TEM investigations of FeCNT which can additionally be measured in an MFM. This problem was solved by using TEM grids which are covered with a thin layer of amorphous carbon as substrate for the FeCNT. The ~20 nm carbon film is thick enough to support the FeCNT but thin enough for a TEM measurement.

The samples were prepared by the technique explained in section 4.1.1, this time a drop of the FeCNT solution was applied onto a carbon covered TEM grid. The grid was then imaged in the SEM to find appropriate individual FeCNT. Their position could be easily documented by counting the grid holes. The chosen FeCNT was then measured in Lift Mode^{TM} MFM. Due to the large curvature of the carbon film the imaging was much more difficult than on a plane silicon substrate and the high resolution constant height mode MFM could not be applied. Often the residual topography signal was larger than the magnetic signal which made the image interpretation more difficult. Nevertheless several successful measurements could be performed. Fig. 4.6 shows a section of a FeCNT with a long continuous filling. On top, the TEM image can be seen. The iron nanowire is clearly visible. It exhibits several kinks and constrictions which are shown schematically below. The lowermost image shows the MFM contrast of the same region. It can be seen that a decreasing diameter is associated with a positive phase shift, an increasing diameter leads to a negative phase shift. The right nanotube part with constant diameter shows no additional MFM contrast. This proves that sites of changing wire diameter are additional sources of stray fields which can be observed with an MFM. The shown MFM signals do not indicate a multi domain state since the phase shift at the wire extremities is much larger than the shift shown in Fig. 4.6. The shown correlation of MFM contrast and wire geometry could not always be found. Some constrictions were not accompanied by an additional MFM signal, some signals could not be explained by diameter variations. A possible explanation for this could be that the TEM image only presents a projection of the nanowire onto one plane. The wire dimension perpendicular to the image plane cannot be evaluated.

4.1.5 Creation of a domain wall in a FeCNT

The growing interest in magnetic domain walls is partly driven by possible novel logic and memory applications based on domain walls.[1,92] The necessary control of the domain wall propagation and the magnetic switching can be achieved with pinning centers which provide well defined stable locations for domain walls. Notches or loop shapes have been used for this purpose in stripe-like nanostructures.[91,93] The observation of a domain wall in a FeCNT in the remanent state with MFM was so far not possible within this work. However, the deliberate introduction of a domain wall could in this case also be accomplished by the mentioned shape variations. Since constrictions in the iron nanowire geometry cannot be controlled like in a lithographical process, the formation of a loop structure was chosen.

Fig. 4.7 a and b show a FeCNT which is filled with an iron nanowire of more than 9 μm length. The BSED image clearly shows the long iron filling. The nanotube was scanned in the MFM revealing the expected single domain behavior of the wire reflected by the strong white and black contrast at its ends. The black arrow marks the nanowire's magnetization direction. In order to introduce a defined curvature into this FeCNT, the NanoMan mode of the Veeco DI 3100 AFM for direct nanoscale manipulation was

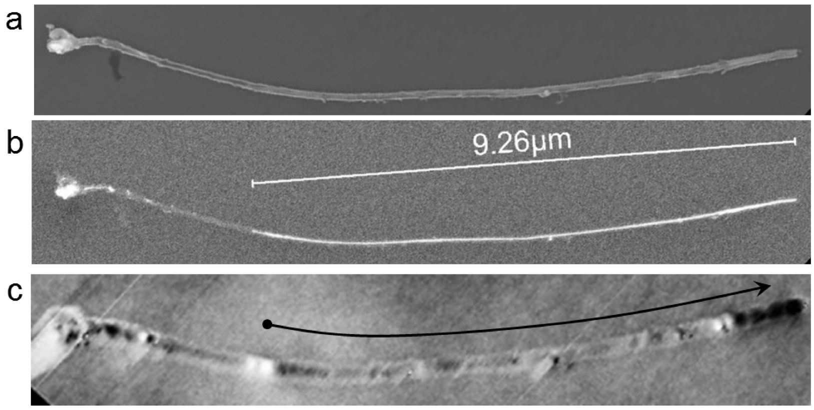

Figure 4.7: a) SEM image of a FeCNT laying flat on a substrate. b) BSED image of the same nanotube, the bright part on the right shows the long iron filling. On the left tube end several iron particles are visible. c) MFM image of the FeCNT. The long iron nanowire shows a single domain behavior reflected by the strong white and black contrast at its ends. The additional contrast within the wire length arises from diameter variations or decorating iron particles.

used. In this mode, a stiff AFM tip is used to scratch over the sample surface along a predefined path thereby either leaving a small trench or moving loose particles on the surface. Fig. 4.8 a shows the effect of such an operation on the once straight nanotube of Fig. 4.7 a. The AFM probe was positioned next to the FeCNT end and then moved in a >90° angle to the nanotube axis to bend the tube. The resulting scratch marks on the substrate surface can be seen in the lower right corner.

Directly after the manipulation the FeCNT was imaged again with the MFM (Fig. 4.8 b). The original domain structure of the nanowire is still present, the magnetization curves with the wire (black arrow). The FeCNT part with the minimum curvature radius shows a weak negative phase shift signal. This can be partially due to the magnetic stray field emanating from the bent region. However, it mainly results from the remaining topographic influence in the MFM image. This type of artifact occurs repeatedly in sample regions where the MFM probe is scanned parallel to the CNT axis. In order to introduce a domain wall, a magnetic field was applied along the direction marked in Fig. 4.8 c. The subsequent MFM image now shows that the original single domain state splits up into a two domain state by the formation of a domain wall at the bending site. The black arrows mark the new magnetization directions. This two-domain state was stable during repeated MFM scans. However, the insets in Fig. 4.8 c show that the position of the domain wall slightly shifts from one scan to another. This can be attributed to the influence of the magnetic tip. A MFM probe with a sufficient magnetic moment could thus be used to manipulate or drag a domain wall to desired positions.

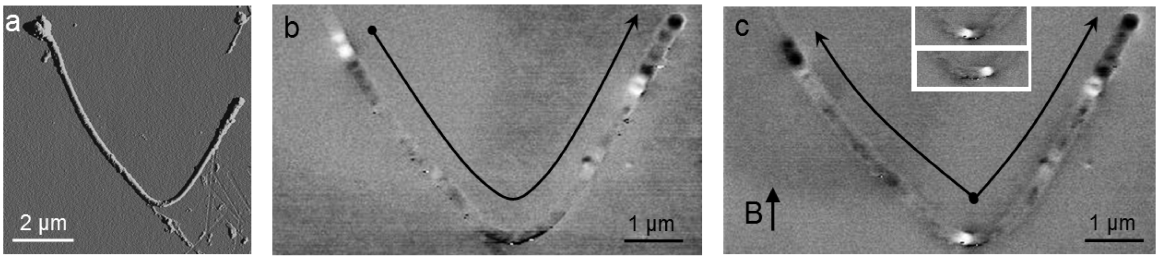

Figure 4.8: a) AFM amplitude image of the FeCNT shown in Fig. 4.7 a after bending. b) MFM image of the FeCNT after bending. The original domain structure is still present. c) MFM image of the FeCNT after applying an external field as marked by the arrow. The single domain state splits up into a two domain state. Insets: The position of the domain wall slightly shifts from one scan to another due to the influence of the MFM probe.

The shown results present only a first try on the deliberate formation and manipulation of domain walls in a FeCNT. Many more associated experiments can be envisioned. It would be interesting to investigate whether the domain wall is still stable when the FeCNT is bent back to the straight state. It might be pinned by defects in the nanowire geometry or propagate at once to the nanowire end. FeCNT with distinguished geometric variations could be chosen to analyze their influence on the domain wall behavior.

4.2 MAGNETIZATION REVERSAL IN AN INDIVIDUAL FECNT MEASURED USING CANTILEVER MAGNETOMETRY

MFM is an excellent tool to image the magnetic configuration of a FeCNT. However, it is not the method of choice to investigate details of the magnetization reversal and its mechanism. Extensive information on the switching behavior of an individual FeCNT can be obtained using vibrating cantilever magnetometry.[*] The investigation of magnetization reversal in ferromagnetic nanostructures is of much interest especially for potential applications in magnetic memory or logic.[1,92]

In cantilever magnetometry, the resonance frequency of a vibrating cantilever with the magnetic sample attached to it is measured as a function of an externally applied magnetic field. Stipe et al.[95] give the following model for the interpretation of the magnetometry data. The iron nanowire can be modeled as a single domain ferromagnet of volume V with saturation magnetization M_s and uniaxial anisotropy K_s. As the cantilever oscillates with a displacement x_c, the cantilever tilts by an angle β and the nanowire moment cants away from its easy axis by an angle θ due to the applied magnetic field along z (Fig. 4.10 a). For small oscillation amplitudes, $\beta = x_c/L_e$ where L_e is the effective cantilever length depending on the shape of the vibrational mode. For the first modes of a rectangular cantilever with length L, $L_e = L/1.38$. The tilt of the nanowire's magnetization can be determined by considering its magnetic energy which can be written as the sum of anisotropy and Zeeman energy terms:

$$E_m = K_s V sin^2\theta - \mu_0 H_{ext} M_s V cos(\beta - \theta) \tag{4.1}$$

with the wire's shape anisotropy $K_s = \frac{1}{4}\mu_0 M_s^2$, the wire volume V, the external field H_{ext} and the saturation magnetization M_s. The magnetocrystalline anisotropy contribution is neglected here. For iron it is much smaller than the shape anisotropy contribution as will be shown below. The minimization of E_m with respect to θ for small angles and the introduction of the anisotropy field $H_k = 2K_s/\mu_0 M_s$ yields

$$\theta = \frac{H_{ext}}{H_{ext} + H_k} \frac{x_c}{L_e} \tag{4.2}$$

---

[*] This work was performed in close collaboration with the group of Prof. Chris Hammel at the Ohio State University, Columbus, USA. The data presented in this section was measured and evaluated by Palash Banerjee et al.[94]

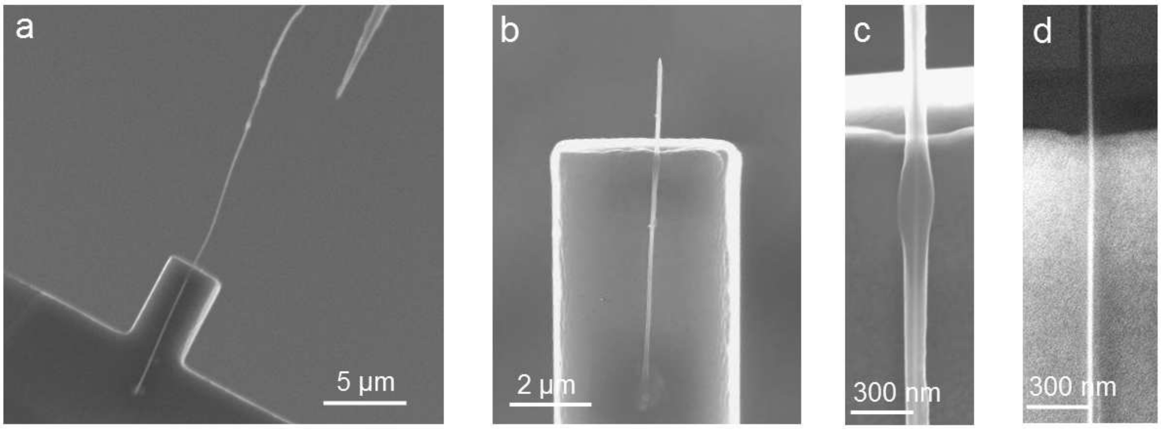

Figure 4.9: a) A FeCNT previously attached to a sharp tungsten tip (upper right) is transfered to the cantilever. b) The overhanging FeCNT was removed with the FIB. c) Detailed view of the FeCNT attached to the cantilever. d) BSED image of the same area showing the long continuous iron filling.

The x component of the nanowire's magnetic moment generates a torque on the cantilever:

$$\begin{aligned} \mathbf{T} &= |\mathbf{m} \times \mathbf{B}| && (4.3) \\ T_y &= \mu_0 M_s V H_{ext}(\beta - \theta) = \mu_0 M_s V H_{ext} \beta \frac{H_k}{H_{ext} + H_k} && (4.4) \end{aligned}$$

This torque ($\mathbf{T} = \mathbf{r} \times \mathbf{F}$) changes the cantilever's spring constant by $\Delta k = T/(x_c L_e) = T/\beta L_e^2$. For small $\Delta k/k_0$ the resulting cantilever frequency shift is $\Delta f/f_0 \approx \frac{1}{2}\Delta k/k_0$:

$$\frac{\Delta f}{f_0} = \frac{\mu_0 m_{NT} H_{ext} H_k}{2 k_0 L_e^2 (H_{ext} + H_k)} \tag{4.5}$$

with the nanowire moment $m_{NT} = M_s V$ and the cantilever spring constant k_0 and resonance frequency f_0 in zero field.

An individual FeCNT was attached to a silicon cantilever using the electron beam induced carbon deposition technique which will be described in more detail in section 5.2. Fig. 4.9 a shows how a FeCNT which was previously attached to a sharp tungsten tip is transfered to the cantilever. Prior to attaching the FeCNT, the cantilever was prepared by first removing its tip using a FIB leaving behind a flat surface on which to place the nanotube. In order to avoid an excessive vibration of the long nanotube during the measurement and to remove disturbing FeCNT parts, most of the overhanging FeCNT was cut off with the FIB (Fig. 4.9 b). The attachment site of the tube can be seen in Fig. 4.9 c. Fig. 4.9 d shows a BSED image of the same area, the long continuous iron filling of ∼25 nm diameter is clearly visible.

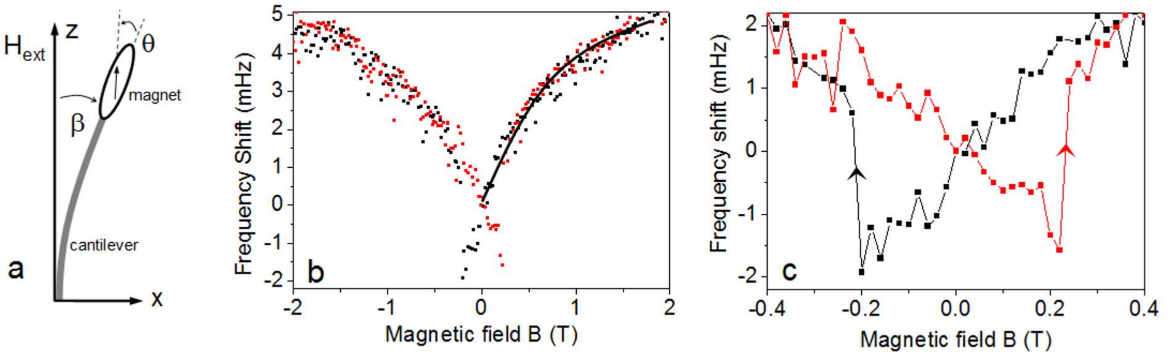

Figure 4.10: a) Geometry of the measurement with the external field aligned parallel to the long axis of the cantilever. b) Frequency shift hysteresis loop for a FeCNT attached to a cantilever. The shift in the cantilever's resonance frequency is plotted as a function of the applied magnetic field. c) Detail of the switching behavior. The nanotube moment switches in one discrete irreversible step marked by the arrows.

The cantilever with the attached FeCNT was oriented such that the external field was parallel to the FeCNT axis. A positive feedback loop drove the cantilever at its respective resonance frequency. The used cantilever had a resonance frequency of f_0=17.1414 kHz (at 6 K), an effective length L_e=312 µm and a spring constant k_0=0.157 N/m.

Fig. 4.10 b shows the cantilever's resonance frequency as a function of the applied magnetic field. Two field sweeps, from positive to negative field and vice versa, are shown in black and red. One branch of each sweep can be fitted using Eq. 4.5 with the iron nanowire's moment m_{NT} and the anisotropy field H_k as fitting parameters. The obtained values by a least-squares fit are m_{NT}=1.2·10^{-14} Am^2 and $\mu_0 H_k$=1.1 T. These results are consistent with the moment calculated from the approximate wire geometry (length 13 µm, diameter 25 nm) and the saturation magnetization of iron. The large anisotropy field is entirely due to the large shape anisotropy of the iron nanowire ($\mu_0 H_k^{shape} = \mu_0 M_s/2$=1.1 T), the magnetocrystalline anisotropy contribution of iron is much smaller ($\mu_0 H_k^{cryst} = 2K_1/M_s$=0.059 T).[94] The detailed view of the frequency shift hysteresis loop in Fig. 4.10 c and Fig. 4.11 b shows the abrupt reversal of the iron nanowire magnetization when a sufficiently large field antiparallel to its original direction is applied. The moment switches in a single step which can be seen by the discrete jump in the cantilever frequency at the switching field. The switching is attributed to the nucleation of a small volume of reversed magnetization and the corresponding insertion of a domain wall at one end of the nanotube. Once inserted the domain wall propagates through the wire reversing its magnetization.

In order to better understand the switching process, the switching event was repeatedly measured (approx. 150 times) at several temperatures. These statistics were

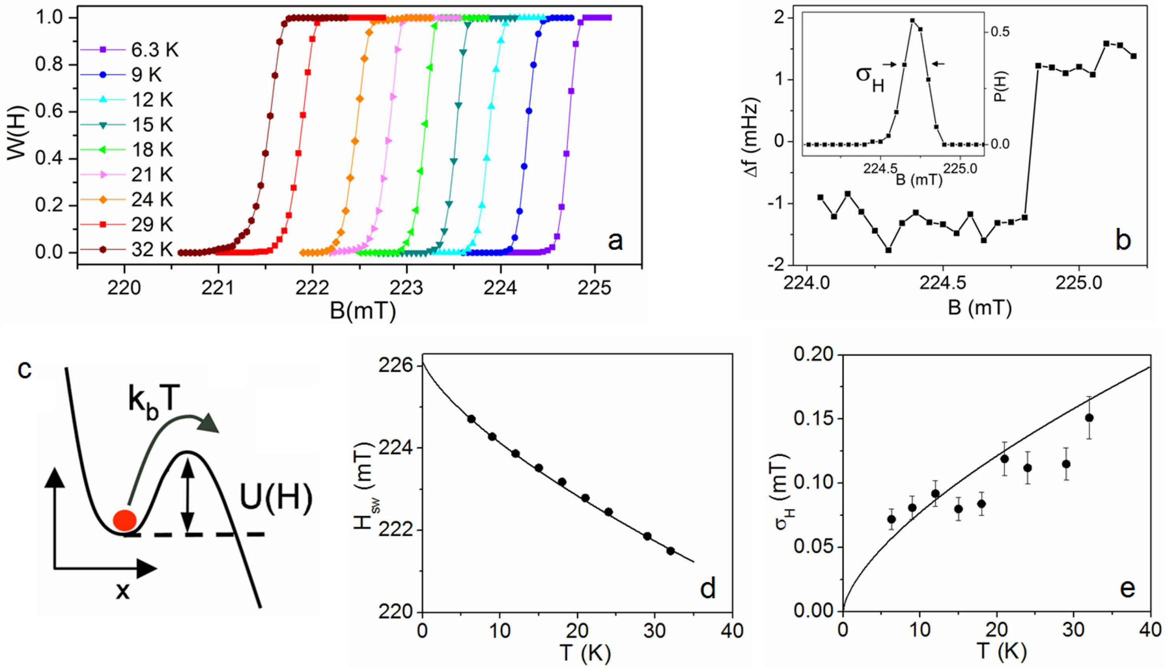

Figure 4.11: a) Cumulative probability of the switching of the FeCNT measured at different temperatures. b) High resolution field scan showing the abrupt switching. The inset presents a histogram of ~150 measurements of the switching event at 6.3 K with a very narrow distribution σ_H. c) Phenomenological model for a field driven thermally assisted reversal of the FeCNT magnetization. d) Temperature dependence of the mean switching field. The solid line shows a fit using Eq. 4.7. e) Width of the switching field distribution depending on the temperature. The calculated dependence using the fitted values is shown by the solid line.

compiled into a cumulative probability $W(H)$ that the FeCNT moment has switched once an applied magnetic field H has been reached and are shown in Fig. 4.11 a. In all cases, only a single switching event is observed. The switching field distributions can be described by a temperature dependent mean $H_{sw}(T)$ and width $\sigma_H(T)$ shown in Fig. 4.11 d and e. The mean switching field decreases from 224.71 mT at 6.3 K to 221.5 mT at 32 K. At the same time, $\sigma_H(T)$ increases from $7.2{\cdot}10^{-5}$ T at 6.3 K to $1.15{\cdot}10^{-4}$ T at 32 K. These results can be explained in terms of a thermally assisted magnetization reversal (see sketch in Fig. 4.11 c).[96] For a thermally assisted process, the escape rate over a barrier is of the Arrhenius form[97]

$$\Gamma(H) = \Gamma_0 \sqrt{1 - \frac{H}{H_c}}\, e^{\frac{-U(H)}{k_B T}} \tag{4.6}$$

where Γ_0 is an attempt frequency, $U(H)$ is the field dependent barrier, k_B is the Boltzmann constant and T is the temperature. The exact form of $U(H)$ for arbitrary values of the external field H is difficult to evaluate. However, close to the critical field H_c where the barrier disappears U(H) can be well approximated by a cubic potential.[97] The barrier depends on external field as $U(H) = U_0(1 - H/H_c)^{3/2}$ where U_0 is the magnitude of the zero field barrier height. Under these conditions, Garg[97] has shown that the mean switching field H_{sw}^m and the width σ_H of the distribution are given by

$$\frac{H_{sw}^m}{H_c} = 1 - (lnX)^{2/3} \left(\frac{k_B T}{U_0}\right)^{2/3} \tag{4.7}$$

and

$$\frac{\sigma_H}{H_c} = \sqrt{\frac{2\pi^2}{27}} \left(\frac{k_B T}{U_0}\right)^{2/3} (lnX)^{-1/3} \tag{4.8}$$

with

$$X = \frac{2k_B T}{3U_0} \frac{\Gamma_0 H_c}{dH/dt}$$

The solid line in Fig. 4.11 d shows a fit of Eq. 4.7 to the data to obtain the value of the unbiased zero field potential U_0=2.54·10^5 K and $\mu_0 H_c$=226.25 mT. A value of Γ_0=1.25·10^{10} s^{-1} is used for the attempt frequency consistent with magnetization precession frequencies in the local internal field of the iron nanowire.[94] These parameter values of U_0, H_c and Γ_0 were used to calculate the temperature dependence of σ_H shown by the solid line in Fig. 4.11 e. It can be seen that the measured values correspond well to the calculated behavior. The error bars represent the error in measuring the sample variance with 150 measurements, it amounts to 11% of the theoretically expected variance.

The large barrier U_0 is closely related to the energy required to fully insert a domain wall into the FeCNT in the absence of an external field. Assuming the FeCNT diameter d to be 25 nm, the energy of a domain wall[52] within the FeCNT is $\pi d^2 \sqrt{AK_s}$=4.3·10^5 K where A the exchange stiffness of Fe (Table 2.1) and $K_s = \frac{1}{4}\mu_0 M_s^2$=9.1·10^5 J/m^3 is the shape anisotropy energy of the nanowire (see Eq. 2.7). This is in good agreement with the deduced value of U_0=2.54·10^5 K given that the exact configuration of spins comprising the domain wall is unknown making estimates based on bulk parameters uncertain. Even though the zero field barrier U_0 is orders of magnitude larger than the available thermal energy, the barrier height is controllable via the external field. At 6.3 K, $\mu_0 H_{sw}^m$=224.71 mT corresponds to a barrier height of $U(H)$=142.6 K, while at 32 K, $\mu_0 H_{sw}$=221.5 mT corresponds to $U(H)$=772.7 K. Over the range of measured temperatures, H_{sw}^m corresponds to a barrier approximately 22-24 times $k_B T$.

The measurements presented in this section provide a thorough description of the magnetization reversal by the nucleation and propagation of a domain wall within the iron nanowire. The temperature dependence of the switching can be explained by a thermally activated process. Thus delocalized reversal mechanisms such as coherent rotation or curling of all spins within the wire cannot be applied for the FeCNT investigated in this study. Lipert et al.[9] investigated the magnetization reversal in a FeCNT with micro-Hall magnetometry in external fields at various angles with respect to the FeCNT axis. These measurements also suggest a thermally activated magnetization reversal, a small domain of reversed magnetization is formed at the wire end initiated by curling. This could also be the case in the measurement shown here, however, the domain formation mechanism was not investigated further.

5 Iron filled carbon nanotubes as probes for MFM

In the previous chapter magnetic characteristics of individual FeCNT such as their single domain character and high switching fields along the easy axis were investigated. In the following these attractive properties will be of use to fabricate probes for magnetic force microscopy based on an individual FeCNT.

5.1 Preliminary considerations on MFM probes

With an ever decreasing size of the structures of interest there is a need for MFM probes with a smaller tip diameter for high resolution imaging. Moreover, despite extensive studies of the image formation process, a reliable quantitative evaluation of the MFM data is still difficult to obtain and restricted to special cases due to the complex magnetic structure of magnetically coated MFM probes. Several theoretical investigations have been conducted, e.g. on the tip-sample-interaction[70] or micromagnetic models of the MFM response.[73] There is also framework to perform the image analysis in the Fourier domain using transfer function theory.[74,75] One of the most commonly used MFM sensor calibration approaches is the point probe approximation[71] which attributes all effective magnetic moments of the MFM tip to a point dipole or monopole within the real probe (see section 3.3.3.2). Various calibration structures that provide a defined magnetic field such as current lines,[18,77] current rings,[17] or magnetic hard discs[12] have been used to determine the point pole and its position within the MFM probe. All these evaluations can be further complicated due to the perturbation of the sample magnetization by the MFM tip or vice versa. In addition, the application of calibrated conventional probes is restricted to samples with similar magnetic stray field geometry as that used for calibration. To measure a sample with different magnetic structure geometries which interact with a different effective probe volume, a new calibration with analogous features needs to be performed (Fig. 5.1, left side). This

Figure 5.1: Schematic comparison between a magnetically coated MFM probe and an extended dipole probe. Depending on the sample stray field geometry, different volumes of the magnetic coating of a conventional probe are involved in the imaging process (left). In the case of a rod-shaped magnetic dipole longer than the stray field's decay length only the lower monopole takes part in the interaction (right). Knowledge of its value and position leads to a universal probe calibration.

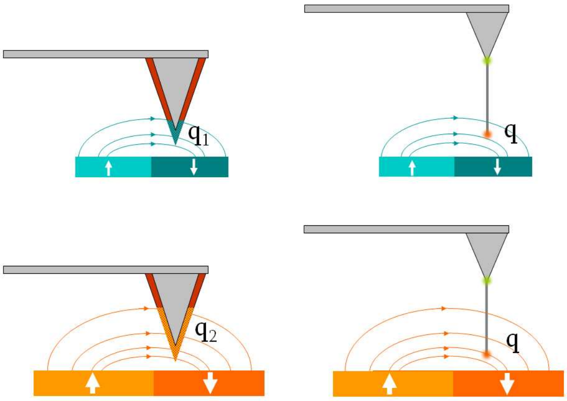

is time consuming and restricts the accuracy of the obtained data. The calibration would be much simpler in the case of a probe shaped like a long cylinder of homogeneous diameter magnetized along the cylinder axis, here referred to as an extended dipole probe, suggested as the ideal sensor shape over 10 years ago.[98] As long as the distance between the long wire's opposing monopoles is larger than the decay length of the sample's magnetic stray field only the monopole close to the sample surface is involved in the tip-sample-interaction (Fig. 5.1, right side). Consequently, knowledge of the value of the lower monopole and its position leads to a universally applicable MFM probe calibration and the possibility of straightforward quantitative MFM measurements. This very attractive advantage of an extended dipole tip is also supported by the force transfer function approach by Hug et al.[74] Within this concept the tip can be approximated by a point charge if the diameter of the elongated tip is smaller and its length is larger than the size of the magnetic structures to be investigated. The force acting on the probe is then proportional to the sample's stray field.

Experimental approaches for the fabrication of such a probe have been demonstrated, e.g., by Saito et al.[80] with the CantiClever design where a bar shaped magnetic sensor is obtained by the deposition of a Co layer on the side of a freestanding SiN plane (see section 3.3.3.3). These approaches yield high resolution tips with a better defined magnetic volume than that of a conventional probe. However, the ferromagnetic coating is not protected and thus subjected to oxidation and abrasion. In addition, a universal calibration of these probes has not been demonstrated.

According to the previous considerations, the ideal MFM probe would be a long ferromagnetic cylinder of known constant diameter in the order of or smaller than the magnetic structure of interest. In addition, it should have well defined magnetic properties such the switching field and a magnetic moment aligned and fixed along the cylinder axis. It should keep these properties over a long lifetime without a change of geometry or magnetic properties. A carbon nanotube enclosing a cylindrical iron ferromagnet with a diameter in the nanometer range and a length of several microns is an ideal candidate for such a MFM probe. Its dimensions fit perfectly to the force transfer function approach mentioned earlier, the point charge approximation is in this case valid for samples with magnetic feature sizes ranging from some tens of nanometers to some micrometers. This covers the magnetic feature sizes of main interest in MFM investigations. It has already been shown[8] that carbon nanotubes reveal great potential as probes for atomic force microscopy. A FeCNT probe is equivalently advantageous for MFM. Carbon nanotubes are known for their outstanding mechanical and chemical stability thus ensuring a long probe lifetime. The ferromagnetic filling enclosed in the carbon shells is protected from oxidation and maintains constant magnetic properties. The small diameter of the filling allows imaging with a high lateral magnetic resolution and less influence on the sample magnetization. Additionally, the large shape anisotropy of the enclosed iron wire far exceeds other anisotropy contributions, e.g. magnetocrystalline anisotropy, and leads to a stable magnetization along the long wire axis and a high switching field. Consequently, the tip magnetization is also less likely to be perturbed by the sample's stray field and a more accurate quantitative data evaluation is possible.

5.2 PROBE PREPARATION

Previous experiments showed that the direct growth of an individual aligned and continuously filled FeCNT on the tip of an atomic force microscopy cantilever is hard to achieve.[99,100] Winkler et al. investigated several routes such as the use of growth inhibiting gold layers or the local application of catalyst material to restrict the FeCNT growth to a small part of the cantilever. However, these approaches posed several problems. The gold layer was not able to prevent the growth of FeCNTs in all unwanted regions due to preexisting or high temperature induced defects in the layer. Furthermore, the alignment of FeCNTs is to a large extent due to their growth as a compact body. If separated FeCNTs are grown, they do not have the tendency to align perpendicular to the substrate surface plane. Thus, for the preparation of FeCNT MFM probes we chose the local attachment of a selected FeCNT to an AFM cantilever tip.[99,101] The following procedure is used: First, many FeCNTs are grown by CVD on a catalyst-coated silicon substrate. One of these nanotubes is then attached to a conventional AFM tip using a SEM equipped with a micromanipulator. After this, the fabricated probe is inspected and can, if necessary, be tailored by etching off unwanted carbon parts by localized electron-beam induced oxidation in a SEM or by cutting off these parts with a FIB. In the following sections each of these steps will be explained in more detail.

5.2.1 Attachment of an individual FeCNT to a conventional AFM probe

The FeCNTs prepared by CVD as described in section 3.1 are favorable for the probe preparation as they do not form a uniform body of tightly packed nanotubes of equal length. Some of the nanotubes are longer than others and stick out of the "nanotube forest". This makes them easily accessible for manipulation, the cantilever tip can be navigated close to the chosen nanotube with a micromanipulator.

For this process, a SEM equipped with a Kleindiek three-axis micromanipulation system is used. The FeCNT sample is broken in two such that a clean edge with exposed nanotubes is formed. The sample is then placed in the SEM with the breaking edge facing the electron gun so that the nanotubes can be seen in their full length. A conventional AFM cantilever is attached to the tip of the micromanipulator and rotated until the cantilever chip is approximately parallel to the FeCNT sample plane to assure that the attached nanotube will be roughly aligned with the cantilevers oscillation direction. The cantilever is then moved towards an individual FeCNT un-

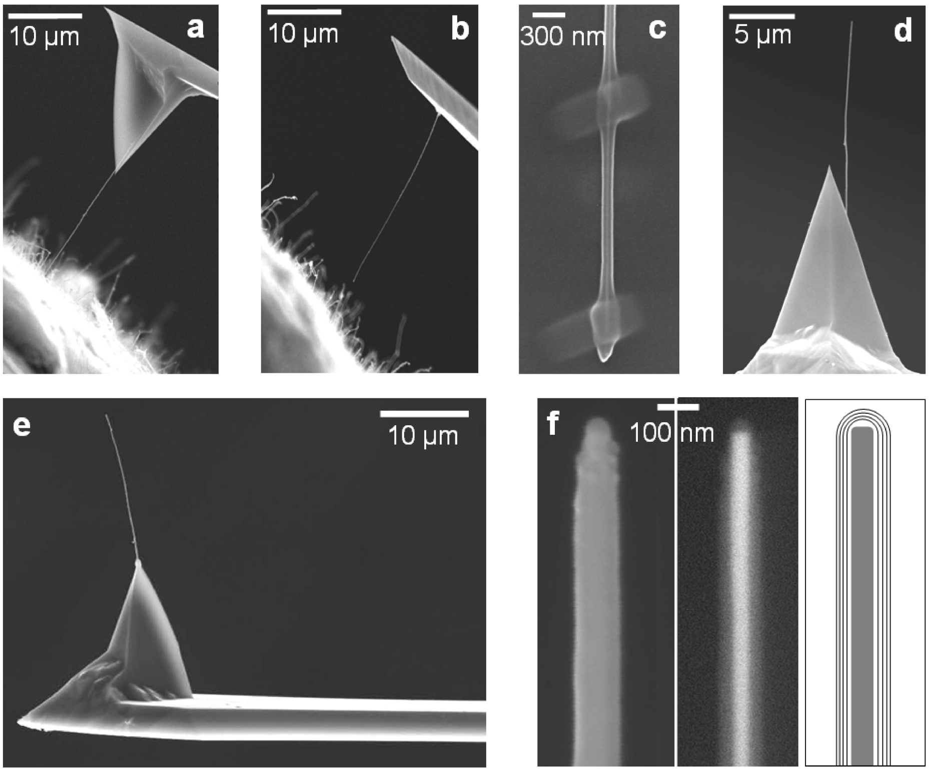

Figure 5.2: SEM micrographs of FeCNT MFM probes. Individual FeCNTs are attached to a) a conventional AFM cantilever and b) a tipless cantilever with the help of a micromanipulation system. c) Amorphous carbon deposits attach the FeCNT to the cantilever. d) and e) FeCNT MFM probes. f) The top part of the FeCNT attached to an AFM probe. Left: SEM image. Middle: Backscattered electron contrast (the bright region of the nanotube is iron filled). Right: Schematic sketch. The iron filling extends to the very end of the nanotube ensuring a small probe-sample distance. The filling is completely surrounded and protected by carbon shells.

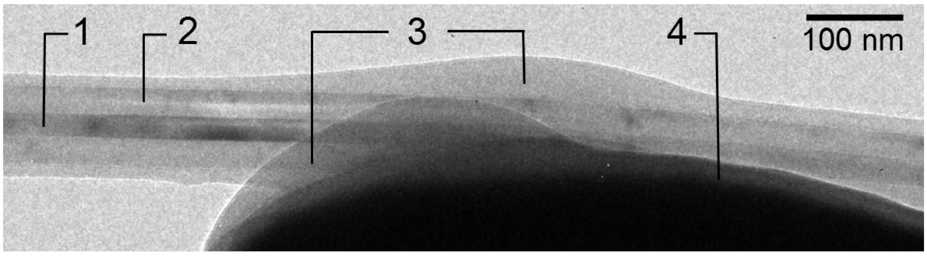

Figure 5.3: TEM micrograph of a FeCNT attached to a silicon cantilever. 1- Iron filling, 2- Carbon shells, 3- Amorphous carbon deposition, 4- Silicon cantilever.

til the end of the nanotube touches the cantilever tip (Fig. 5.2 a and b). The small area of the nanotube in contact with the cantilever surface is then scanned with the primary electron beam at a high magnification (≈100,000×). This leads to the deposition of amorphous carbon in this area, e.g., from remaining hydrocarbons in the microscope chamber (Fig. 5.2 c and Fig. 5.3). After that, the cantilever is retracted, thereby pulling the attached nanotube off the substrate surface. Two examples of the resulting probes can be seen in Fig. 5.2 d and e. Fig. 5.2 f shows the very end of such a probe and a sketch illustrating that the iron filling extends to the very end of the nanotube ensuring a small probe-sample distance. Carbon shells completely surround and protect the iron wire. The connection between nanotube and cantilever tip proves to be very stable. The nanotube remains unchanged on the cantilever tip even after multiple tapping mode AFM scans or bending processes in the SEM while the probe is still attached to the micromanipulator.

5.2.2 Tailoring fabricated tips with a focused ion beam

Some nanotubes attached to cantilevers show properties that are not advantageous for MFM imaging. This includes unfilled nanotube parts and iron particles (e.g., remaining catalyst particles) on the ends of nanotubes. In order to improve these probes, it is possible to cut off unwanted tube parts with a focused ion beam (FIB). In Fig. 5.4 such a process is shown. The original FeCNT attached to the AFM cantilever contains two smaller iron nanowires (1-2 µm) at the tube ends and a larger one (9 µm) in the center (Fig. 5.4 a). In order to use the longer wire as scanning probe, the tube end was cut using a gallium ion beam at 16 kV and a current of 0.6 pA (lowest possible). It was observed in previous experiments that the filled or unfilled nanotube parts processed with a FIB at higher beam currents can bend at the cutting site towards the incoming beam (e.g., due to Ga-ion implantation, see Fig. 5.4 e). This makes them unusable as MFM probes. At lower currents this damage is reduced. A scan window of ≈500×300 nm was moved along the nanotube, thereby successively removing its top part. To avoid further damage of the nanotube by imaging it with the ion beam, no images were made during FIB cutting. Due to this, the actual cutting progress was hard to estimate and a larger part of the tube than originally intended was removed. Fig. 5.4 b shows the final state. The FeCNT was shortened by ≈8 µm and now has a 1.3 µm long nanowire at its end which can be used for MFM imaging. To see whether the cut FeCNT end remains open, two samples that were cut with a FIB were investigated in a TEM (Fig. 5.4 c and d). A 5-20 nm thick film (most likely amorphous carbon) covers the cutting site. It is unclear how this layer is formed, it could be a result of imaging in the SEM or TEM (similar to the deposition formed

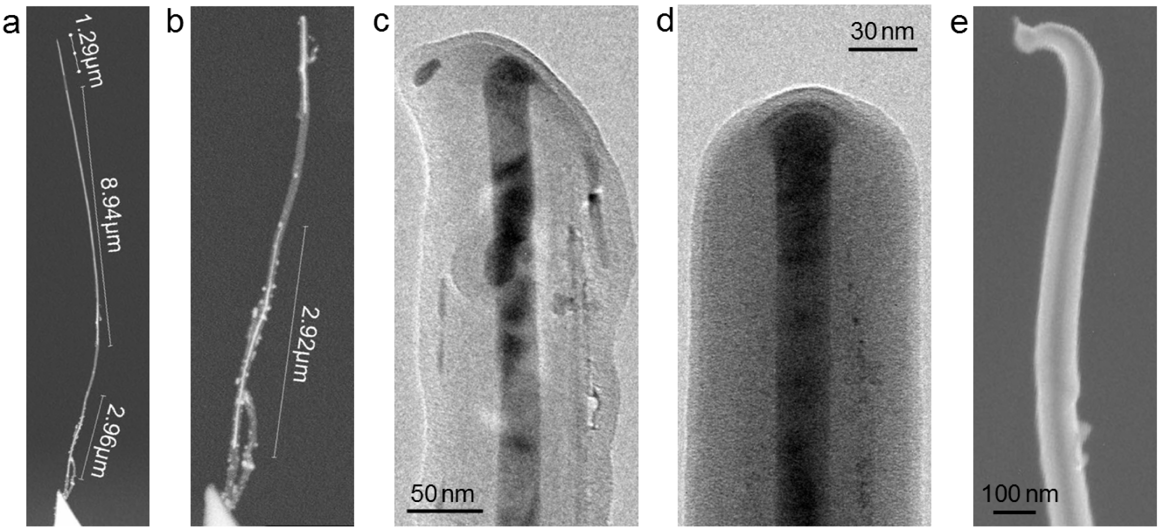

Figure 5.4: SEM and TEM images of FIB-cut FeCNT. a) Backscattered electron contrast of the original FeCNT filled with three iron nanowires. b) The same FeCNT after cutting off several microns with the FIB. c) and d) TEM images of two cut FeCNT ends. A thin carbon layer covers the iron core. e) SEM image of a FeCNT FIB-cut at higher ion beam currents. The end is bent due to ion beam induced damage.

for attaching the FeCNT to the cantilever). Since all FeCNT probe manipulation described here takes place in a SEM, it is most likely that the ends of all cut FeCNTs obtain an amorphous carbon cover of changing thickness depending on the imaging time and parameters. This prevents an oxidation of the filling but at the same time increases the minimum probe-sample separation due to a bigger carbon shell size.

5.2.3 Tailoring fabricated tips by localized electron-beam induced oxidation

Electron-beam induced oxidation of carbon is known to be able to locally remove parts of carbon nanotubes.[102] It is a useful alternative to using a focused ion beam for cutting off unfilled FeCNT ends or reducing the shell diameter as there is less damage induced to the iron filling and the carbon shell. A disadvantage is that no iron particles can be removed with this technique. Various process parameters can lead to the desired results. In the following, one example for such a local oxidation will be explained.

For electron-beam induced oxidation, the chosen MFM probe is oriented in the SEM in a way that the attached tube can be seen in full length. To distinguish the filled from the unfilled nanotube parts, a backscattered electron detector (BSED) is used. After focusing the electron beam in high vacuum on the empty nanotube part to be removed, the microscope chamber is filled with water vapor at a pressure of 0.2 mbar. A small scan window is placed only over the area to be oxidized, and the electron

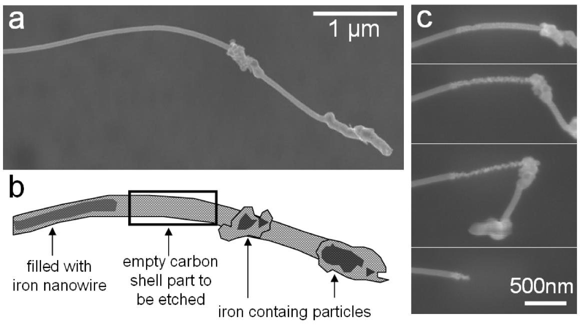
a
1 µm
b
filled with iron nanowire
empty carbon shell part to be etched
iron containg particles
c
500nm

Figure 5.5: a) SEM micrograph and b) schematic image of a partially iron filled CNT. The iron nanowire does not extend to the end of the tube. Instead, there are iron containing particles. To remove the tube end, localized electron-beam assisted etching was performed in the boxed region (b). c) Progressing oxidation of the carbon shell until complete removal.

beam is scanned at an acceleration voltage of 10 kV and a current of approximately 2 nA. Depending on the window size and the thickness of the carbon nanotube, the exposure time until all carbon in the selected area is removed varies from 30 s to 5 min. In Fig. 5.5, such a process is depicted. Fig. 5.5 a shows the end of the original nanotube attached to the probe. The end of the nanotube which is supposed to interact with the sample stray field is unfilled and covered with multiple iron and carbon particles. The long iron filled nanotube part further back (see sketch in Fig. 5.5 b) would be more appropriate for the tip of the MFM probe. In order to “cut off” the disturbing part, the empty carbon shell between the long, filled center part and the nanotube end is removed by scanning it with a scan area of approximately $150\,\text{nm} \times 1\,\mu\text{m}$. It had been observed in previous experiments that when scanning only a small part of a nanotube to produce a cut, the nanotube end tends to bend by 180° due to electron beam induced defects. It then sticks to the rest of the tube instead of being cut off. Therefore, we chose to scan a larger area to avoid this process. It can be seen in Fig. 5.5 c that the front part of the tube bends over while the etched part gets thinner, but eventually it is completely removed. Now the iron nanowire is located at the tube end and can be used for MFM imaging.

A second example of the improvement of a FeCNT MFM probe by localized electron-beam induced oxidation is shown in Fig. 5.6. In Fig. 5.6 a, it is clearly visible that the iron wire inside (darker contrast) does not extend all the way to the tube end. This unfilled nanotube section of about 100 nm increases the effective distance between sample surface and iron nanowire probe causing the poor MFM phase contrast shown on the right (magnetic hard disc sample). In Fig. 5.6 b, the extra carbon is removed and the nanotube tip is sharpened, leading to strongly enhanced MFM intensity and resolution at the same probe sample distance.

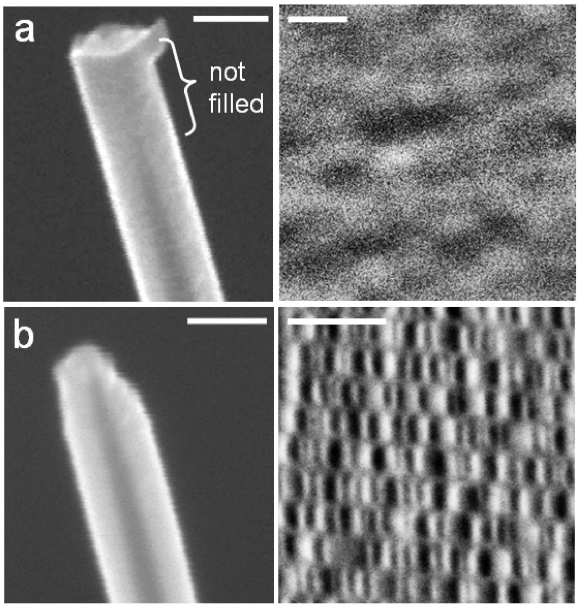

Figure 5.6: Left: SEM micrograph of the end of a FeCNT MFM probe a) before and b) after removal of the empty carbon shell at the tube end. Right: MFM images taken with the corresponding probe. A clear improvement in lateral resolution can be seen. Scale bar in SEM micrographs: 100 nm, in MFM images: 1 µm.

5.3 MFM MEASUREMENTS WITH FECNT MFM PROBES

Each fabricated tip was tested in a Veeco DI 3100 AFM for its applicability as an MFM probe in tapping mode (AFM) and Lift Mode^{TM} at a lift height of 50 nm (MFM). For a test sample, a conventional magnetic hard disk was used. The magnetic bits are magnetized parallel or antiparallel to the MFM probe magnetization corresponding to black and white in the MFM image. In Fig. 5.7, SEM micrographs of four FeCNT MFM probes are shown along with an AFM height image and MFM phase image taken with the corresponding probe. The behavior of most nanotube probes during approach to the sample surface was not different from what is observed when working with coated MFM tips. Most probes allow excellent topographic imaging even with a nanotube length of up to 20 µm. This is a sign of extraordinary stiffness of the filled nanotubes. The thermal vibration amplitude x of a nanotube can be estimated by equating the thermal energy $\frac{1}{2}k_B T$ with the potential energy of the lateral nanotube bending $\frac{1}{2}k_{CNT}x^2$:[103]

$$x = \sqrt{\frac{k_B T}{k_{CNT}}} \tag{5.1}$$

To determine the nanotube force constant for lateral bending, k_{CNT}, the CNT attached to the cantilever can be approximated as a one side clamped beam of circular cross section:

$$k_{CNT} = \frac{3\pi E r^4}{4L^3} \tag{5.2}$$

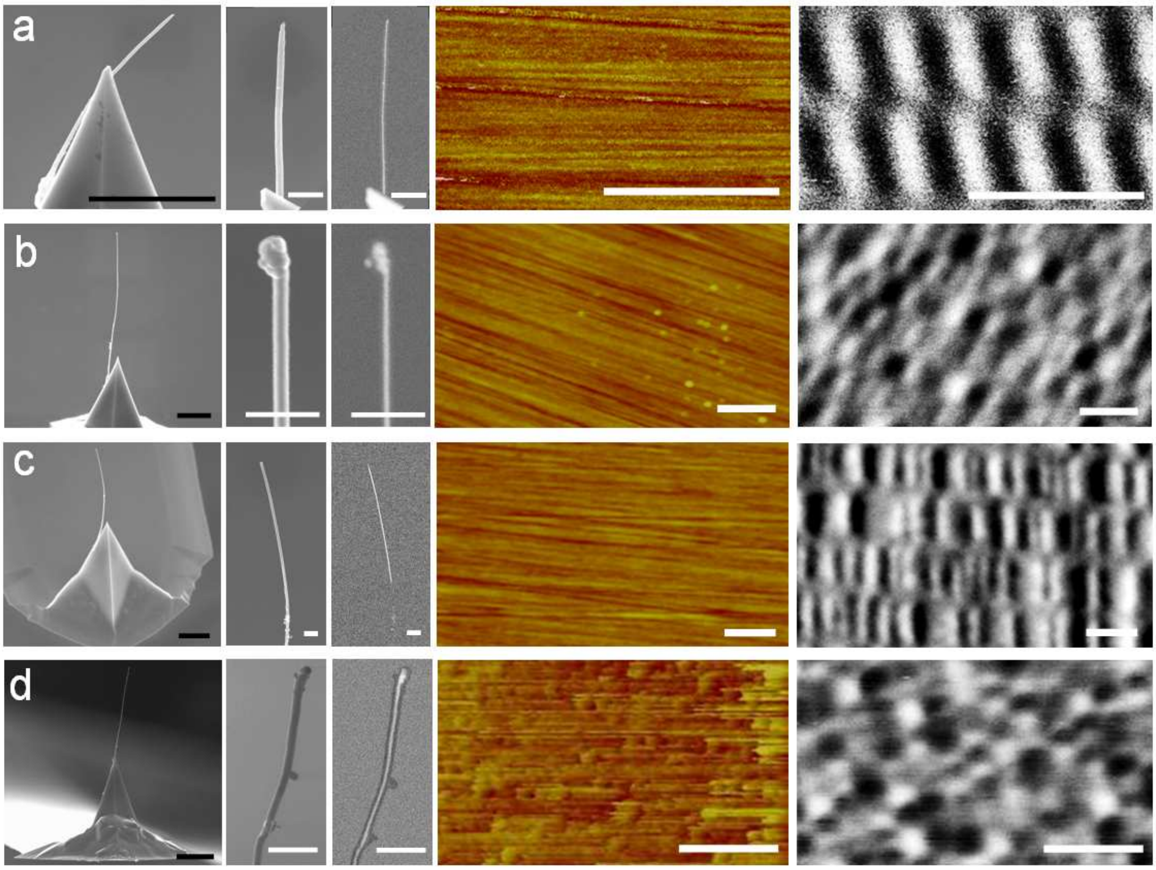

Figure 5.7: MFM test of four different FeCNT MFM probes. For a) to d) from left to right: SEM micrograph of the probe; zoomed in SEM micrograph of the tip of the attached nanotube; backscattered electron contrast SEM image of the same region, the bright part shows the enclosed iron; AFM height image of the test sample (magnetic hard drive) measured with the fabricated probe; MFM phase image of the same area. AFM height scale: 10nm. MFM phase scale 2°. White scale bar: 500 nm; black scale bar: 4 µm.

with the nanotube length L, radius r and its Young's modulus E. For the probe shown in Fig. 5.7 c with a nanotube length of 13 µm, a diameter of 100 nm and a Young's modulus E=400 GPa,[104] Eq. 5.1 and 5.2 yield a force constant of 3 mN/m and a thermal vibration amplitude of 1.2 nm at T=300 K. This would hardly be noticed even in a high resolution MFM scan (see section 5.4). This approach does not consider the properties of the CNT attachment or the influence of the iron filling, however, the obtained result can still help to understand the FeCNT probe's mechanical behavior.

The probes that were found to be suitable for AFM also show good MFM contrast and resolution. However, in some cases tapping mode imaging was not possible or only with artifacts in the resulting topography image (see Fig. 5.7 d). A possible reason might be that due to its low force constant, the FeCNT can stick to the sample surface at small probe sample distances. Another reason could be a poor attachment of the nanotube to the cantilever (weak connection) or defects in the FeCNT that lead to reduced rigidity.

FeCNT probes that did not allow imaging in the tapping mode were subsequently tested in constant height mode MFM in the Nanoscan hr-MFM. In this imaging mode, almost all FeCNT probes with iron filling at the very tube end yielded good MFM images. Thus, the problems in tapping mode described above are probably due to adhesion between FeCNT and sample. Non-contact mode might consequently be suited better for this kind of probes.

For the aim of quantitative MFM measurements, iron cylinders or needles with constant diameter, as shown in Fig. 5.7 a and c, are favorable. For qualitative MFM imaging, nanotubes with particles on the end (Fig. 5.7 b and d) work just as well, although the larger particle diameter reduces the topographic and magnetic resolution. The quality of the magnetic image strongly depends on size and position of the iron contained in the nanotube. In general, the larger the iron filling and the closer it is located to the end of the nanotube, the stronger is the MFM phase contrast. The probe magnetic dipole moment $m = M_s \, \pi \, l \, r^2$ depends on the iron wire length l and radius r. M_s is the saturation magnetization of iron. If only the monopole moment at the wire end interacts with the sample stray field, the length of the nanowire can be omitted. Considering an iron nanowire length of 5 µm and a magnetization of $1.76 \cdot 10^6$ A/m, the magnetic monopole moment varies from $5 \cdot 10^{-10}$ to $5 \cdot 10^{-8}$ Am and the dipole moment from $3 \cdot 10^{-15}$ to $3 \cdot 10^{-13}$ Am^2 for wire diameters of 10 to 100 nm. Applying the point probe model, Lohau et al.[17] obtained values of 10^{-8} to 10^{-7} Am for the monopole moments and 10^{-14} to 10^{-13} Am^2 for the dipole moments of thin film MFM tips. So the moment of the carbon nanotube tips is not necessarily smaller than the moment of today's thin film MFM tips, but much more localized. It can be varied to some extent, depending on the geometry of the chosen nanotube.

Concerning the probe lifetime, all working FeCNT probes so far (after more than 100 working hours) show no changes in their mechanical and magnetic properties. Even after rigorous physical contact to the sample surface which would have damaged the brittle tip of silicon probes no probe deterioration could be observed. From FeCNT manipulation in the SEM it is known that the nanotube will just bend when encountering an obstacle returning elastically back to its original shape without noticeable damage.

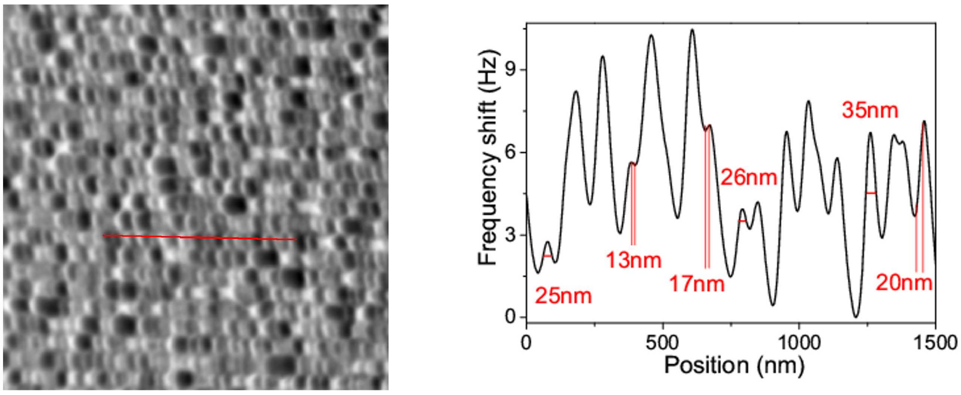

Figure 5.8: Left: 3 μm×3 μm MFM scan of a magnetic hard disc made with a FeCNT MFM probe. Right: Section along the red line, an average over 3 scan lines is displayed revealing features with widths ranging from 13 to 35 nm.

5.4 MAGNETIC RESOLUTION OF FECNT MFM PROBES

To test the achievable magnetic resolution of a FeCNT MFM probe it was tested on high density magnetic storage media. The measurements were performed in constant height mode in the Nanoscan hr-MFM in high vacuum. Fig. 5.8 shows a 3 μm×3 μm scan of a 320 GB Western Digital hard disc. To determine the resolution in this case, a line section through a row of bits was extracted. Peaks with a width of 25-35 nm can be found and some smaller features with widths below 20 nm appear as shoulders on bigger peaks. Thus the magnetic resolution of the FeCNT MFM probe comes close to the so far maximum reported resolution of 10 nm.[15,84]

The magnetic hard disc shown in Fig. 5.8 has an average bit size of ≈ 30 nm×100 nm. This is too large to really test the maximum possible resolution of the fabricated probes, other samples with smaller domain sizes need to be found. It is known that magnetic multilayers with strong perpendicular anisotropy[105] form sub-micron sized stripe or bubble domains depending on the external magnetic field. However, MFM measurements with FeCNT probes showed that the minimum stripe domain width is in the range of 50 nm which is still too large. Another option is the use of magnetic nanoparticles, e.g., synthesized from a gas aggregation source.[106] In this work, Co and Fe nanoparticles with a diameter of 5-10 nm deposited onto silicon substrates were used. Fig. 5.9 shows an MFM scan and two line sections of such a sample measured with a FeCNT probe. The obtained MFM contrast mainly shows features with full width at half maximum of 50-80 nm and rarely some smaller substructures of 20-30 nm width. Consequently, only larger particles or particle aggregates are detected (even small superparamagnetic particles should give a negative frequency shift contrast in MFM if the resolution of the probe is high enough). Also, larger dirt particles on

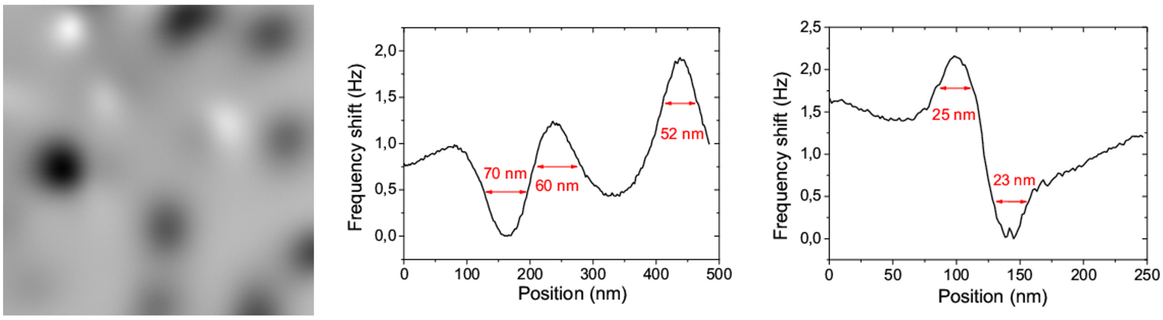

Figure 5.9: Left: 800 nm×800 nm MFM scan of iron nanoparticles made with a FeCNT MFM probe. Right: two line sections taken from MFM images of iron nanoparticles.

the substrate surface prevented the tip from approaching close enough to the sample surface to get a better resolved signal from the smaller sized particles.

The maximum obtainable resolution is related to the dimensions of the magnetic probe which is exposed to the sample stray field and to the probe-sample distance. Thus in order to improve the lateral resolution, it is necessary to reduce the magnetically sensitive part of the probe to a small size and to operate the probe in close proximity to the sample surface. FeCNT probes already feature a nanscale diameter of the magnetically active part. Thus the resolution could be enhanced by choosing nanotubes with a very thin carbon shell to reduce the probe-sample distance. Due to the time consuming preparation procedure of the FeCNT probes and the more difficult handling of thinner FeCNT this was not attempted so far.

5.5 Behavior of FeCNT MFM probes in external magnetic fields

In the last years, much progress has been made to adjust the MFM technique to the needs of special applications. To directly observe the magnetization reversal mechanism and domain evolution in magnetic materials, MFM systems for imaging samples in an external magnetic field have been developed.[107,108] For this application it is necessary to consider that also the magnetic tip is subjected to the applied field. The probe magnetization will change depending on the magnitude and orientation of this applied field which leads to changes in the resulting MFM image. It can then be necessary to use special calibration samples in order to determine the magnetization state of the probe in the external field for a clear evaluation of the MFM data.[109] In some cases the reorientation of the probe's magnetization along the external field might be an advantage, e.g., to selectively image specific components of the sample stray field.[108] However, when only the perpendicular sample stray field component is to be imaged depending on the external field, this is an unwanted effect. According to Babcock et al.[107] there are two possibilities for these kinds of experiments to avoid an unpredictable canting of the probe moment. First, a tip with a coercivity much larger than the applied field can be used. The second alternative is a very soft magnetic tip whose magnetization is always aligned with the total local field in a defined way. However, the magnetization direction of such probes can still differ from that of the sample making the image interpretation difficult.

In this section the behavior of a FeCNT MFM probe in an external magnetic field parallel to the sample plane is investigated and compared to two different kinds of probes. For this application, the high aspect ratio and thus the large magnetic shape anisotropy of the iron nanowire contained in the FeCNT is a great advantage. The wire's magnetization is stabilized along its long axis even in a moderate external field perpendicular to this easy axis.

5.5.1 Experimental procedure

In order to unmistakably see the change of the MFM probe's magnetization in the MFM image a test structure was chosen that would not change its magnetic configuration in an external field parallel to the sample plane. An array of Co/CoO nanodots (Fig. 5.10 a) that was originally prepared for investigations of exchange-biased structures[110] was used.* The nanodots were prepared by electron beam lithography and a standard lift-off process on silicon substrates. A 25 nm thick Co layer was deposited and subsequently exposed to pure oxygen to form the 2 nm surface oxide. A further oxidation was prevented by coating the sample with a 7 nm Au film. The measurements were performed at room temperature, so the dots behave like small bar magnets. They have a size of 360 nm × 120 nm leading to a magnetic shape anisotropy and a preferred direction of magnetization along the long dot axis, here denoted as x (see Fig. 5.10 c).

The MFM measurements were performed in the Nanoscan hrMFM in high vacuum. For magnetic field dependent studies, the system is equipped with a perpendicular and an in-plane field option. The in-plane magnetic field is provided by an arrangement of four permanent magnets positioned around the sample, its orientation coincides with the sample's x direction. A piezo motor changes the magnets' position to vary the field strength continuously from -230 to +230 mT. The sample was scanned in constant

---

[*] The structure was fabricated by Dominique Givord, Institut Néel, CNRS-UJF, Grenoble, France and provided by Ulrike Wolff, Institute for Metallic Materials, IFW Dresden.

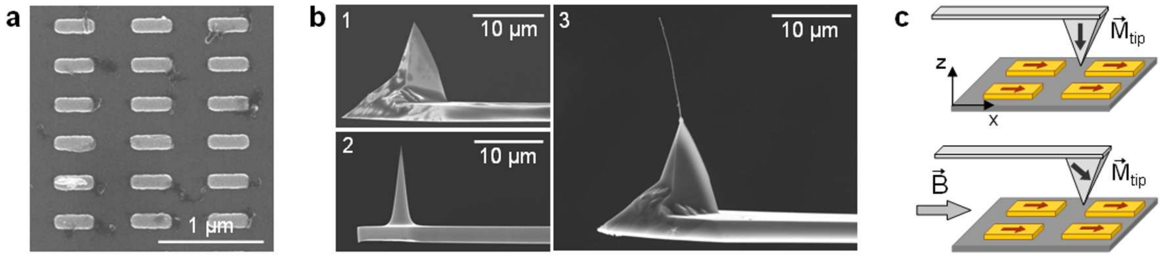

Figure 5.10: a) SEM micrograph of an array of Co/CoO nanodots. b) MFM probes used in this investigation. 1 - Pyramid shaped silicon probe coated with 40 nm CoCrTa. 2 - High aspect ratio MFM probe (HR-MFM, Team Nanotec). 3 - FeCNT MFM probe. c) Schematic view of the MFM measurements. The external field is applied along the long axis of the dots coinciding with x. Bottom: With increasing magnitude of the field, the magnetization of the MFM probe can tilt away from its original orientation along z. This leads to changes in the measured MFM image.

height mode thereby mapping the cantilever frequency shift due to the samples' stray field gradient.

Three different MFM probes were investigated (Fig. 5.10 b): (1) a conventional pyramidal atomic force microscopy (AFM) tapping mode cantilever coated with 40 nm of a high coercive CoCrTa alloy, (2) a coated high aspect ratio MFM probe (HR-MFM, Team Nanotec) and (3) a FeCNT MFM probe. This particular FeCNT contains a 13 μm long and ~30 nm wide iron nanowire. Before the measurement, all MFM probes were magnetized perpendicular to the sample surface, along z. Thus, during MFM measurements the external magnetic field was applied parallel to the sample plane and perpendicular to the original probe magnetization.

5.5.2 In-plane field MFM measurement results

Fig. 5.11 shows MFM scans of the Co/CoO nanodots taken at different values of the external magnetic field with a) the pyramidal MFM probe, b) the high aspect ratio MFM probe and c) the FeCNT MFM probe.[111] When the MFM probe is magnetized along the z direction perpendicular to the sample surface, it only images the z component of the magnetic stray field gradient (we disregard the tilt of the cantilever beam relative to the sample plane). Thus, the zero field MFM scans on the left side of Fig. 5.11 show the magnetic stray field emanating from the ends of the rectangles as black or white dots corresponding to the stray field's z component parallel or antiparallel to the MFM probe magnetization. At a certain value of the external field the black and white dots start to transform into neighboring black-white and white-black structures. At that point the MFM probe magnetization is starting to tilt away from the z-axis into the direction of the applied field (see sketch in Fig. 5.10 c). Consequently, not the

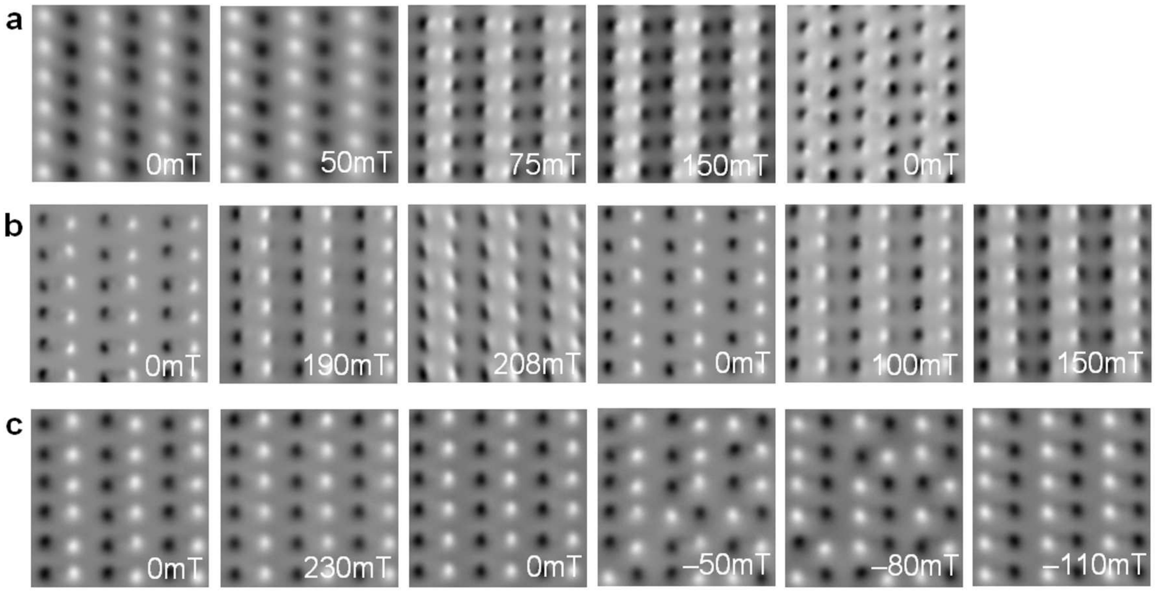

Figure 5.11: MFM scans of the Co/CoO nanodots taken at the displayed values of the external magnetic field with a) the pyramidal MFM probe, b) the high aspect ratio MFM probe and c) the FeCNT MFM probe. Scan size 2.1 μm×2.1 μm.

sample stray field derivatives along the z direction are imaged but those of the stray field component parallel to the direction of the effective tip magnetization.

The three tested probes show different behavior in the external magnetic field. The magnetization of the pyramidal tip (Fig. 5.11 a) starts to follow the external field beginning at a value between 50 and 75 mT. At 150 mT the MFM image seems to display only in-plane field contrast. In the rightmost image of Fig. 5.11 a it can be seen that the probe moment stays tilted even when the external field is removed. In order to restore its magnetization perpendicular to the sample surface, the probe needs to be remagnetized. Especially for MFM measurements conducted in vacuum this represents a bothersome additional effort. The field-dependent behavior of pyramidal MFM probes has already been studied extensively.[109,112–114] Depending on the anisotropy of the coating, the tip magnetization starts to tilt at lower or higher field values. The tilt of the tip's magnetic moment as a function of the external in-plane field was measured by Weis et al.[109] Tilt angles of 40-50° relative to the pyramid axis were found for Co coated probes in a field of ∼8mT. The CoCrTa coated probe has a higher coercivity and its magnetization should thus remain stable up to somewhat higher field values which corresponds to the shown observations.

Weis et al. also found a strong magnetic history dependence of the tip moment of coated probes. This effect was also seen in this study for both coated probes and will be displayed here in detail for the high aspect ratio probe (Fig. 5.11 b). In the first experimental run after having magnetized the probe along z, the tilt of the probe magnetization is only observed at a field of ~200 mT, probably due to the higher shape anisotropy of the probe. With the field removed, the in-plane component of the tip magnetization is not visible anymore in the MFM image. In the second run of increasing the external field, the tip moment starts tilting already at ~100 mT. This could indicate that the probe magnetization was not completely restored to the original state after the first run. A slightly modified domain configuration might have remained lowering the energy barrier for the rotation of the tip moment in the second run.

Fig. 5.11 c shows the field dependent measurements performed with the FeCNT MFM probe. The in-plane field was increased up to the experimental limit of 230 mT without a sign of a tilting tip magnetization. Due to the high shape anisotropy the probe magnetization remains stable along the FeCNT axis and the unchanged z component of the magnetic sample stray field gradient is imaged. Then the field was reduced to 0 mT and stepwise increased in the opposite direction to observe the switching of the nanodots. The dots switch at different fields ranging from ~40 mT to ~100 mT.[110] This switching process can be nicely observed with the FeCNT probe without a disturbing in-plane magnetization. The FeCNT probe thus allows an easily interpretable observation of magnetic reversal processes in the presence of an external field of at least up to 230 mT perpendicular to the FeCNT axis.

5.5.3 Micromagnetic simulation of an iron nanowire in external fields

It is known that if the direction of an external magnetic field deviates from the long axis of a ferromagnetic nanowire, the magnetic moments inside the nanowire start to tilt towards the applied field (e.g. shown experimentally by Wang et al.[115]). When the applied field becomes stronger, the deviation of the moment's orientation from the nanowire axis also becomes larger. Yet in this work, the MFM measurements in applied fields do not show a component of the FeCNT's magnetization parallel to the sample surface. This could mean that the deviation of the magnetization from the wire axis is still small and the stray field of the magnetic monopole at the nanowire end outweighs the existing in-plane components.

To better understand the FeCNT probe's behavior, micromagnetic simulations of the reversal process of an iron nanowire were performed with the *NMag* simulation code. Detailed information on *NMag* can be found elsewhere.[116,117] The simulations are based on the Landau-Lifshitz-Gilbert equation[118,119] describing the dynamic magnetization processes in a ferromagnetic material:

$$\frac{\partial \mathbf{M}}{\partial t} = -\gamma \, \mathbf{M} \times \mathbf{H}_T + \frac{\alpha}{M_s} \mathbf{M} \times \frac{\partial \mathbf{M}}{\partial t} \tag{5.3}$$

where $\mu_0 \, \mathbf{H}_T = -\frac{\partial E}{\partial \mathbf{M}}$ is the total effective magnetic field, E is the total free energy in the ferromagnet, M_s is the saturation magnetization, γ is the gyromagnetic ratio and α is the Gilbert damping constant. The total effective magnetic field can for example be described as $H_T = H + H_k + H_D + H_{ex}$ with the applied field H, the magnetocrystalline anisotropy field H_k, the demagnetization field H_D and the exchange field H_{ex}.[42,120] For a constant $\mathbf{H}_T$ and $\alpha = 0$, M precesses around the field vector $\mathbf{H}_T$ with a frequency $\omega = \gamma \mu_0 H_T$. The damping leads to a relaxation (the precession spirals down) towards a time independent magnetization along the field direction on a time scale of $1/\alpha\omega$.

The *NMag* simulation code takes a given magnetization configuration and carries out the time integration of Eq. 5.3 until the system reaches a (metastable) equilibrium. This is the case when the torque on the magnetic moment at each site of the simulated object's mesh is smaller than a certain threshold.[116]

It has been shown (e.g., by Ott et al.[121]) that the approximated shape of the nanowire has a big influence on the simulation results. The hysteresis curves of cylindrical, ellipsoidal or bar-shaped wires of the same dimensions can differ considerably. To come as close as possible to the real geometry of the nanowires used in this work, TEM images of the wire ends were made (Fig. 5.12 c). As the wire end is not flat, the nanowire's geometry was approximated by a cylinder with hemispherical caps (Fig. 5.12 a). The length of the simulated cylinder was set to 200 nm and its width to 10 nm leading to an aspect ratio of 20:1. The actual probe aspect ratio is bigger than that (approx. 400:1). The calculation should nevertheless be valid for our case since it has been shown that the shape anisotropy of magnetic nanowires changes gradually with increasing aspect ratio, but then remains almost constant when the aspect ratio gets larger than 20:1 (see section 2.3).[46]

The orientation of the iron nanowire on the measured FeCNT probe is not exactly perpendicular to the sample surface and the external field. From SEM images taken at various stage tilt angles the nanowire's angle with respect to z was estimated to be ∼19°. Taking this into account, the wire's hysteresis curve was simulated using a geometrically equivalent arrangement with a magnetic field applied along x and the nanowire oriented in the $x - z$ plane (Fig. 5.12 a and b).

The red curve with circular symbols displays the magnetization parallel to the long nanowire axis ($M_{\parallel}$, easy axis), the blue curve with square symbols represents the magnetization component in the $x - z$ plane perpendicular to the long axis ($M_{\perp}$, hard

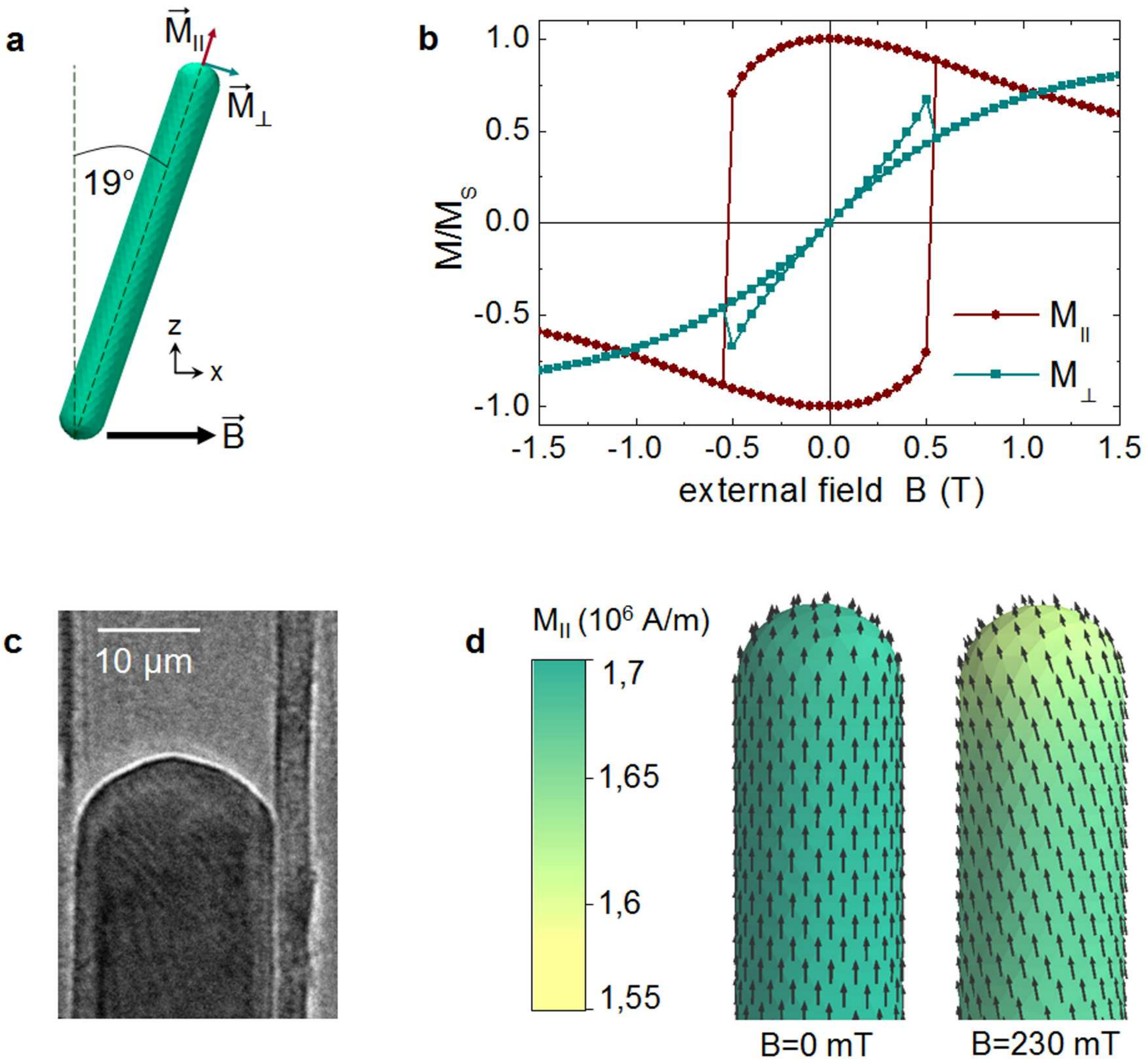

Figure 5.12: Micromagnetic simulation of the hysteresis curve of a FeCNT probe. a) Capped cylinder used for the simulation in the geometry of the experimental setup. b) Hysteresis curve of a capped iron cylinder simulated with *NMag*. The red curve with circular symbols displays the magnetization component $M_{\parallel}$ parallel to the long nanowire axis, the blue curve with square symbols represents the magnetization component $M_{\perp}$ perpendicular to the long axis. c) TEM image of the end of an iron nanowire enclosed in a CNT. d) Magnetic configuration of the simulated nanowire at different points of the hysteresis curve. Left: zero field. Right: 230 mT, the maximum applied field in the MFM experiments. The black arrows show the direction of the magnetization **M**. The colored surface represents the magnitude of $M_{\parallel}$.

axis). It can be seen that the wire magnetization component parallel to the long axis at first decays very slowly with increasing field. At the maximum experimental value of 230 mT a small perpendicular magnetization component already appeared, but the parallel component is still more than four times larger. This can also be seen in the visualization of the magnetization vector field (Fig. 5.12 d). At 230 mT the largest deviation of the magnetization can be seen at the wire end, but the magnitude of $M_{\|}$ still amounts to more than 90% of its zero field value. When the applied field is increased further, the wire magnetization tilts more and more towards the external field. In a magnetic field >1.1 T the component perpendicular to the wire axis dominates. The sudden jumps in the curve at ±0.5 T mark the reversal of the wire magnetization. This corresponds well to what has been found in MFM measurements of the angular dependence of the switching field of iron nanowires.[115]

The Fe crystal orientation of the FeCNT probe was not considered in this calculation. However, as the iron nanowire's magnetocrystalline anisotropy (K_u =0.046 MJ/m^3) is more than one order of magnitude smaller than its shape anisotropy ($\mu_0 M_s^2/4$ $= 0.9$ MJ/m^3 for an infinite cylinder) it may be neglected in this case.

6 Calibration of FeCNT probes for quantitative MFM

A single magnetic domain iron wire enclosed in a carbon nanotube with a high shape anisotropy constitutes a structure of predictable magnetic properties that can simplify the reconstruction of MFM data. The ferromagnetic wire can be treated as an extended dipole of which only the monopole close to the sample surface is involved in the imaging process. In this section, a calibration routine based on the point probe model (described in section 3.3.3.2) will be presented. This routine can be used to determine the probe's magnetic monopole moment and prove its independence of the sample stray field geometry. This opens up the potential for straightforward quantitative MFM measurements.

6.1 Calibration device

6.1.1 Device design

For the calibration of a FeCNT MFM probe, the effective probe monopole moment involved in the imaging process, its position in the probe according to the point probe model and the dependence of both values on the decay length of the sample stray field need to be determined.[71] To achieve this, a calibration structure which generates a well defined local magnetic field at small length scales is necessary. In addition, different magnetic field geometries need to be accessible to test their influence on the probe's effective magnetic moment. For this purpose current carrying parallel nanowires as suggested by Kebe and Carl for the calibration of coated MFM probes are used.[18,69]

Fig. 6.1 a shows a schematic drawing of a section of parallel lines carrying current I with the definition of the lateral dimensions and the coordinate system in use. The

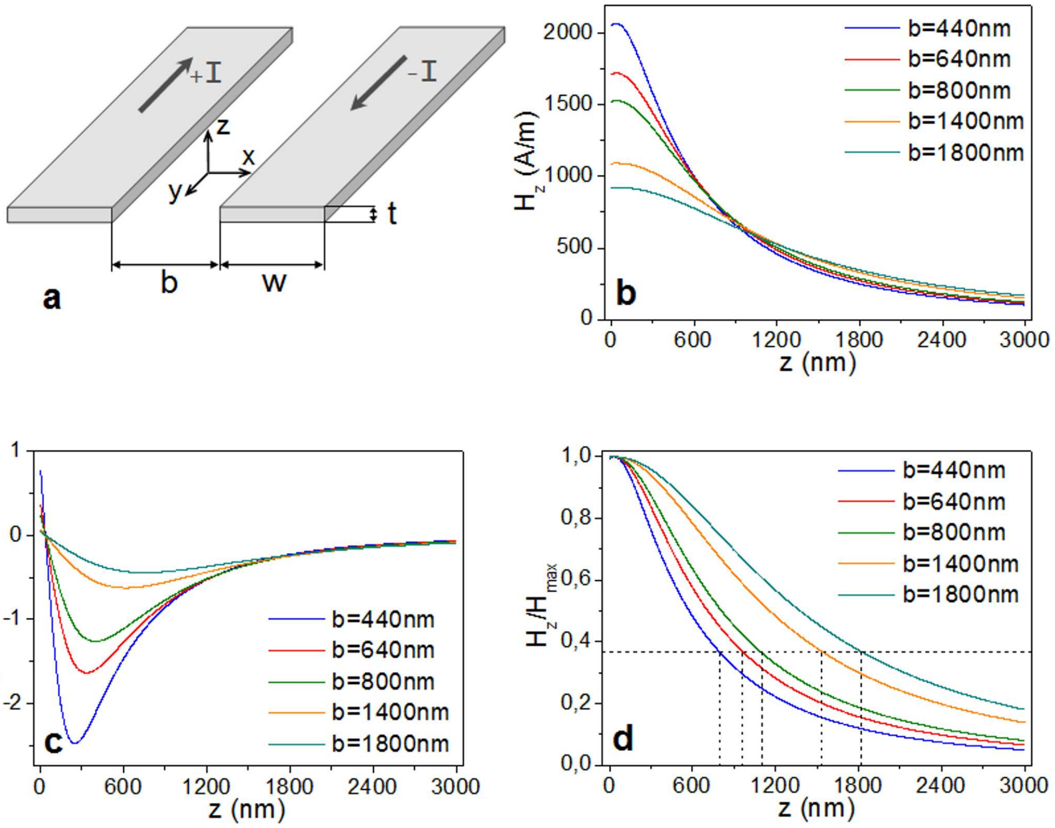

Figure 6.1: a) Schematic drawing of a parallel wire section with the definition of the lateral dimensions and the coordinate system in use. b) z-component of the magnetic field H_z in the center between the lines ($x = 0$) as a function of z according to Eq. 6.3 for a current of $I = 4\,\text{mA}$. The different colors represent different wire separations b. c) Corresponding plot of the first derivative of H_z with respect to z (Eq. 6.4). d) H_z/H_{max} as a function of z. The dotted lines mark the positions where the magnetic field has dropped to a value $H(z = \lambda) = H_{max}/e$ (37% of H_{max}). The so defined decay length λ of H_z in the z direction increases with larger distances b between the wires.

magnetic field caused by such an infinitely extended (along y) line can be calculated with the Biot-Savart law:

$$\mathbf{H}(\mathbf{r}) = \frac{1}{4\pi} \int_0^w dx' \int_{-\infty}^{\infty} dy' \int_0^t \frac{\mathbf{j}(\mathbf{r}) \times (\mathbf{r} - \mathbf{r}')}{|\mathbf{r} - \mathbf{r}'|^3} dz' \tag{6.1}$$

Here w is the line width, t its thickness and $|\mathbf{j}| = I/wt$ is the current density. The resulting magnetic field only has components along x and z and depends on the line's geometry and the applied current:

$$\mathbf{H}(\mathbf{r}) = H_x(I, w, t, x, z)\mathbf{e}_x + H_z(I, w, t, x, z)\mathbf{e}_z \tag{6.2}$$

The exact result derived from Eq. 6.1 can be found elsewhere.[18,69] The magnetic field produced by the setup shown in Fig. 6.1 a is obtained by the superposition of the fields obtained by each one of the two lines with the parameter b as their separation along x. Due to the current line symmetry, the magnetic field component along x vanishes in their exact center ($x = 0$) in all heights z. The remaining z component can be calculated as a function of the height z above the sample surface:[18]

$$\begin{aligned} H_z = \frac{I}{2\pi wt} \Bigg\{ &(z-t)\; ln \left[\frac{(z-t)^2 + (b/2)^2}{(z-t)^2 + [w+(b/2)]^2} \right] - z\, ln \left[\frac{z^2 + (b/2)^2}{z^2 + [w+(b/2)]^2} \right] \\ &- 2\,[w+(b/2)] \cdot \left[arctan\left(\frac{z-t}{w+(b/2)} \right) - arctan\left(\frac{z}{w+(b/2)} \right) \right] \\ &+ b \left[arctan\left(\frac{z-t}{b/2} \right) - arctan\left(\frac{z}{b/2} \right) \right] \Bigg\} \end{aligned} \tag{6.3}$$

The first derivative of H_z with respect to z, $dH_z/dz(\mathrm{A/m^2})$, which is needed for the point monopole model is then given by

$$\begin{aligned} \frac{dH_z}{dz} = \frac{I}{2\pi wt} \Bigg\{ &\frac{2b^2}{b^2 + 4(z-t)^2} - \frac{2b^2}{b^2 + 4z^2} + \frac{2(2w+b)^2}{(2w+b)^2 + 4z^2} \\ &- \frac{2(2w+b)^2}{(2w+b)^2 + 4(z-t)^2} - ln \left[\frac{(z-t)^2 + (b/2)^2}{(z-t)^2 + (w+b/2)^2} \right] \\ &+ ln \left[\frac{z^2 + (b/2)^2}{z^2 + (w+b/2)^2} \right] + \frac{2(z-t)^2 \left[(w+b/2)^2 - (b/2)^2 \right]}{\left[(z-t)^2 + (b/2)^2 \right] \left[(z-t)^2 + (w+b/2)^2 \right]} \\ &- \frac{2z^2 \left[(w+b/2)^2 - (b/2)^2 \right]}{\left[z^2 + (b/2)^2 \right] \left[z^2 + (w+b/2)^2 \right]} \Bigg\} \end{aligned} \tag{6.4}$$

The spatial distribution of the generated magnetic field and its gradient can be altered by varying the distance b between the parallel lines. Fig. 6.1 b- d show the stray field's z component at $x = 0$, its first derivative and the corresponding decay length as a function of z for various values of b calculated with Eq. 6.3 and 6.4. The decay length λ is here defined as the distance z where the magnetic field has dropped to a value of $H(z = \lambda) = H_{max}/e$, so about 37% of H_{max}. Although H_z does not decrease exponentially with z, this definition is still useful. In Fig. 6.1 d, b varies from 440 to 1800 nm and the corresponding decay lengths vary from about 800 to 1800 nm. Smaller separations b lead to a larger absolute value of H_z close to the sample surface but also to a faster decrease along z. Consequently, the magnetic field generated by parallel wires with a larger separation b has a larger decay length and extends further in the

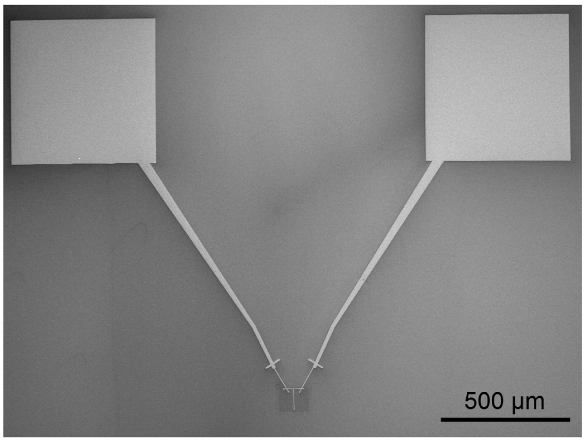

Figure 6.2: SEM micrograph of contact pads and parallel gold lines produced by EBL. A more detailed view of the parallel lines is shown in Fig. 6.3.

z direction. This enables us to probe the dependence of the tip's effective monopole moment on the stray field geometry.

6.1.2 Device fabrication by electron beam lithography

The parallel line structures and contact pads were fabricated by standard electron beam lithography (EBL) and lift-off technique on silicon substrates.[*] At first, two layers of the electron resist poly(methyl methacrylate) (PMMA) were spin-coated onto a 7 mm×7 mm silicon wafer with 300 nm surface oxide. For each layer, the polymer solution was dropped onto the wafer at a spinning rate of 2000 rpm and then distributed evenly on the surface at 6000 rpm for 30 s. For the 200 nm thick bottom layer, PMMA with an average molecular weight of 50 K was used and diluted with chlorobenzene to a 9 weight percent solution. The 50 nm top layer was prepared with a 1 weight percent solution of 950 K PMMA. After spin-coating, each layer was heated for 10 min on a hot plate at 150 °C to avoid any strains inside the PMMA layers and to evaporate the solvent chlorobenzene. The two different PMMA layers react differently to a given electron exposure and thus provide an undercut of the structures which facilitates the lift-off procedure.

The lithography was carried out in a FEI Nova$^{\text{TM}}$ NanoSEM equipped with a nanonic eLitho lithography system. The smallest areas of the line structures were exposed with a beam current of 20 pA at 25 kV while the larger contact pads were fabricated with a current of 2000 pA (Fig. 6.2). After exposure, the electron resist was developed for 2.5 min in a 1:3 volume ratio mixture of methyl isobutyl ketone and isopropanol (MIBK:IPO). The development process was then stopped by a 1 min bath in isopropanol.

---

[*] The structure fabrication was performed in collaboration with Kamil Lipert, Institute for Solid State Research, IFW Dresden and Joachim Schumann, Institute for Integrative Nanosciences, IFW Dresden.

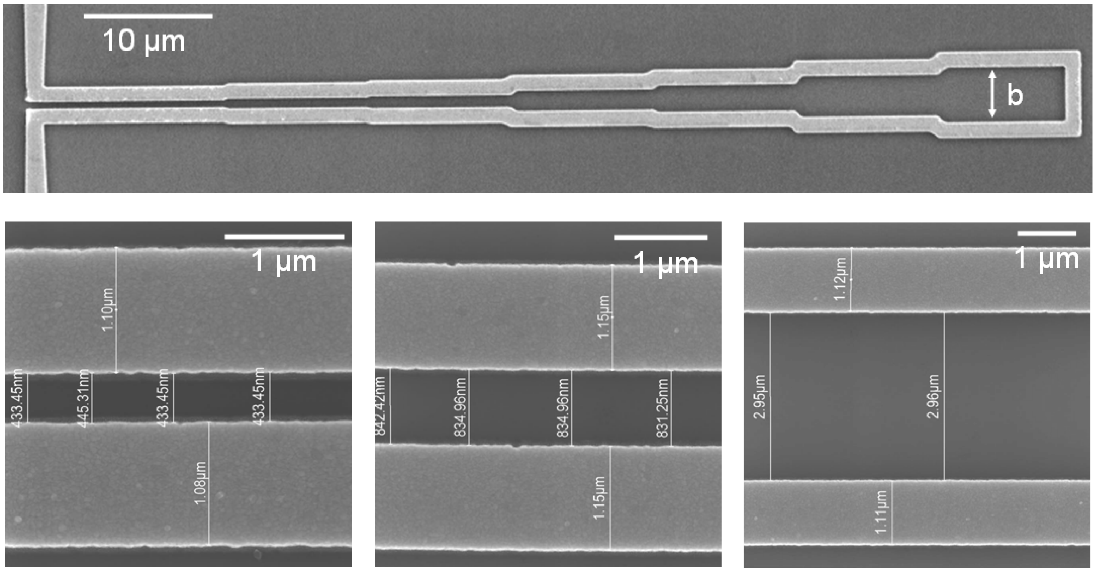

Figure 6.3: SEM images of parallel gold lines produced by EBL. Top: The entire structure with varying distance b between the lines. Bottom: Higher magnification micrographs of parallel lines with b = 440 nm, 830 nm and 3 µm.

Subsequently, the sample was coated with a 70 nm gold layer via conventional thermal evaporation including the deposition of a 5 nm Cr adhesion layer. The lift-off was performed in an acetone bath at 70 °C.

Fig. 6.3 shows SEM micrographs of the resulting sample. As mentioned above, the line distance b is changed along the length of the structure to produce magnetic fields of varying decay lengths. However, b is kept constant for wire segments of 10µm length each to have a sufficiently large region of uniform geometry for the measurement and to avoid disturbing fields from the curved line sections.

In EBL, the so-called proximity-effect causes the exposure distribution and hence the developed pattern to be wider than the scanned pattern. Electrons that penetrate the resist can scatter back off the silicon substrate and cause subsequent exposing processes. Consequently, the final pattern size deviates slightly from the predefined size. To determine the exact dimensions of the fabricated lines, SEM (Fig. 6.3) and AFM (Fig. 6.4) measurements were performed. The measured line width differs from the nominal w=1 µm by 50 - 150 nm depending on the line separation. This leads to corresponding changes of the actual distance between the lines. The line thickness t=72 nm is constant throughout the structure within the gold layer's surface roughness. For wider line separations (b >800 nm) the roughness is smaller than 2 nm and it increases slightly to approximately 3.5 nm for closer line segments (440 nm< b <650 nm). For the determination of the magnetic field generated by the sample the measured dimensions are used.

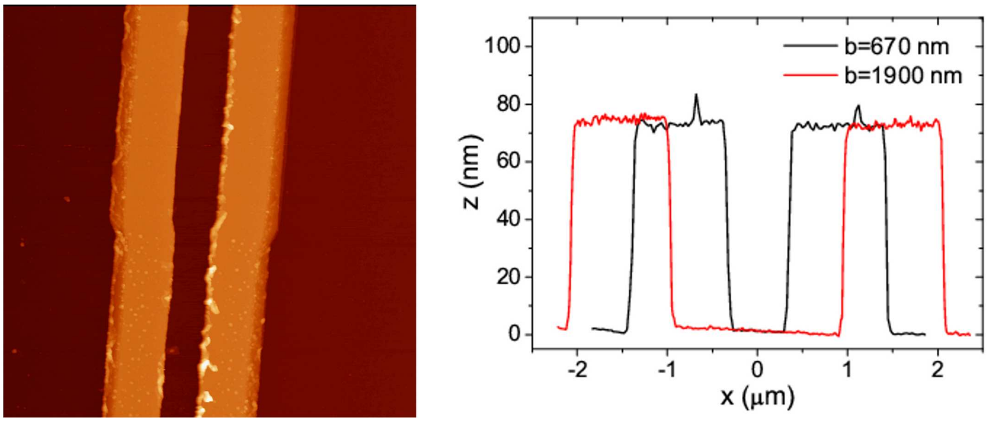

Figure 6.4: AFM images of parallel gold lines produced by EBL. Left: 8 µm×8 µm height image. Right: Sections at two different line distances b.

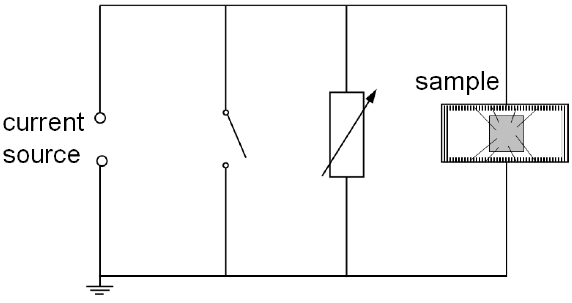

Figure 6.5: Electrical circuit to protect the gold lines from electrostatic potentials. The current source, a switch and a potentiometer (0 - 100 kΩ) are connected parallel to the sample.

6.1.3 Current voltage characteristic of the parallel gold line structures

One silicon sample contains four parallel line structures along with the connected contact pads. After measuring all necessary properties in the AFM, the sample was placed onto a 24 lead chip carrier. Each contact pad was connected to one of the leads via ultrasonic wedge bonding of aluminum wires. The connected gold line structures are very sensitive to electrostatic potentials. The resulting currents might lead to an evaporation of the metal. To avoid destructive potentials when connecting the sample to the current source, an electric circuit containing a switch and a potentiometer is interconnected (Fig. 6.5). When the sample is connected to the source, the switch is closed. The potentiometer is set to the lowest resistance to protect the sample from current pulses that might be created when opening the switch. Finally the potentiometer is set to the highest resistance (100 kΩ). Then the current will flow through the gold lines which have a much lower resistance (≈350 Ω). As current source, a Keithley SourceMeter 2400 for coupled sourcing and measurement was used.

The small cross section of the parallel gold wires can lead to high current densities even at low dc-currents. A current I =10 mA passing through a wire with thickness t=70 nm and width w=1 µm leads to a current density $j = I/wt = 1.4 \cdot 10^{11}$ A/m^2.

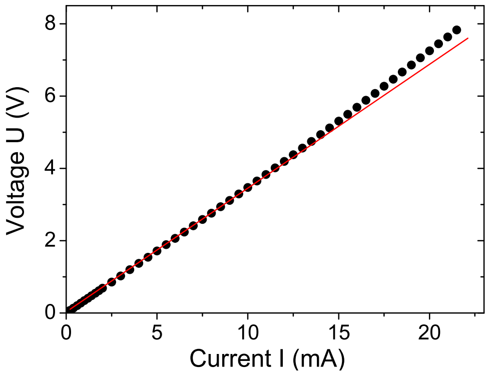

Figure 6.6: Typical current-voltage curve for a parallel gold line sample showing a linear slope up to a current of ≈9 mA. For higher currents, the resistance of the wires increases leading to a steeper slope.

This can lead to a substantial increase of the sample's temperature and resistance. To determine the constant resistance regime and the break-down current of the gold lines, the current (I) - voltage (U) characteristic was measured (Fig. 6.6). Varying slightly from one structure to another, the $I - U$ curve of the device is linear up to a current of 7 - 9 mA. In Fig. 6.6, for I <7 mA the resistance measures 342 Ω, at I=12 mA it has a value of 350 Ω.

The gold wire's temperature T can be calculated from its resistance R by using the relation[18]

$$R(T) = R_{T=293\,K}\left[1 + \alpha(T - 20\,K)\right] \tag{6.5}$$

with the temperature coefficient of the electrical resistance for gold α=4·10^{-3}K^{-1}. From zero current to 12 mA, the line temperature increases by 6 K. This small increase should not effect the MFM measurements and indicates a good thermal contact between the gold lines and the silicon substrate. At 15 mA the temperature increase already amounts to 10 K. For higher currents, the temperature increases faster until a local melting of the line occurs. Most structures were found to break down at values of 25 ± 5 mA. With optical microscopy it was observed that the structures tend to be destroyed at the thinnest cross section carrying the highest current density. If the lines contain defects, the failure can also happen at those sites.

The calibration measurements were performed at a current of 4 mA to avoid any heating and increasing resistance. Thus we can exclude a temperature change in the vicinity of the MFM tip during the calibration procedure.

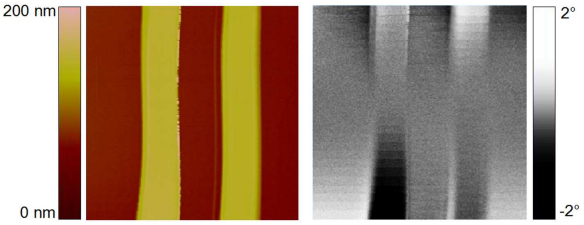

Figure 6.7: Topography image (left) and MFM scan (right, phase shift) of two parallel lines (slow scan axis disabled, a slight non-constant drift along x is visible). The current was swept from -12 to +12 mA during the scan. Scan range: 8×8 μm

6.2 INFLUENCE OF ELECTROSTATIC FORCES ON THE MEASURED PHASE SHIFT SIGNAL

For a quantitative evaluation of MFM data it is of great importance to consider all possible influences on the measured signal. As mentioned in section 3.3, there are several forces acting on the MFM probe, e.g. Van der Waals forces, electrostatic forces and magnetic forces. The calibration is mostly carried out at a distance >100 nm from the sample surface, so the Van der Waals forces are negligible. However, long range electrostatic forces need to be taken into account, especially since the gold lines and the substrate surface have a different contact potential and the lines are each connected to different potentials of the current source. Thus it is not possible to cancel this interaction by controlling the bias between the tip and the sample as it is done in the case of a flat single material sample.

It was observed in first calibration experiments that the cantilever phase shift cannot be purely due to magnetic interactions. The dependence of the phase shift on the current of the parallel lines did not show a linear behavior as expected from the linear relation between dH_z/dz and the applied current I in the Biot-Savart law (Eq. 6.1). The electrostatic influence can also be seen in Fig. 6.7. A topography image (left) and an MFM scan (right) of two parallel lines are displayed (measured in lift mode in a Digital Instruments 3100 SPM). During the scan, the current was swept from -12 to +12 mA. The increasing white and dark contrast indicates the increasing electrostatic interaction between the probe (kept at constant potential) and the changing line potential. Especially for small distances between the lines, this interaction can still be visible in the center between the lines.

This problem was not encountered by other groups who carried out the calibration of conventional probes (e.g. Kebe et al.[18] or Lohau et al.[17]). A possible reason could be that the magnetic moment of the FeCNT probe is smaller compared to that of magnetically coated probes and the magnetic interaction does not necessarily outweigh the electrostatic influences. As an example, Kebe et al.[18] measured monopole moments ranging from 1 to $6 \cdot 10^{-8}$ Am for coated MFM probes. The monopole moment of FeCNT probes is more than one order of magnitude smaller as will be shown later.

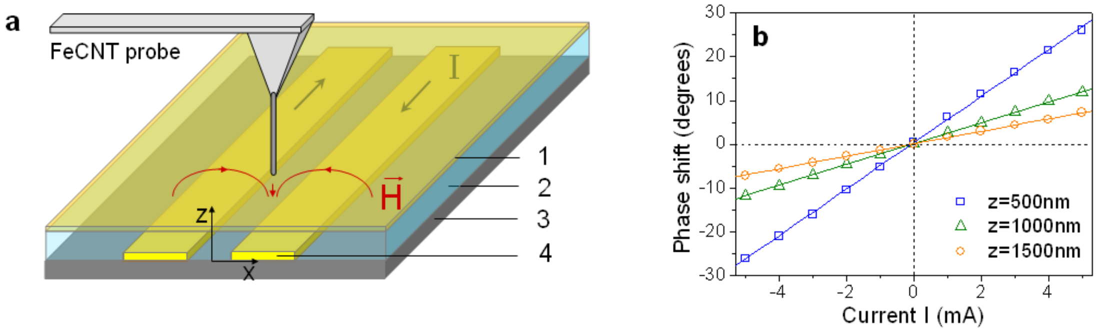

Figure 6.8: a) A gold layer on top of the gold lines shields electrostatic interactions. 1) 70 nm gold layer to shield electrostatic potentials. 2) 200 nm silicon nitride insulation layer. 3) Silicon substrate. 4) 70 nm thick and 1 μm wide parallel gold lines carrying opposing current $\pm I$. b) Phase shift in the center between the lines ($x = 0$) depending on the current of the calibration structure for three different heights z, b=620 nm.

However, some groups solved the problem by constantly adjusting the tip potential to that of the sample (potential-correction MFM)[122] or by physically grounding a segment of the current lines to the tip.[123] In this work, the electrostatic interaction was shielded by depositing a 200 nm silicon nitride insulation layer by radio frequency magnetron sputtering and a 60 nm gold layer on top of the current lines to shield the electrostatic interaction (Fig. 6.8 a). During both processes, the contact pads were protected by a layer of photoresist that was manually applied with a small brush. After deposition, a lift-off procedure was performed to uncover the contact pads.

After setting the tip to the constant potential of the gold layer, only magnetic interactions should be detected. To test this, the phase shift $\Delta\Phi$ of the cantilever oscillation in the center between the lines was detected depending on the current I passing through the lines. This measurement was carried out at three constant heights, z=500 nm, z=1000 nm and z=1500 nm (Fig. 6.8 b). We observe $\Delta\Phi$=0 at zero current, thus we have no remaining signal from interactions other than magnetic. At the transition from negative to positive current the sign of $\Delta\Phi$ changes due to the reversal of the magnetic field produced by the current lines. The linear relation between I and $\Delta\Phi$ proves that there is no modification of the measured signal by the electrostatic forces originating from the current carrying lines. It also implies that the tip magnetization is not changed by the small magnetic stray field of the lines which at I=4 mA has a maximum value of H_z=2000 A/m corresponding to less than 3 mT (Fig. 6.1 b). This is no surprise given the high stability of FeCNT probes in much higher external fields described in section 5.5.

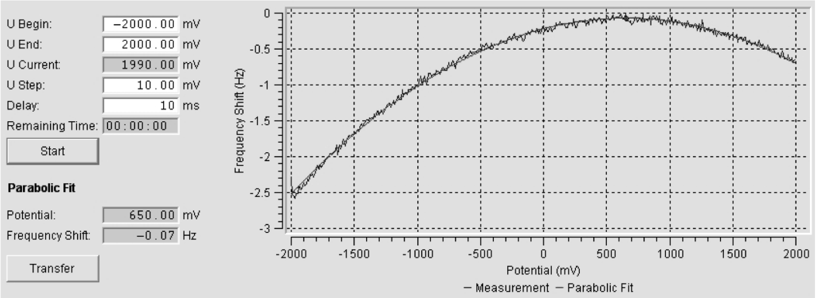

U Begin: −2000.00 mV
U End: 2000.00 mV
U Current: 1990.00 mV
U Step: 10.00 mV
Delay: 10 ms
Remaining Time: 00:00:00

Parabolic Fit

Potential: 650.00 mV
Frequency Shift: −0.07 Hz

Figure 6.9: Bias sweep to determine the sample surface potential.

6.3 Calibration of a conventional MFM probe

The calibration routine that is described here is adapted from the works of Kebe et al.[18,69] with an additional adjustment of the electrostatic potentials. The calibration measurements were conducted in the Nanoscan hr-MFM in high vacuum. The calibration structure was placed on the sample holder plate and connected via an electric feed-through to a Keithley SourceMeter 2400. The gold shielding layer of the structure was connected to the grounded output of the current source. The MFM probe itself is connected to a floating potential within the MFM, so probe and sample are not on the same potential. This difference was adjusted during the measurement as will be explained later. After probe and sample have been installed, the microscope chamber was pumped to approximately $1{\cdot}10^{-6}$ mbar. The parallel line structure was prepositioned with the help of the external CCD cameras and the MFM probe set to oscillate at its resonance frequency. A current of $\mathrm{I} = 4\,\mathrm{mA}$ was then applied to the structure at least 1 hour before the actual measurement and kept constant throughout. This ensures a constant sample temperature and minimizes drifts due to thermal expansion.

To adjust the probe potential to the sample potential, a bias sweep was performed. For this, the potential applied to the probe is swept from, e.g, -2 V to +2 V while the frequency shift signal (and thus the electrostatic interaction between probe and sample) is recorded. Fig. 6.9 shows such a sweep. The maximum of the parabola (minimum probe-sample interaction) marks the surface potential. Due to the shielding layer, this potential does not depend on the current applied to the lines or the $x - y$ position of the probe, however, it does depend slightly on the probe's height z above the sample surface. Therefore, the bias sweep is repeated in different heights. The respective potential is then applied to the probe during the measurement in different heights.

For the probe calibration the phase shift signal $\Delta\Phi$ in the center (x=0) between the current carrying lines needs to be detected. To accurately locate the center, line

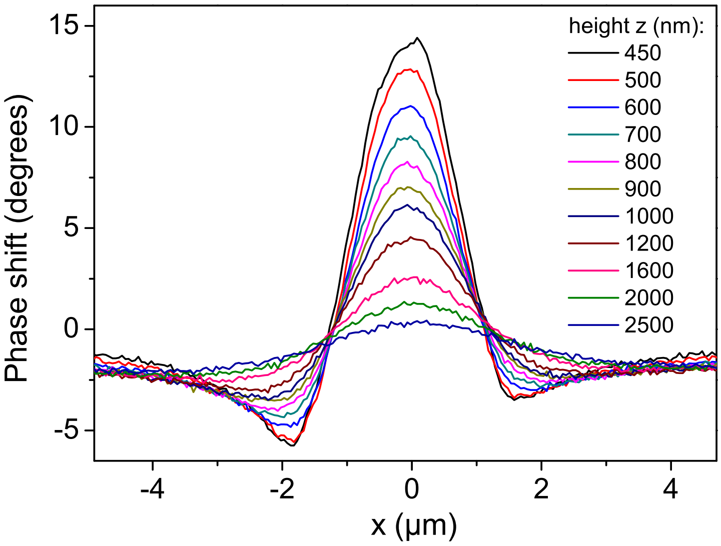

Figure 6.10: Line scans at different heights above the sample surface across two current carrying lines with b=630 nm. The phase shift signal at x=0 nm is evaluated in the calibration process.

scans over the line structures are performed, but only the signal at $x=0$ is evaluated (Fig. 6.10). These scans are repeated in different heights z to obtain a phase shift $\Delta\Phi$ vs. height z curve that can be fitted using the point monopole model. Consequently, the resulting probe moment is a mean value over different probe heights.

Within the point probe approximation (see section 3.3.3.2), the phase shift $\Delta\Phi$ of the cantilever vibration (MFM signal) due to the effective probe monopole moment and the sample's magnetic field gradient at $x=0$ can be expressed as[17,18]

$$\Delta\Phi = \mu_0 \frac{180}{\pi} \frac{Q}{k} q \frac{\partial H_z}{\partial z} \tag{6.6}$$

The only unknown in this equation is the tip's monopole moment, q, which will be obtained by fitting the measured phase shift $\Delta\Phi$ at $x=0$ depending on z to Eq. 6.6. In addition, in the expression for $\frac{\partial H_z}{\partial z}$ z will be replaced by $z+d$ where d accounts for the distance of the point monopole from the tip apex. This procedure will be performed for different sample stray field geometries.

The calibration procedure was first tested with a conventional magnetically coated pyramid shaped tip (Nanosensors PPP-MFMR) in order to compare the obtained results to the results of other groups and validate the used setup. Conventional probes might as well be described by a point dipole, however, to compare the results to the ones obtained with a FeCNT probe the point monopole description was chosen.

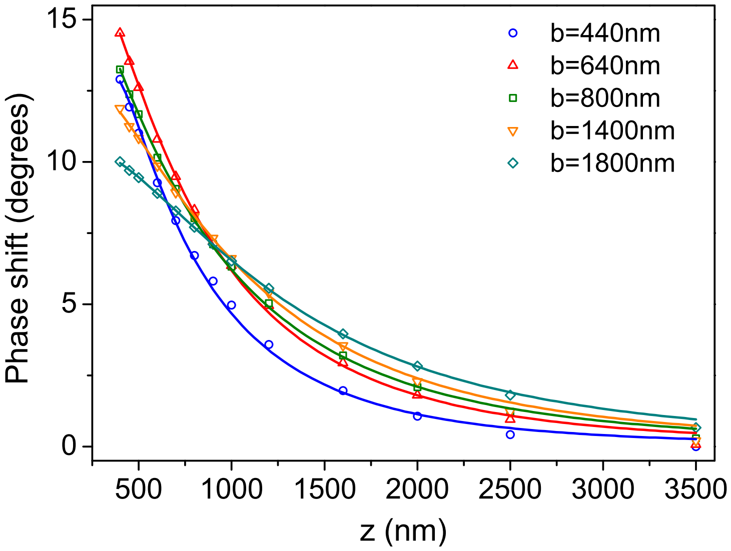

Figure 6.11: Phase shift $\Delta\Phi$ vs. height z curves measured with a coated MFM probe for different line separations b. The symbols represent the measured data, the solid lines are the fitted curves according to the point probe model.

The fit was carried out using the built-in Origin fit procedure based on a Levenberg-Marquardt algorithm for least squares curve fitting. The probe monopole moment q and its position d were fitted. The values for the line geometry (width w, separation b, thickness t) were set according to SEM or AFM measurements. The quality factor Q was determined from the cantilever's resonance curve with $Q = f_0/\Delta f$ where f_0 is the resonance frequency and Δf is the width of the resonance peak at its maximum amplitude divided by $\sqrt{2}$. The spring constant k of the cantilever was calculated based on Eq. 3.2 with the cantilever dimensions determined from SEM images and the density ρ=2.33 g/cm^3 for silicon.

Fig. 6.11 shows the resulting $\Delta\Phi$ vs. z curves for different line separations b. The symbols represent the measured data, the solid lines are the fitted curves using Eq. 6.6. The obtained values for the monopole moment and its position are listed in table 6.1.

The curve shapes in Fig. 6.11 reflect the expected behavior of $\frac{\partial H_z}{\partial z}$ and can be fitted well with the monopole model. The values for the probe's monopole moment and its distance from the probe apex both increase with increasing distance between the line structures (larger stray field decay length). The effective probe moment increases by more than 50% from $4.3 \cdot 10^{-8}$ to $6.5 \cdot 10^{-8}$ Am, its distance d from the tip apex increases from 520 to 830 nm. These findings are in agreement with measurements performed by Kebe et al.[18] which proves that the used calibration structure is working as expected. The results also confirm that a universal calibration for coated pyramidal MFM probes is not possible with this calibration route.

Table 6.1: Fitted monopole moment q and its position d of a coated MFM probe for different current line separations b.

b (nm)	q (A/m)	d (nm)
440	$4.3 \cdot 10^{-8}$	520
640	$4.6 \cdot 10^{-8}$	550
800	$4.9 \cdot 10^{-8}$	610
1400	$5.9 \cdot 10^{-8}$	690
1800	$6.5 \cdot 10^{-8}$	830

The described routine for calibration is very time consuming as the phase shift line scans across the current carrying lines need to be performed at a slow scan rate to minimize errors (< 1µm/min). To improve this, an additional procedure was tested. After obtaining a topography scan of the parallel lines, the probe was positioned at the very center between them (x=0). The phase shift was then read with a PC-based digital oscilloscope (PicoScope) while the probe was moved further away from the sample surface alomg z. If there is no drift in the sample's position, the obtained results do not differ from the ones obtained using the full line scans. All shown calibration results were obtained using the oscilloscope.

6.4 CALIBRATION OF A FECNT MFM PROBE

The calibration was carried out for a probe equipped with a FeCNT containing a 5 μm long iron wire at its end. Fig. 6.12 displays the measured phase shift at x=0 as a function of the distance z from the silicon surface for different values of the current line separation b. The fitted values for the monopole moment q and its position d are shown in table 6.2.

The fitted monopole moment of the FeCNT MFM probe varies between $2.0 \cdot 10^{-9}$ and $2.3 \cdot 10^{-9}$ Am with a mean value of $(2.1 \pm 0.1) \cdot 10^{-9}$ Am. This clearly shows that even with a changing decay length of the sample's magnetic stray field the effective probe moment stays constant.

The fitted monopole position d shows no monotonous behavior, it fluctuates around zero with a standard deviation of 54 nm. A more accurate measurement of d could be achieved by downscaling the calibration structure. Then d should only reflect the thickness of the carbon shell which separates the end of the magnetic nanowire from

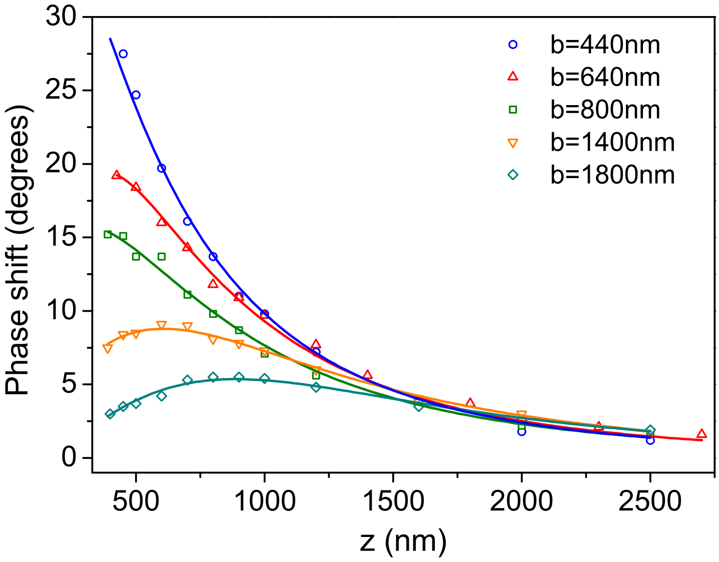

Figure 6.12: Phase shift $\Delta\Phi$ vs. height z curves measured with a FeCNT MFM probe for different line separations b. The symbols represent the measured data, the solid lines are the fitted curves according to the point probe model.

Table 6.2: Fitted monopole moment q and its position d of a FeCNT MFM probe for different current line separations b.

b (nm)	q (A/m)	d (nm)
440	$2.3{\cdot}10^{-9}$	15
640	$2.0{\cdot}10^{-9}$	-59
800	$2.1{\cdot}10^{-9}$	65
1400	$2.3{\cdot}10^{-9}$	7
1800	$2.0{\cdot}10^{-9}$	-63

the sample surface at z=0. However, geometrical deviations from the ideal cylinder geometry at the nanowire end can result in a slight shift of the effective position.

The theoretical monopole moment of the FeCNT probe can be calculated with $m = M_s \cdot \pi r^2$ using the iron nanowire's radius r of approximately 21 nm and the saturation magnetization of iron $M_s(300\,\mathrm{K})$=$1.71 \cdot 10^6$ A/m. This yields a moment of $(2.4 \pm 0.5) \cdot 10^{-9}$ Am considering the error when measuring the iron nanowire diameter in the SEM. This value corresponds very well to the experimentally obtained mean of $(2.1 \pm 0.1) \cdot 10^{-9}$ Am. A slightly smaller experimental value could originate from a tilting of the probe's magnetization at the edges of the nanowire end. The FeCNT probe thus has a very predictable magnetic moment that can be adjusted by choosing a different wire diameter. After further experiments to confirm this agreement, the

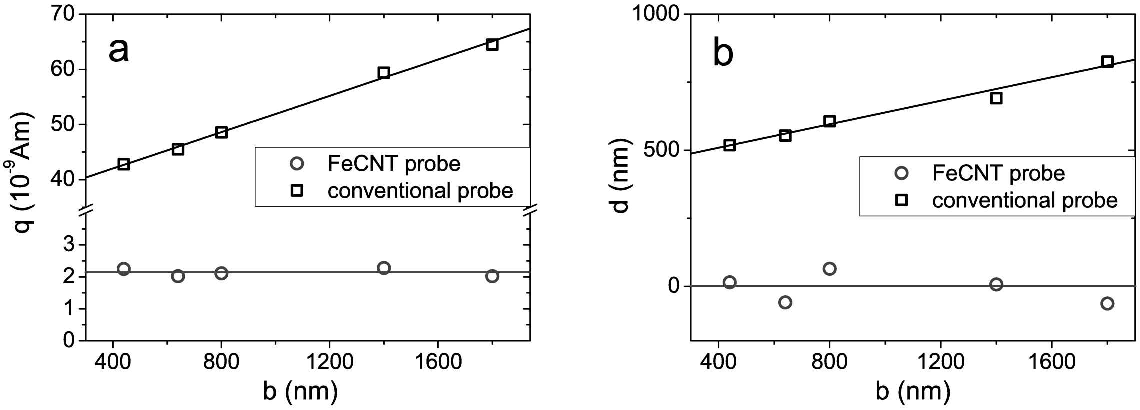

Figure 6.13: Comparison of the fitting results of a conventional probe (squares) and a FeCNT probe (circles): a) monopole moment q, b) monopole position d for different current line separations b. The solid lines should just guide the eye but do not reflect the underlying law.

calibration procedure could even be replaced by a simple geometry measurement of the FeCNT's iron core diameter in the SEM.

Fig. 6.13 shows the obtained values again in comparison to those obtained with the magnetically coated pyramid shaped tip. This plot visualizes very well how the monopole moment of the conventional probe increases with increased line distance b whereas the moment of the FeCNT remains constant. A once obtained calibration of the FeCNT probe is thus applicable for quantitative MFM measurements of samples with different magnetic structure geometries.[124]

Evaluation of the measurement error

The exact error of the calibration procedure is hard to evaluate. The noise of the phase shift signal is less then 4% of the measured value. The error in the Q-factor measurement is negligible; the calculated spring constant has an error of $< 7\%$ due to errors in the measurement of the cantilever dimensions. Deviations of the real gold line geometry from the measured value can lead to an error of up to 10% in the fitted monopole moment. Consequently, we estimate the maximum error of the fitted monopole moment to be $< 20\%$.

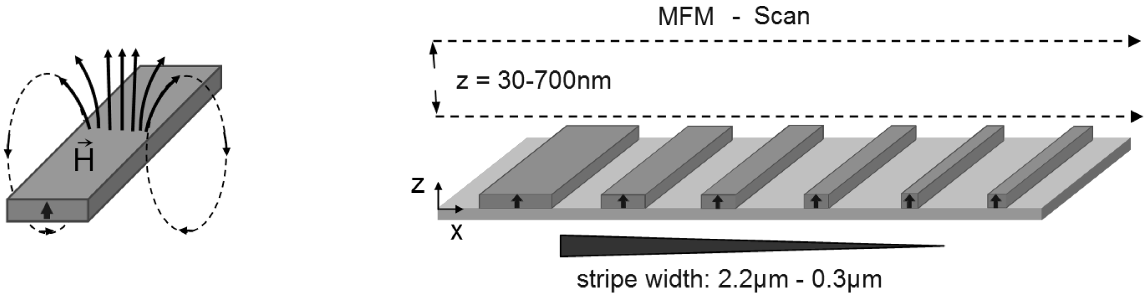

Figure 6.14: Left: Sketch of the magnetic stray field of a (Co/Pt)$_7$ stripe with perpendicular anisotropy. Right: Schematic of (Co/Pt)$_7$ stripes with varying width used for the MFM probe calibration to investigate the dependence of the probe parameters on the domain size.

6.5 CALIBRATION OF A FECNT PROBE USING MULTILAYER STRIPES

The calibration results in the previous section show that FeCNT MFM sensors allow a universally applicable probe calibration. In order to confirm this conclusion, a different calibration procedure was tested.* (Co/Pt)$_7$ multilayer stripes with varying width from 2.2 µm down to 300 nm and a height of 14 nm were used as reference samples with a well defined magnetic stray field to investigate the dependence of the probe parameters on the domain size (Fig. 6.14). The stripes were prepared by electron beam lithography with lift-off technique and electron beam evaporation of Co and Pt.[126] The multilayer architecture leads to a strong perpendicular anisotropy with a single domain remanent state after perpendicular saturation. Electrostatic potential differences between the stripes and the silicon substrate were minimized by the deposition of a few nanometers of carbon on top of the structure.

The calibration was again carried out with both a conventional magnetically coated MFM probe (VEECO MESP) and a FeCNT probe. The used FeCNT probe contained a 2 µm long and 32 nm wide iron nanowire. The MFM measurements where this time performed with a Digital Instruments 3100 SPM in the tapping/lift mode. For the derivation of the probe characteristics from the MFM scan, the point probe approximation[71] (Eq. 6.6) was used. The stray field derivative of the perpendicularly magnetized stripes was calculated based on the known saturation magnetization and the obtained topography images. This calculation was then used to model the corresponding MFM scan lines and fit them to the measured data. The fitting parameters were the probe monopole moment q and its position d as described in the previous section.

---

*This work was performed in cooperation with the Institute of Metallic Materials, IFW Dresden. The data evaluation was performed by Silvia Vock.[125] The calibration structures were prepared by Christoph Hassel from the University Duisburg-Essen, Department Experimental Physics.

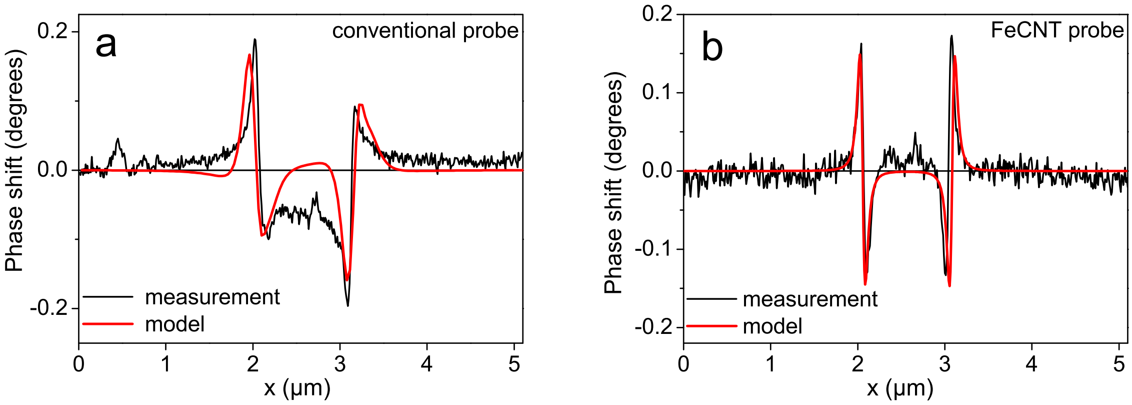

Figure 6.15: Average over 50 MFM linescans over a 1 µm wide $(Co/Pt)_7$ stripe taken with a) a conventional MFM probe and b) a FeCNT MFM probe. The black lines represent the measured data, the red lines show the fitted curve.

MFM measurements were performed with both probes on six $(Co/Pt)_7$ stripes with varying width. Before the measurement, the MFM probes and stripes were magnetized in the same direction. Consequently, an attractive interaction is expected. Each stripe was measured at a tip-sample distance of ∼70 nm, 50 scan lines were averaged to increase the signal to noise ratio. Fig. 6.15 shows such averaged line scans and the corresponding modeled data for a) a conventional MFM probe and b) a FeCNT MFM probe. The data obtained with the FeCNT probe can be modeled very well with the monopole model. In contrast, the asymmetric data obtained with the conventional probe indicates that the monopole model is inappropriate to describe this result. The probe thus needs to be approximated by a tilted dipole (shown in Fig. 6.15 a, the dipole fit is described in detail by Vock et al.[125]).

Fig. 6.16 summarizes the results of the calibration procedure and compares them to literature values. The probe monopole moment q and its distance d from the tip apex are plotted on a logarithmic scale as a function of the magnetic structure size. The error bars are based on the standard deviation of the values obtained at different lift heights (20 nm-120 nm). The coated MFM probe (MESP) shows an increase of the monopole moment and its position with increasing structure size whereas the parameters of the FeCNT probe stay constant. This confirms the results that have been obtained by the calibration with current carrying lines and proves that the FeCNT probe comes close to a true point monopole whose properties do not change depending on the sample's stray field geometry. The obtained mean monopole moment of the FeCNT probe is $(0.8 \pm 0.2) \cdot 10^{-9}$ Am. This is again comparable to the theoretical value of $1.4 \cdot 10^{-9}$ Am calculated from the nanowire geometry with a smaller diameter of 32 nm. This diameter constitutes an almost perfect monopole relative to the stripe dimensions of 300 nm and larger. The obtained distance $d = (85 \pm 30)$ nm is reasonable considering

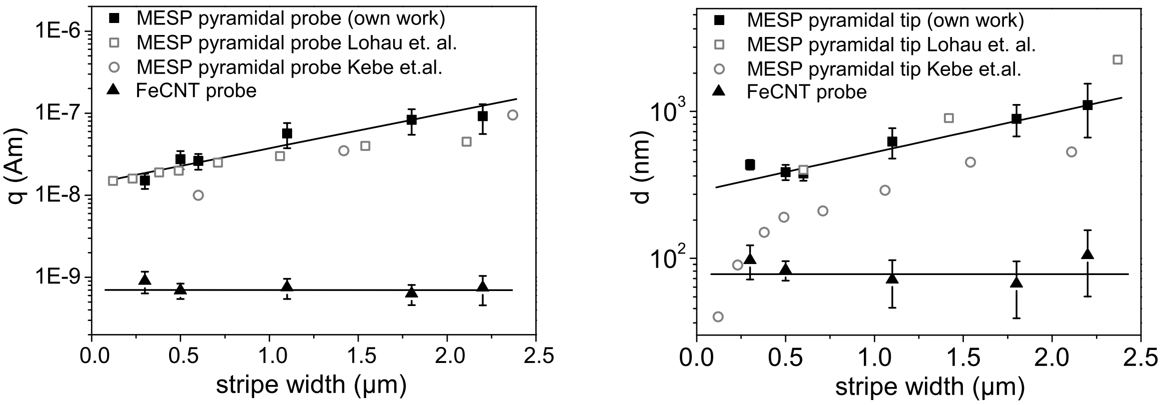

Figure 6.16: Fitted probe monopole moment q (left) and its position d (right) for a conventional probe and a FeCNT probe in comparison with literature values (Kebe et al.[18], Lohau et al.[17]). As described in the previous section, Kebe et al. used current carrying parallel lines whereas Lohau et al. employed ring structures to generate the reference stray field. This can lead to different dependencies, however, the trend is preserved. The solid lines represent a linear fit of the data and do not necessarily reflect the underlying physical law.

a FeCNT carbon shell thickness of approximately 30 nm. Small deviations from the ideal cylinder geometry at the wire end can cause the increased distance.

The above findings lead to the conclusion that the monopole approximation is an absolutely adequate model to describe the FeCNT. In contrast, the monopole model can only give a rough estimation of the parameters of a conventional MFM probe. It can only be used for quantitative MFM after extensive probe calibration.

6.6 Application of the calibration results for quantitative MFM

After the determination of all relevant properties of the FeCNT probe for a universal calibration it is now possible to perform quantitative MFM imaging. As a test sample for this a (Co/Pt)/Ru multilayer was chosen.[105,125] This ferromagnetic layer system features a strong perpendicular magnetic anisotropy and is of special interest for applications in perpendicular magnetic recording technology. It is composed of individual sputter deposited blocks of Co(0.4 nm)/Pt(0.7 nm) multilayers separated by a thin Ru spacer layer. The exact architecture is $[(\text{Co}(0.4\,\text{nm})/\text{Pt}(0.7\,\text{nm}))_8/\text{Ru}(0.9\,\text{nm})]_{18}$. The film is grown on a 2 nm Pt buffer layer and covered with 2 nm Pt.

In zero field, the sample is in a ferromagnetic band domain state with the perpendicular magnetization vertically correlated throughout all layers. The MFM image in

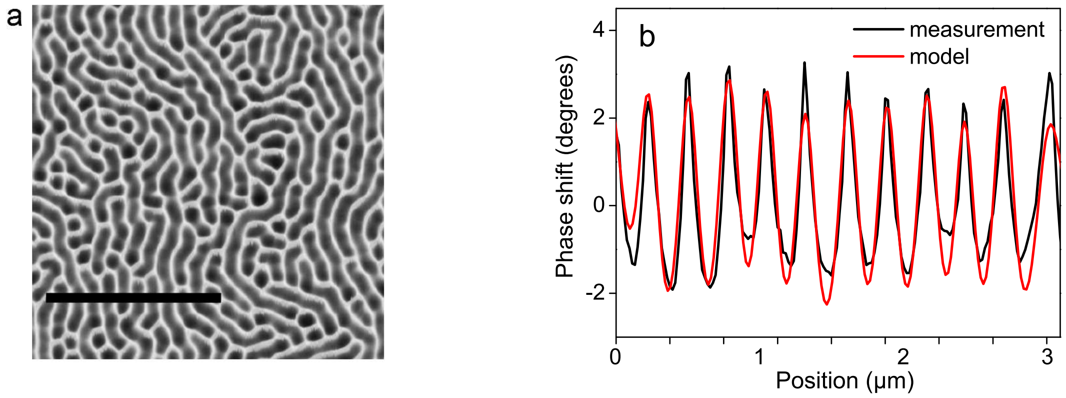

Figure 6.17: a) 7 µm×7 µm MFM scan of a (Co/Pt)/Ru multilayer in the ferromagnetic band domain state. b) Line section along the black line in the MFM image, the black line shows the MFM measurement, the red line the simulation using the fitted monopole moment of the FeCNT probe.

Fig. 6.17 a shows the neighboring domains with opposite magnetization and a width of approximately 180 nm. Using the calibrated probe, it is now possible to obtain quantitative information on the magnetization present in those domains.

The measured MFM signal is quantified by the same procedure as described in the previous chapter, only now the probe parameters are known and the sample magnetization is used as the optimization parameter. The sample's stray field is calculated from a positive/negative magnetic charge pattern derived by applying a discrimination level to the MFM data. Zero width domain walls are assumed. The tip properties q=7.54·10^{-10} Am and d=85 nm were applied. The MFM measurement of the multilayer film was performed in a lift height of z=50 nm, so the total height $z + d$ in which the MFM signal needs to be calculated is 135 nm.

The results of the modeling are shown in Fig. 6.17 b. The simulation was performed along the black line in Fig. 6.17 a, an optimum agreement is found for a sample magnetization $M = (440 \pm 135)$ kA/m. A volume averaging technique such as VSM (vibrating sample magnetometry) cannot give access to the local remanent sample magnetization. The saturation magnetization obtained from this global measurement is $M_{VSM} = (650 \pm 65)$ kA/m. The discrepancy between the two values is partially due to the non-vanishing width of the domain walls. However, the main reason is that the magnetization of the multilayer stacks is not perfectly perpendicular to the sample plane in the remanent state. There is a competition between anisotropy energy (E_k) and stray field energy (E_s) in the thin film sample. The magnetization of a band domain structure is only expected to lie completely perpendicular to the surface for a very large perpendicular anisotropy $E_k/E_s >> 1$. For smaller values the sample develops a non-homogeneous magnetization with considerable in-plane components.[127]

This reduces the perpendicular magnetization component which is measured in MFM leading to the smaller value obtained in the quantitative MFM analysis. In the shown case, the remaining perpendicular magnetization amounts to approximately 70% of the saturation magnetization.

These results demonstrate that the localized magnetization study with quantitative MFM allows a more detailed interpretation of the sample magnetization from a microscopic point of view. A monopole-like FeCNT probe is an ideal tool for such investigations.

6.7 QUANTITATIVE MFM ON PERMALLOY DOTS USING A FECNT PROBE

In this section MFM measurements on perpendicularly magnetized permalloy dots will be used as a third approach to confirm the applicability of the point monopole model to the FeCNT probe. A magnetic monopole moment corresponding to the calculated value from the FeCNT probe's geometry fits the experimental data. Furthermore, the gradient of the magnetic stray field at the FeCNT apex will be evaluated. Due to the small dimensions of the iron nanowire, this gradient can be very large and of potential use for sensor applications in magnetic resonance force microscopy.[*]

6.7.1 Probe calibration

Two FeCNT probes (in the following called J2 and K2, Fig. 6.18) were characterized by performing MFM on permalloy (Py) disks in a high external magnetic field of ∼2 T perpendicular to the Py film plane. The Py disk array was fabricated by photolithography and a lift-off process. The Py thickness is 40 nm, the disk diameter is 2.2 µm and the disks center-to-center distance is 6 µm. The saturation magnetization of the Py material is $M_s^{\mathrm{Py}}=7.6\cdot10^5$ A/m. The MFM experiments were performed at a temperature of 5 K in a high vacuum MFM setup at Ohio State University. A fiber-optic interferometer was used to detect the cantilever deflection.

Typical MFM images measured with FeCNT probe J2 in different probe sample distances z are presented in Fig. 6.19 a. The displayed MFM signal is the cantilever frequency shift monitored during the scan in a constant height above the Py disk

---

[*] This work was performed in close collaboration with the group of Prof. Chris Hammel at the Ohio State University, Columbus, USA. The measurement and data evaluation was performed by Yuri Obukhov.[128]

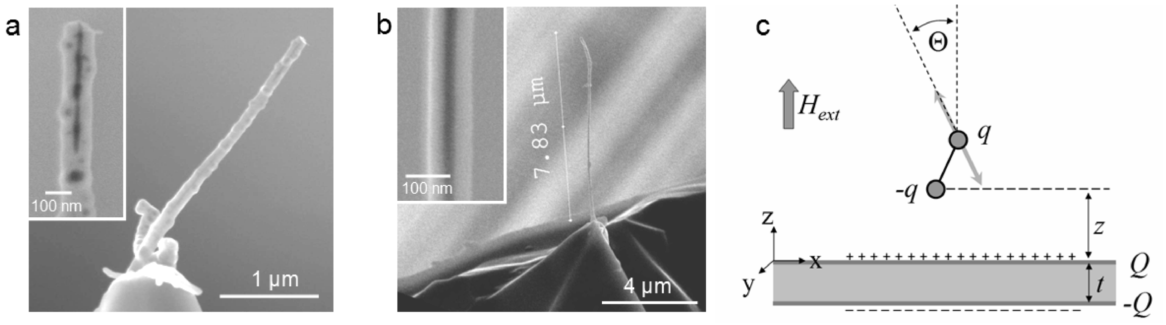

Figure 6.18: SEM images of the two FeCNT MFM probes a) J2 and b) K2. The insets show close-ups of the corresponding FeCNTs, the iron filling has a darker shade than the carbon shells. c) Monopole model of the FeCNT. A uniformly magnetized iron wire which is located at a distance z from the sample surface can be defined by its two monopoles q and -q. The sample, a Py disk of thickness t, is magnetized perpendicular to the disk plane in high external magnetic fields. The magnetization of the disk can be described by two sheets of magnetic charges with a charge density Q defined by the Py saturation magnetization. The angle Θ characterizes the cantilever tilt.

without any SPM feedback. The probe sample distance z was obtained by measuring the DC force acting on the cantilever at different distances (force vs. distance curve), providing the probe touch point (z=0) with an accuracy of 10-15 nm. The system does not have "in vacuum" vibration isolation, therefore the accuracy of the z measurement is defined by the time variation of the probe sample distance due to mechanical vibrations induced by boiling liquid helium. The amplitude of the cantilever oscillation was kept much smaller than the probe sample distance z. It was usually set to 10 nm peak-to-peak, for z values smaller than 80 nm it was reduced to 5 nm.

The cantilever frequency shift Δf due to a force gradient can be written as (see Eq. 3.6):

$$\Delta f(x,y) = -\frac{f_0}{2k_0}\frac{\partial F}{\partial z}(x,y)$$

where f_0 is the cantilever's initial resonance frequency, k is its spring constant and $\frac{\partial F}{\partial z}$ is the force gradient in the direction of the cantilever oscillation if this direction coincides with z.

To calculate the MFM force gradient $\frac{\partial F}{\partial z}$ two assumptions were made (see Fig. 6.18 c). First, the iron wire in the CNT is considered to be uniformly magnetized along its long axis. In this case its magnetization can be described by two monopoles q and $-q$ positioned at the ends of the wire. The monopole moment $q = \pi d^2/4 \cdot M_s^{\mathrm{Fe}}$ is defined by the diameter d of the iron wire and its saturation magnetization M_s^{Fe}. In the experiment a magnetic field of 2 T was used which is close to the saturation field of iron (2.2 T). If the iron wire is not exactly parallel to external field its magnetization might tilt several degrees away from the CNT's axis and the monopole at the wire

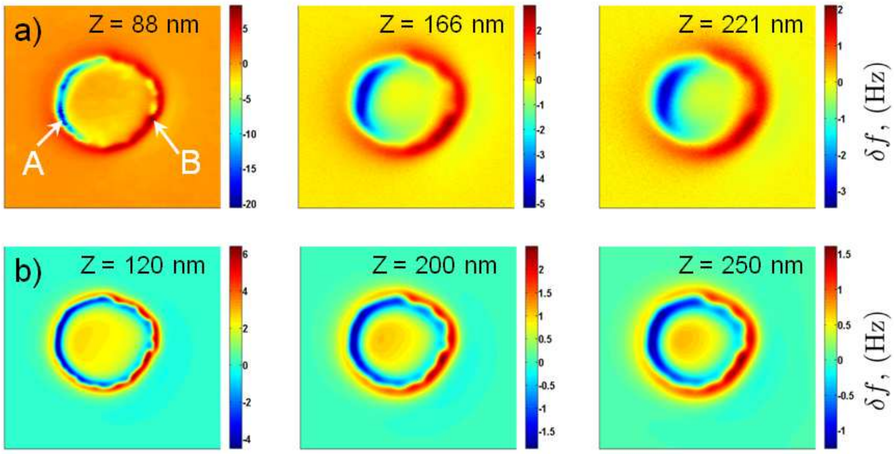

Figure 6.19: a) MFM images of a Py disk in a $\sim 2\,\mathrm{T}$ magnetic field perpendicular to the sample plane made with the FeCNT probe J2 in different probe sample distances z, scan size $4.5\,\mu\mathrm{m} \times 4.5\,\mu\mathrm{m}$. The horizontal axis corresponds to x, the vertical to y. The points A and B show the position of the minimum and maximum cantilever frequency shift (see text). b) Corresponding simulation of the MFM images using the model shown in Fig. 6.18 c. The simulations were calculated for the same probe sample distances z as in a), but the estimated carbon shell thickness of $\sim 30\,\mathrm{nm}$ was added.

end will be slightly reduced. However, for moderate FeCNT tilt angles ($\leq$ 20-30°) the monopole description is still reasonable. The second assumption is that the Py film is assumed to be saturated in the direction of the external field, perpendicular to the film plane. Consequently the magnetization of the Py film can be represented by two monopole layers with a charge per unit area $Q = M_s^{\mathrm{Py}}$ defined by the saturation magnetization of Py.

As shown in the previous sections, if the decay length of the sample's magnetic stray field is smaller than the iron wire length, the influence of the wire's monopole q which is positioned further away from the sample surface (see Fig. 6.18 c) on the MFM image can be neglected. The MFM force gradient induced by the sample's upper monopole layer can then be expressed as

$$\begin{aligned} \frac{\partial F}{\partial z}(x,y) &= \mu_0 \int \left.\frac{\partial H_z}{\partial z}\right|_z (x-x', y-y')\; Q(x',y')\; dx'dy' \\ &\equiv \mu_0 \left.\frac{\partial H_z}{\partial z}\right|_z * Q \end{aligned}$$

where H is the magnetic field created by the tip monopole $-q$ ($\mathbf{H} = -q\mathbf{r}/4\pi r^3$), $\mathbf{r}$ is the radius vector, and the sign $*$ stands for the convolution. The total MFM force gradient created by both Py monopole layers can be written as

$$\frac{\partial F}{\partial z} = \mu_0 \left.\frac{\partial H_z}{\partial z}\right|_z * Q - \mu_0 \left.\frac{\partial H_z}{\partial z}\right|_{z+t} * Q$$

where t is the Py film thickness. According to the above equations the MFM image is supposed to be centrally symmetric relative to the center of the Py disk. Nevertheless in Fig. 6.19a a considerable asymmetry in the x (horizontal) direction can be observed. This can be explained by the tilt of the cantilever and its oscillation relative to the z axis (Fig. 6.18 c). In the used setup this tilt is exactly in the xz plane and the tilt angle is $\Theta = 15\text{-}20°$. In this case the above MFM force gradient equation should be written as:

$$\frac{\partial \mathbf{F}}{\partial \mathbf{l}} = \mu_0 \left.\frac{\partial \mathbf{H}}{\partial \mathbf{l}}\right|_z * Q - \mu_0 \left.\frac{\partial \mathbf{H}}{\partial \mathbf{l}}\right|_{z+t} * Q \tag{6.7}$$

where $\mathbf{l}$ is a position vector in the direction of the cantilever oscillation. A calculation of $\frac{\partial \mathbf{H}}{\partial \mathbf{l}}$ in the given geometry yields:

$$\begin{aligned}
\frac{\partial \mathbf{H}}{\partial \mathbf{l}} &= \frac{1}{4\pi}\left[\frac{\partial H_x}{\partial x}\sin^2\Theta + \left(\frac{\partial H_x}{\partial z} + \frac{\partial H_z}{\partial x}\right)\sin\Theta\cos\Theta \right.\\
&+ \left.\frac{\partial H_z}{\partial z}\cos^2\Theta\right] \\
\frac{\partial H_x}{\partial x} &= -q\frac{r^2-3x^2}{4\pi r^5} \\
\frac{\partial H_x}{\partial z} &= \frac{\partial H_z}{\partial x} = q\frac{3xz}{4\pi r^5} \\
\frac{\partial H_z}{\partial z} &= -q\frac{r^2-3z^2}{4\pi r^5}
\end{aligned} \tag{6.8}$$

Using Eq. 6.7, MFM images of a Py disk were modeled. The FeCNT monopole and its position (corresponding to the carbon shell thickness) were adjusted to obtain the best agreement between experimental and simulated data. The shape of the disk is not exactly circular, therefore the shape of the disk boundary was modeled according to the MFM image in Fig. 6.19a at $z = 88$ nm. The results of this simulation are presented in Fig. 6.19b for the same values of z as in the experimental data plus a carbon shell thickness of ~ 30 nm (evaluated later) which increases the distance of the probe monopole to the sample surface. The parameters used in the model are: saturation magnetization of the iron wire in the FeCNT $M_s^{\mathrm{Fe}}=1.7\cdot 10^6$ A/m, diameter of the iron wire d=16 nm, resulting FeCNT monopole $q=3.5\cdot 10^{-10}$ Am, saturation magnetization of the Py film $M_s^{\mathrm{Py}}=7.6\cdot 10^5$ A/m and cantilever tilt Θ=20°.

The results of the proposed model (Fig. 6.19b) are in good qualitative and quantitative agreement with the experimental data in Fig. 6.19a. However, there is a considerable difference between model and experiment close to the surface at $z = 88\,\mathrm{nm}$. In the experiment, the negative cantilever frequency shift on the left side of the Py disk (see point A in Fig. 6.19a, $z = 88\,\mathrm{nm}$) is substantially bigger than what is expected from the model. This can be attributed to the electrostatic attraction between the FeCNT probe and the Py disk which adds a negative frequency shift. This effect becomes smaller at larger probe sample distances.

6.7.2 Quantitative MFM data evaluation

For a quantitative comparison of the model with the experiment the maximum positive frequency shift on the right side of the disk (for the image in Fig. 6.19a, $z = 88\,\mathrm{nm}$, it corresponds to point B) was chosen. Point B is located outside of the Py disk boundary, so the probe-sample distance is bigger and the contribution of the electrostatic attraction to the total force is smaller. However, at small probe-sample distances the measurements will still have an error induced by electrostatic forces (the magnetic field gradient of the probe or sample at point B will thus be somewhat underestimated close to the sample surface).

The results for both FeCNT probes J2 and K2 are show in Fig. 6.20. The measurements of the two probes at point B are in very good quantitative agreement with the model (solid line, calculated using eq. 6.7. To visually confirm the agreement between experiment and model, the simulated curve was shifted by the corresponding shell thickness to match the measured data (dotted lines in Fig. 6.20). Only the measured data points close to the sample surface deviate from the calculated curve which can be explained by additional electrostatic forces. The best agreement is achieved with a probe monopole moment q=3.5·10^{-10} Am which corresponds exactly to the moment calculated from the nanowire's geometry. The difference in z (probe sample distance) between the experimental data and the model corresponds to the distance of the magnetic monopole to the tube end, namely the carbon shell thickness. This value can be different for different FeCNT. For J2 a shell thickness of $\sim 30\,\mathrm{nm}$ is obtained which is in good agreement with what can be observed in the SEM image (inset of Fig. 6.18 a). The measurement with K2 suggests a shell thickness of $\sim 60\,\mathrm{nm}$. This bigger shell thickness might be attributed to the roughness of the carbon shell. Since this FeCNT was cut with the FIB, the bigger shift in z could be also explained by a FIB induced damage to the topmost iron part.

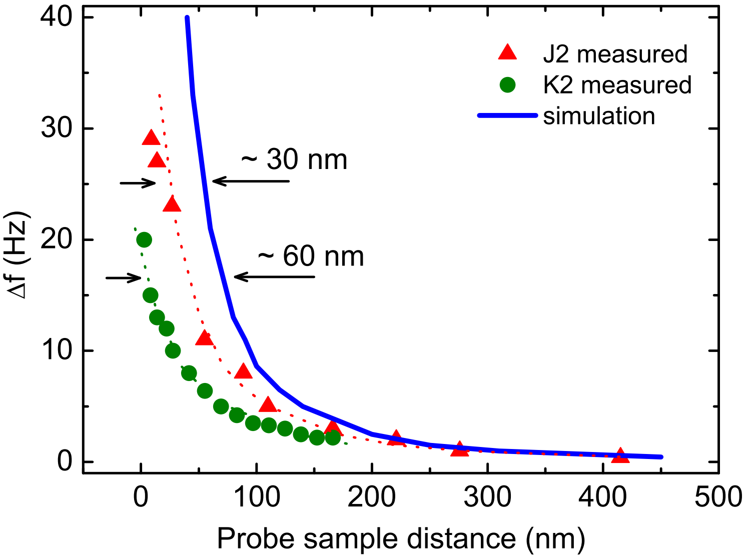

Figure 6.20: MFM response at point B (Fig. 6.19a) for different probe sample distances z. The experimental data for the FeCNT probe J2 is displayed by triangles, the data for probe K2 by circles. The solid blue line is the simulation obtained using the monopole model in Fig. 6.18 c. The experimental data and the model differ by a shift in z (the dotted lines correspond to the shifted simulated curve). This shift corresponds to the distance between the actual position of the magnetic monopole and the measured z touch point which is mainly determined by the FeCNT's carbon shell thickness.

These results confirm that a FeCNT can be modeled as a monopole with a magnetic charge defined by the iron wire diameter positioned at a small distance from the CNT's end. With the knowledge of the magnetic charge of the monopole q one can directly image the magnetic field gradient generated by the sample:

$$\Delta f(x,y,z) = \frac{f_0}{2k} q \cdot \mu_0 \frac{\partial \mathbf{H}}{\partial \mathbf{l}}(x,y,z) \tag{6.9}$$

Unlike in Eq. 6.7, $\frac{\partial \mathbf{H}}{\partial \mathbf{l}}$ here is the sample field gradient. Using Eq. 6.9 the value of the sample's magnetic field gradient in different distances z from the Py disk surface can be extracted from the frequency shift data in Fig. 6.20. This evaluation is shown in Fig. 6.21 for the measurement with FeCNT probe J2. The actually measured probe sample distance is displayed without adding the carbon shell thickness of $\sim 30\,\text{nm}$. This and the logarithmic scale are the reasons for the apparent saturation of the curve at small probe sample distances. At a distance of $\sim 20\,\text{nm}$, a field gradient of $1.5 \cdot 10^6\,\text{T/m}$ was measured.

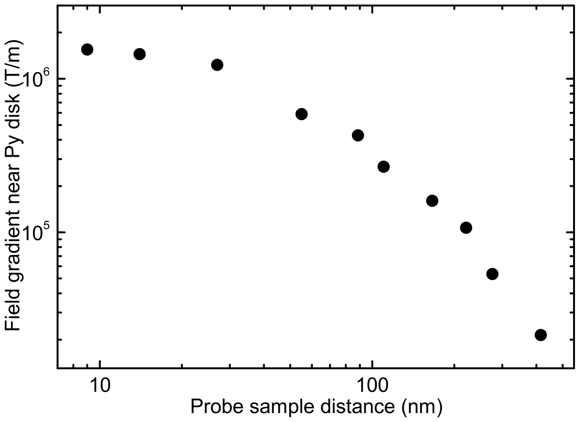

Figure 6.21: Magnetic field gradient at point B (Fig. 6.19a) near the Py dot measured at different probe-sample distances using FeCNT probe J2.

6.7.3 Evaluation of the FeCNT field gradient

Using the proposed monopole model it is also possible to reconstruct the field gradient near the tip of the FeCNT probe. The probe gradient is obtained by calculating $\frac{\partial H}{\partial z} = 2q/4\pi(z + z_s)^3$ (z_s is the carbon shell thickness) with the probe monopole moment q and z_s obtained from the best fit between measurement and simulation in Fig. 6.20. For each measurement height, the shift between the simulated curve and the measured curve is evaluated separately, so a slightly different z_s is obtained for each point. Particularly for the measurement close to the sample surface, z_s is bigger than the mean 30 nm. This reflects the increased influence of additional effects , e.g. electrostatics or mechanical vibrations, and complicates the exact reconstruction of the FeCNT's field gradient. Therefore it will be further on called an effective field gradient. The results are presented in Fig. 6.22. The black squares represent the described effective field gradient. Due to the carbon shell thickness and electrostatic influences the gradient saturates in the logarithmic plot at small probe-sample distances. A maximum field gradient of $\sim 6{\cdot}10^5$ T/m is detected near the FeCNT tip at a probe-sample distance of $\sim$ 10 nm. If the electrostatic interactions close to the sample surface are disregarded and a constant carbon shell thickness of 30 nm is assumed, the probe gradient in a distance of 10 nm increases to $\sim 1.2{\cdot}10^6$ T/m (represented by the open gray squares). The open gray diamonds show the theoretical field gradient of the iron nanowire in the case of no carbon shell. A maximum gradient of $\sim 9{\cdot}10^7$ T/m can be obtained at 10 nm distance from the iron wire. Unfortunately, this larger gradient is not experimentally accessible in the shown case due to the, in comparison to the iron wire diameter, relatively thick carbon shell. A higher gradient can thus be expected

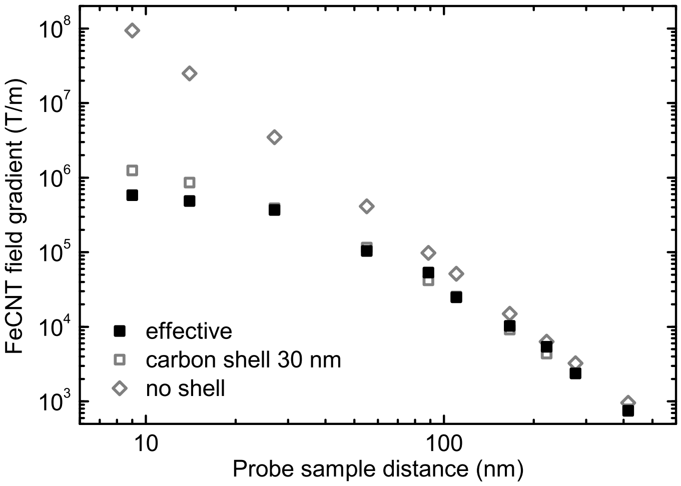

Figure 6.22: Effective and theoretical magnetic field gradient close to the tip of FeCNT J2. The graphs are obtained from the fit in Fig. 6.20 using the monopole model.

for a smaller shell size. Decreasing the carbon thickness by changing the FeCNT growth conditions or by electron beam induced oxidation of parts of the shell in water atmosphere (see section 5.2) could open a way for producing high gradient FeCNT probes.

The probe's magnetic field gradient is a very important parameter for high resolution magnetic force detection and for magnetic resonance force microscopy (MRFM) in particular. It defines the minimal magnetic moment that can be detected. The state of the art maximum value of the field gradient is $4.2{\cdot}10^6$ T/m, demonstrated in MRFM imaging of the Tobacco Mosaic virus.[129] If the carbon shell thickness can be reduced, the FeCNT could also be employed as a convenient probe for high resolution high sensitivity MRFM.

The results presented in this section confirm that a FeCNT can be modeled as a monopole with a magnetic charge defined by the diameter of the iron wire enclosed in the carbon nanotube and the typical saturation magnetization of bcc iron. The FeCNT probes are thus unique for an application in quantitative MFM. Knowing the magnetic charge of the monopole q one can directly image the field gradient generated by the sample as demonstrated for a Py disk.

SUMMARY AND OUTLOOK

Iron filled carbon nanotubes are a very promising nanoscale magnetic material with unique magnetic and mechanical properties. The carbon shells protect the iron core from oxidation and mechanical damage thus enabling a wide range of applications that require a long-term stability. The magnetic properties of the enclosed nanowire are in part determined by its small size and elongated shape. A thorough understanding of these properties is a necessary precondition for an application of FeCNT, e.g. as sensors or in other fields. Various investigations have already been conducted on the magnetic properties of large ensembles of magnetic nanowires,[46,60,130] however, due to the common inhomogeneity of the material the obtained results can usually not be transfered to individual nanowires.

In this work, magnetic force microscopy was used to investigate the magnetic properties of individual FeCNT. These measurements showed that the iron nanowire enclosed in a FeCNT exhibits a single domain behavior and is magnetized along the long wire axis in the remanent state. The two monopoles of opposing polarity are located at the wire extremities. TEM measurements revealed deviations from the ideal cylindrical structure of the nanowire that can act as additional weaker stray field sources. MFM combined with the application of external magnetic fields allowed a determination of coercive properties of individual FeCNT. Switching fields in the range of 100-400 mT were found due to the large shape anisotropy of the iron nanowires. Cantilever magnetometry measurements showed that the switching of an individual iron nanowire occurs in a very narrow field distribution at low temperatures. This can be attributed to a thermally assisted magnetization reversal mechanism with the nucleation and propagation of a domain wall.

The very defined magnetic properties of individual FeCNT combined with their mechanical strength make them ideal candidates for an application as high resolution high stability MFM probes. The fabrication of such probes could be achieved with the help of a micromanipulation setup in the SEM. This method is very time consuming, yet it yields very stable probes for first experiments. Electron beam induced carbon etching allowed to remove empty CNT sections to position the magnetically active iron nanowire at the very end of the tube.

The FeCNT MFM probes show a sub 25 nm magnetic resolution which is competitive with other high resolution probes currently available on the market. The resolution could still be increased in the future by using FeCNT with a very thin carbon shell filled with nanowires of smaller diameter. MFM measurements with FeCNT MFM probes in external fields showed that the magnetization of these probes is exceptionally stable compared to coated MFM probes. This greatly simplifies the data evaluation of such applied field MFM measurements. Applying horizontal fields in MFM is so far widely regarded as almost useless because of the artifacts introduced by coated probes. FeCNT probes can solve this problem. This positive effect would be even more pronounced in the case of a CNT attached parallel to the cantilever axis along the direction of the external in-plane field. This field should then only further stabilize the probe monopole and horizontal fields of arbitrary value could be used without any distortion of the probe moment. This is a unique property of FeCNT probes.

The emphasis of this work was put on the calibration of FeCNT probes to enable straightforward quantitative MFM measurements. The defined shape allows an appropriate application of the point monopole description. Three different calibration techniques were tested in order to prove this assumption. First, microscale parallel current carrying lines that produce a defined magnetic field were used as calibration structures to determine the effective magnetic moment of different MFM probes. The line geometry was varied in order to produce multiple magnetic field decay lengths and investigate the influence on the effective probe moment. Electrostatic interactions between probe and sample were minimized by a shielding layer. It was found that while the effective magnetic monopole moment of a coated probe increases with an increasing sample stray field decay length, the effective moment of a FeCNT MFM probe remains constant. For the first time, this enables a MFM probe calibration that stays valid for a large variety of magnetic samples. Reliable quantitative information on the sample stray field derivative can be obtained. Furthermore, the fitted monopole moment of a FeCNT probe is consistent with the moment calculated from the nanowire geometry and the saturation magnetization of iron. When more statistics of the correlation between the diameter of the iron nanowire and the monopole moment obtained by the calibration has been gathered, the time consuming calibration could be omitted and the FeCNT probe could just be characterized by the monopole moment determined from the iron wire diameter. This would make the application of FeCNT probes for quantitative MFM even more simple.

The above findings were confirmed by a calibration using multilayer stripes with perpendicular anisotropy. The stripe width was varied to check the dependence of the probe parameters on the sample's domain size. Again, the effective monopole moment of FeCNT probes was found to stay constant when measuring different domain sizes. With the help of a calibrated FeCNT MFM probe it was possible to determine the local remanent magnetization of a (Co/Pt)/Ru multilayer sample from MFM measurements. This has so far not been possible with volume averaging techniques for magnetization measurements. A detailed interpretation of a sample's magnetization from a microscopic point of view is thus possible with a calibrated FeCNT probe.

Finally, MFM images of permalloy dots saturated in the out of plane direction were used to determine a FeCNT probe's magnetic monopole moment. The known effective probe moment then allowed a quantitative evaluation of the sample's magnetic field gradient. Also, the magnetic field gradient at the tip of a FeCNT probe was obtained. The effective gradient of $\sim 6{\cdot}10^5\,\mathrm{T/m}$ is much smaller then the theoretically possible $9{\cdot}10^7\,\mathrm{T/m}$ at 10 nm distance from the nanowire end. This is mainly due to the 30 nm carbon shell surrounding the nanowire which increases the effective probe sample distance. If the carbon shell thickness could be reduced, high gradient FeCNT probes could be well suited for magnetic resonance force microscopy where a large gradient is needed.

The proven monopole character of FeCNT probes should also facilitate the imaging of in-plane sample stray fields. This could for example be achieved by an in-plane vibration of the probe. This way, the field gradient parallel to the sample surface could be unambiguously imaged.

The summarized results show the great potential of FeCNT as probes for all relevant MFM techniques. A future challenge will be to find a larger scale approach for their fabrication. The direct growth of an individual FeCNT on a silicon cantilever could be envisioned with the help of a specially designed CVD reactor and the use of prepositioned nanoscale catalyst particles. This would clearly pave the way for new kinds of standard MFM measurements in various sectors of research that have so far not been possible with conventional probes.

BIBLIOGRAPHY

[1] S. S. P. Parkin, M. Hayashi, and L. Thomas. Magnetic domain-wall racetrack memory. *Science*, 320(5873):190–194, 2008.

[2] R. J. Tseng, C. L. Tsai, L. P. Ma, and J. Y. Ouyang. Digital memory device based on tobacco mosaic virus conjugated with nanoparticles. *Nat. Nanotechnol.*, 1(1):72–77, 2006.

[3] J. Lu, S. H. Yang, K. M. Ng, C. H. Su, C. S. Yeh, Y. N. Wu, and D. B. Shieh. Solid-state synthesis of monocrystalline iron oxide nanoparticle based ferrofluid suitable for magnetic resonance imaging contrast application. *Nanotechnology*, 17(23):5812–5820, 2006.

[4] Y. Krupskaya, C. Mahn, A. Parameswaran, A. Taylor, K. Kramer, S. Hampel, A. Leonhardt, M. Ritschel, B. Büchner, and R. Klingeler. Magnetic study of iron-containing carbon nanotubes: Feasibility for magnetic hyperthermia. *J. Magn. Magn. Mater.*, 321(24):4067–4071, 2009.

[5] B. Thiesen and A. Jordan. Clinical applications of magnetic nanoparticles for hyperthermia. *Int. J. Hyperthermia*, 24(6):467–474, 2008.

[6] W. M. Hassen, C. Chaix, A. Abdelghani, F. Bessueille, D. Leonard, and N. Jaffrezic-Renault. An impedimetric DNA sensor based on functionalized magnetic nanoparticles for HIV and HBV detection. *Sens. Actuators B*, 134(2):755–760, 2008.

[7] G. K. Kouassi and J. Irudayaraj. Magnetic and gold-coated magnetic nanoparticles as a DNA sensor. *Anal. Chem.*, 78(10):3234–3241, 2006.

[8] N. R. Wilson and J. V. Macpherson. Carbon nanotube tips for atomic force microscopy. *Nat. Nanotechnol.*, 4(8):483–491, 2009.

[9] K. Lipert, S. Bahr, F. Wolny, P. Atkinson, U. Weissker, T. Mühl, O. Schmidt, B. Büchner, and R. Klingeler. An individual iron nanowire-filled carbon nanotube probed by micro-hall magnetometry. *Appl. Phys. Lett.*, 97:212503, 2010.

[10] J. J. Saenz, N. Garcia, P. Grütter, E. Meyer, H. Heinzelmann, R. Wiesendanger, L. Rosenthaler, H. R. Hidber, and H. J. Güntherodt. Observation of magnetic forces by atomic force microscopy. *J. Appl. Phys.*, 62(10):4293, 1987.

[11] P. Grütter, D. Rugar, and H. J. Mamin. Magnetic force microscopy of magnetic materials. *Ultramicroscopy*, 47(4):393, 1992.

[12] D. Rugar, H. J. Mamin, P. Güthner, S. E. Lambert, J. E. Stern, I. McFadyen, and T. Yogi. Magnetic force microscopy: General principles and application to longitudinal recording media. *J. Appl. Phys.*, 68(3):1169, 1990.

[13] E. F. Wassermann, M. Thielen, S. Kirsch, A. Pollmann, H. Weinforth, and A. Carl. Fabrication of large scale periodic magnetic nanostructures. *J. Appl. Phys.*, 83(3):1753, 1998.

[14] U. Wolff, A. Singh, L. Schultz, and V. Neu. Switching behaviour of patterned $SmCo_5$ thin films investigated by magnetic force microscopy. *J. Magn. Magn. Mater.*, 310(2):2210, 2007.

[15] M. R. Koblischka, U. Hartmann, and T. Sulzbach. Improving the lateral resolution of the MFM technique to the 10 nm range. *J. Magn. Magn. Mater.*, 272-276:2138, 2004.

[16] K. Babcock. Magnetic force microscopy: Recent advances and applications. *Mat. Res. Soc. Symp. proc.*, 355:311, 1995.

[17] J. Lohau, S. Kirsch, A. Carl, G. Dumpich, and E. F. Wassermann. Quantitative determination of effective dipole and monopole moments of magnetic force microscopy tips. *J. Appl. Phys.*, 86(6):3410, 1999.

[18] Th. Kebe and A. Carl. Calibration of magnetic force microscopy tips by using nanoscale current-carrying parallel wires. *J. Appl. Phys.*, 95(3):775, 2004.

[19] Z. Deng, E. Yenilmez, J. Leu, J. E. Hoffman, E. W. J. Straver, H. Dai, and K. A. Moler. Metal-coated carbon nanotube tips for magnetic force microscopy. *Appl. Phys. Lett.*, 85(25):6263, 2004.

[20] T. Arie, H. Nishijima, S. Akita, and Y. Nakayama. Carbon-nanotube probe equipped magnetic force microscope. *J. Vac. Sci. Technol., B*, 18(1):104, 2000.

[21] S. Iijima. Helical microtubules of graphitic carbon. *Nature*, 354(6348):56–58, 1991.

[22] X. Wang, Q. Li, J. Xie, Z. Jin, J. Wang, Y. Li, K. Jiang, and S. Fan. Fabrication of ultralong and electrically uniform single-walled carbon nanotubes on clean substrates. *Nano Lett.*, 9(9):3137–3141, 2009.

[23] C. N. R. Rao, B. C. Satishkumar, A. Govindaraj, and M. Nath. Nanotubes. *ChemPhysChem*, 2(2):78–105, 2001.

[24] R. Saito, G. Dresselhaus, and M. S. Dresselhaus. Trigonal warping effect of carbon nanotubes. *Phys. Rev. B: Condens. Matter*, 61(4):2981–2990, 2000.

[25] S. J. Tans, A. R. M. Verschueren, and C. Dekker. Room-temperature transistor based on a single carbon nanotube. *Nature*, 393(6680):49–52, 1998.

[26] D. Qian, G. Wagner, and W. Liu. Mechanics of carbon nanotubes. *Appl. Mech. Rev.*, 55:495, 2002.

[27] E. Brown, L. Hao, J. C. Gallop, and J. C. Macfarlane. Ballistic thermal and electrical conductance measurements on individual multiwall carbon nanotubes. *Appl. Phys. Lett.*, 87(2):023107, 2005.

[28] D. J. Yang, S. G. Wang, Q. Zhang, P. J. Sellin, and G. Chen. Thermal and electrical transport in multi-walled carbon nanotubes. *Phys. Lett. A*, 329(3):207–213, 2004.

[29] P. Poncharal, Z. L. Wang, D. Ugarte, and W. A. de Heer. Electrostatic deflections and electromechanical resonances of carbon nanotubes. *Science*, 283(5407):1513, 1999.

[30] K. M. Lee, B. Lukic, A. Magrez, J. W. Seo, G. A. D. Briggs, A. J. Kulik, and L. Forro. Diameter-dependent elastic modulus supports the metastable-catalyst growth of carbon nanotubes. *Nano Lett.*, 7(6):1598, 2007.

[31] T. W. Ebbesen and P. M. Ajayan. Large-scale synthesis of carbon nanotubes. *Nature*, 358(6383):220–222, 1992.

[32] T. Guo, P. Nikolaev, A. Thess, D. T. Colbert, and R. E. Smalley. Catalytic growth of single-walled nanotubes by laser vaporization. *Chem. Phys. Lett.*, 243(1-2):49–54, 1995.

[33] M. Endo, T. Hayashi, Y. A. Kim, and H. Muramatsu. Development and application of carbon nanotubes. *Jpn. J. Appl. Phys.*, 45(6A):4883, 2006.

[34] C. Müller, S. Hampel, D. Elefant, K. Biedermann, A. Leonhardt, M. Ritschel, and B. Büchner. Iron filled carbon nanotubes grown on substrates with thin metal layers and their magnetic properties. *Carbon*, 44(9):1746, 2006.

[35] C. Ducati, I. Alexandrou, M. Chhowalla, G. A. J. Amaratunga, and J. Robertson. Temperature selective growth of carbon nanotubes by chemical vapor deposition. *J. Appl. Phys.*, 92(6):3299, 2002.

[36] P. Mauron, C. Emmenegger, A. Zuttel, C. Nutzenadel, P. Sudan, and L. Schlapbach. Synthesis of oriented nanotube films by chemical vapor deposition. *Carbon*, 40(8):1339, 2002.

[37] L. Dai, A. Patil, X. Gong, Z. Guo, L. Liu, Y. Liu, and D. Zhu. Aligned nanotubes. *ChemPhysChem*, 4(11):1150, 2003.

[38] C. Bower, W. Zhu, S. Jin, and O. Zhou. Plasma-induced alignment of carbon nanotubes. *Appl. Phys. Lett.*, 77(6):830, 2000.

[39] P. M. Ajayan and S. Iijima. Capillarity-induced filling of carbon nanotubes. *Nature*, 361(6410):333–334, 1993.

[40] A. Loiseau and H. Pascard. Synthesis of long carbon nanotubes filled with Se, S, Sb and Ge by the arc method. *Chem. Phys. Lett.*, 256(3):246–252, 1996.

[41] Y. C. Sui, R. Skomski, K. D. Sorge, and D. J. Sellmyer. Nanotube magnetism. *Appl. Phys. Lett.*, 84(9):1525–1527, 2004.

[42] R Skomski. Nanomagnetics. *J. Phys. Condens. Matter*, 15(20):R841, 2003.

[43] L. Sun, Y. Hao, C. L. Chien, and P. C. Searson. Tuning the properties of magnetic nanowires. *IBM Journal of Research and Development*, 49(1):79, 2005.

[44] Stephen Blundell. *Magnetism in condensed matter.* Oxford University Press, 2001.

[45] Nicolas Pilet. *The relation between magnetic hysteresis and the micromagnetic state explored by quantitative magnetic force microscopy.* PhD thesis, University of Basel, 2006.

[46] D. J. Sellmyer, M. Zheng, and R. Skomski. Magnetism of Fe, Co and Ni nanowires in self-assembled arrays. *J. Phys. Condens. Matter*, 13(25):R433, 2001.

[47] C. Kittel. Physical theory of ferromagnetic domains. *Rev. Mod. Phys.*, 21(4):541, 1949.

[48] N. Kawai and A. Sawaoka. Effect of hydrostatic pressure on the magnetocrystalline anisotropy of iron and nickel. *J. Phys. Chem. Solids*, 29(4):575–580, 1968.

[49] E. C. Stoner and E. P. Wohlfarth. A mechanism of magnetic hysteresis in heterogeneous alloys. *Philos. Trans. R. Soc. London, Ser. A*, 240(826):599–642, 1948.

[50] D. Weller, A. Moser, L. Folks, M. E. Best, W. Lee, M. F. Toney, M. Schwickert, J. U. Thiele, and M. F. Doerner. High K_u materials approach to 100 Gbits/in^2. *IEEE Trans. on Magn.*, 36(1):10, 2000.

[51] Christian Müller. *Grundlegende Untersuchungen zum CVD-Wachstum Fe-gefüllter Kohlenstoff-Nanoröhren.* PhD thesis, Technische Universität Dresden, 2007.

[52] Amikam Aharoni. *Introduction to the theory of ferromagnetism.* Oxford Science Publications, 1996.

[53] T. Mühl, D. Elefant, A. Graff, R. Kozhuharova, A. Leonhardt, I. Mönch, M. Ritschel, P. Simon, S. Groudeva-Zotova, and C. M. Schneider. Magnetic properties of aligned Fe-filled carbon nanotubes. *J. Appl. Phys.*, 93(10):7894, 2003.

[54] A. Leonhardt, S. Hampel, C. Müller, I. Mönch, R. Koseva, M. Ritschel, D. Elefant, K. Biedermann, and B. Büchner. Synthesis, properties, and applications of ferromagnetic-filled carbon nanotubes. *Chem. Vap. Deposition*, 12(6):380, 2006.

[55] Y.S. Chen, J.H. Huang, J.L. Hu, C.C. Yang, and W.P. Kang. Synthesis of single-walled carbon nanotubes produced using a three layer Al/Fe/Mo metal catalyst and their field emission properties. *Carbon*, 45(15):3007, 2007.

[56] H. Hongo, F. Nihey, T. Ichihashi, Y. Ochiai, M. Yudasaka, and S. Iijima. Support materials based on converted aluminum films for chemical vapor deposition growth of single-wall carbon nanotubes. *Chem. Phys. Lett.*, 380(1-2):158, 2003.

[57] L. Huang, X. Cui, B. White, and S. O'Brien. Long and oriented single-walled carbon nanotubes grown by ethanol chemical vapor deposition. *J. Phys. Chem. B*, 108:16451, 2004.

[58] V. I. Telnoi, K. V. Kiruanov, V. I. Yermolaev, and I. B. Rabinovich. Thermochemistry of dicyclopentadienyl compounds of transition-elements of 3d-series of periodic system. *Doklad. Akad. Nauk SSSR*, 220:1088, 1975.

[59] C. Müller, D. Golberg, A. Leonhardt, S. Hampel, and B. Büchner. Growth studies, TEM and XRD investigations of iron-filled carbon nanotubes. *Phys. Stat. Sol. A*, 203(6):1064, 2006.

[60] S. Hampel, A. Leonhardt, D. Selbmann, K. Biedermann, D. Elefant, C. Müller, T. Gemming, and B. Büchner. Growth and characterization of filled carbon nanotubes with ferromagnetic properties. *Carbon*, 44(11):2316, 2006.

[61] Ulrich Killian and Christine Weber, editors. *Lexikon der Physik*. Spektrum Akademischer Verlag, 2000.

[62] G. I. Goldstein, D. E. Newbury, P. Echlin, D. C. Joy, C. Fiori, and E. Lifshin. *Scanning electron microscopy and x-ray microanalysis*. Plenum Press, New York, 1981.

[63] G. Binnig, H. Rohrer, C. Gerber, and E. Weibel. Surface studies by scanning tunneling microscopy. *Phys. Rev. Lett.*, 49(1):57–61, 1982.

[64] G. Binnig, C. F. Quate, and C. Gerber. Atomic force microscope. *Phys. Rev. Lett.*, 56(9):930–933, 1986.

[65] U. Hartmann. Magnetic force microscopy. *Annu. Rev. Mater. Sci.*, 29:53–87, 1999.

[66] *http://www.nanosensors.com*. July 2010.

[67] O. Wolter, T. Bayer, and J. Greschner. Micromachined silicon sensors for scanning force microscopy. *J. Vac. Sci. Technol., B*, 9(2):1353–1357, 1991.

[68] Y. Martin and H. K. Wickramasinghe. Magnetic imaging by force microscopy with 1000 Å resolution. *Appl. Phys. Lett.*, 50(20):1455–1457, 1987.

[69] Thomas Kebe. Magnetkraftmikroskopische Untersuchungen an stromführenden parallelen Leiterbahnen. Diploma thesis, Gerhard-Mercator-Universität Duisburg, 2002.

[70] U. Hartmann. Fundamentals and special applications of noncontact scanning force microscopy. *Adv. El. El. Phys.*, 87:49–200, 1994.

[71] U. Hartmann. The point dipole approximation in magnetic force microscopy. *Phys. Lett. A*, 137(9):475, 1989.

[72] A. Wadas and P. Grütter. Theoretical approach to magnetic force microscopy. *Phys. Rev. B*, 39(16):12013, 1989.

[73] R. Engel-Herbert, D. M. Schaadt, and T. Hesjedal. Analytical and numerical calculations of the magnetic force microscopy response: A comparison. *J. Appl. Phys.*, 99(11):113905, 2006.

[74] H. J. Hug, B. Stiefel, P. J. A. van Schendel, A. Moser, R. Hofer, S. Martin, H. J. Güntherodt, S. Porthun, L. Abelmann, J. C. Lodder, G. Bochi, and R. C. O'Handley. Quantitative magnetic force microscopy on perpendicularly magnetized samples. *J. Appl. Phys.*, 83(11):5609–5620, 1998.

[75] P. J. A. van Schendel, H. J. Hug, B. Stiefel, S. Martin, and H. J. Güntherodt. A method for the calibration of magnetic force microscopy tips. *J. Appl. Phys.*, 88(1):435–445, 2000.

[76] M. R. Scheinfein, J. Unguris, D. T. Pierce, and R. J. Celotta. High spatial-resolution quantitative micromagnetics (invited). *J. Appl. Phys.*, 67(9):5932–5937, 1990.

[77] T. Göddenhenrich, H. Lemke, M. Muck, U. Hartmann, and C. Heiden. Probe calibration in magnetic force microscopy. *Appl. Phys. Lett.*, 57(24):2612–2614, 1990.

[78] *http://www.nanosensors.com/Magnetic_Force_Microscopy.pdf.* July 2010.

[79] G. N. Phillips, M. Siekman, L. Abelmann, and J. C. Lodder. High resolution magnetic force microscopy using focused ion beam modified tips. *Appl. Phys. Lett.*, 81(5):865–867, 2002.

[80] H. Saito, A. van den Bos, L. Abelmann, and J. C. Lodder. High-Resolution MFM: Simulation of Tip Sharpening. *IEEE Trans. Magn.*, 39:3447, 2003.

[81] P. B. Fischer, M. S. Wei, and S. Y. Chou. Ultrahigh-resolution magnetic force microscope tip fabricated using electron-beam lithography. *J. Vac. Sci. Technol., B*, 11(6):2570–2573, 1993.

[82] M. R. Koblischka, U. Hartmann, and T. Sulzbach. Improvements of the lateral resolution of the MFM technique. *Thin Solid Films*, 428:93–97, 2003.

[83] G. Yang, J. Tang, S. Kato, Q. Zhang, L. C. Qin, M. Woodson, J. Liu, J. W. Kim, P. T. Littlehei, C. Park, and O. Zhou. Magnetic nanowire based high resolution magnetic force microscope probes. *Appl. Phys. Lett.*, 87(12):123507, 2005.

[84] H. Kuramochi, T. Uzumaki, M. Yasutake, A. Tanaka, H. Akinaga, and H. Yokoyama. A magnetic force microscope using CoFe-coated carbon nanotube probes. *Nanotechnology*, 16(1):24, 2005.

[85] S. Akita, H. Nishijima, Y. Nakayama, F. Tokumasu, and K. Takeyasu. Carbon nanotube tips for a scanning probe microscope: their fabrication and properties. *J. Phys. D: Appl. Phys.*, 32(9):1044, 1999.

[86] L. Delzeit, C. V. Nguyen, R. Stevens, J. Han, and M. Meyyappan. Growth of carbon nanotubes by thermal and plasma chemical vapour deposition processes and applications in microscopy. *Nanotechnology*, 13(3):280, 2002.

[87] J. H. Hafner, C. L. Cheung, and C. M. Lieber. Growth of nanotubes for probe microscopy tips. *Nature*, 398(6730):761, 1999.

[88] R. M. D. Stevens, N. A. Frederick, B. L. Smith, D. E. Morse, G. D. Stucky, and P. K. Hansma. Carbon nanotubes as probes for atomic force microscopy. *Nanotechnology*, 11(1):1, 2000.

[89] E. Yenilmez, Q. Wang, R. J. Chen, D. Wang, and H. Dai. Wafer scale production of carbon nanotube scanning probe tips for atomic force microscopy. *Appl. Phys. Lett.*, 80(12):2225, 2002.

[90] *http://www.nanosensors.com/Carbon_Nanotube_Probes.pdf*. July 2010.

[91] M. Kläui, H. Ehrke, U. Rüdiger, T. Kasama, R. E. Dunin-Borkowski, D. Backes, L. J. Heyderman, C. A. F. Vaz, J. A. C. Bland, G. Faini, E. Cambril, and W. Wernsdorfer. Direct observation of domain-wall pinning at nanoscale constrictions. *Appl. Phys. Lett.*, 87(10):102509, 2005.

[92] D. A. Allwood, G. Xiong, M. D. Cooke, C. C. Faulkner, D. Atkinson, N. Vernier, and R. P. Cowburn. Submicrometer ferromagnetic NOT gate and shift register. *Science*, 296(5575):2003–2006, 2002.

[93] T. Yamaoka, K. Watanabe, Y. Shirakawabe, K. Chinone, Saitoh E., and Miyajima H. Observations of single magnetic domain wall in nanomagnet by magnetic force microscopy. *Jap. J. Appl. Phys.*, 45:2230–2233, 2006.

[94] P. Banerjee, F. Wolny, D.V. Pelekhov, M.R. Herman, K.C. Fong, U. Weissker, T. Mühl, Y. Obukhov, A. Leonhardt, B. Büchner, and P.C. Hammel. Magnetization reversal in an individual 25 nm iron-filled carbon nanotube. *Appl. Phys. Lett.*, 96:252505, 2010.

[95] B. C. Stipe, H. J. Mamin, T. D. Stowe, T. W. Kenny, and D. Rugar. Magnetic dissipation and fluctuations in individual nanomagnets measured by ultrasensitive cantilever magnetometry. *Phys. Rev. Lett.*, 86(13):2874, 2001.

[96] L. Gunther and B. Barbara. Quantum tunneling across a domain-wall junction. *Phys. Rev. B*, 49(6):3926–3933, 1994.

[97] A. Garg. Escape-field distribution for escape from a metastable potential well subject to a steadily increasing bias field. *Phys. Rev. B*, 51(21):15592–15595, 1995.

[98] S. Porthun, L. Abelmann, S. J. L. Vellekoop, J. C. Lodder, and H. J. Hug. Optimization of lateral resolution in magnetic force microscopy. *Appl. Phys. A*, 66:S1185–S11891, 1998.

[99] Andreas Winkler, Thomas Mühl, Siegfried Menzel, Radinka Kozhuharova-Koseva, Silke Hampel, Albrecht Leonhardt, and Bernd Büchner. Magnetic force microscopy sensors using iron-filled carbon nanotubes. *J. Appl. Phys.*, 99(10):104905, 2006.

[100] Andreas Winkler. Herstellungsverfahren für Nanosonden mit gefüllten Kohlenstoff-Nanoröhrchen und deren Charakterisierung. Diploma thesis, Hochschule Mittweida (FH), 2004.

[101] F. Wolny, U. Weissker, T. Mühl, A. Leonhardt, S. Menzel, A. Winkler, and B. Büchner. Iron-filled carbon nanotubes as probes for magnetic force microscopy. *J. Appl. Phys.*, 104(6):064908, 2008.

[102] T. D. Yuzvinsky, A. M. Fennimore, W. Mickelson, C. Esquivias, and A. Zettl. Precision cutting of nanotubes with a low-energy electron beam. *Appl. Phys. Lett.*, 86(5):053109, 2005.

[103] J. H. Hafner, C. L. Cheung, T. H. Oosterkamp, and C. M. Lieber. High-yield assembly of individual single-walled carbon nanotube tips for scanning probe microscopies. *J. Phys. Chem. B*, 105(4):743, 2001.

[104] M. Löffler, U. Weissker, T. Mühl, T. Gemming, and B. Büchner. Robust determination of Young's modulus of individual carbon nanotubes by quasi-static interaction with Lorentz forces. *Ultramicroscopy*, 111(2):155–158, 2011.

[105] C. Bran, A. B. Butenko, N. S. Kiselev, U. Wolff, L. Schultz, O. Hellwig, U. K. Rößler, A. N. Bogdanov, and V. Neu. Evolution of stripe and bubble domains in antiferromagnetically coupled $[(Co/Pt)_8/Co/Ru]_{18}$ multilayers. *Phys. Rev. B*, 79(2):024430, 2009.

[106] F. Schäffel, C. Kramberger, M. H. Rümmeli, R. Kaltofen, D. Grimm, A. Grüneis, E. Mohn, T. Gemming, T. Pichler, B. Büchner, B. Rellinghaus, and L. Schultz. Carbon nanotubes grown from individual gas phase prepared iron catalyst particles. *phys. stat. sol. (a)*, 204(6):1786–1790, 2007.

[107] K. L. Babcock, L. Folks, R. Street, R. C. Woodward, and D. L. Bradbury. Evolution of magnetic microstructure in high-coercivity permanent magnets imaged with magnetic force microscopy. *J. Appl. Phys.*, 81(8):4438–4440, 1997.

[108] Romel D. Gomez, Edward R. Burke, and Isaak D. Mayergoyz. Magnetic imaging in the presence of external fields: Technique and applications. *J. Appl. Phys.*, 79(8):6441–6446, 1996.

[109] T. Weis, I. Krug, D. Engel, A. Ehresmann, V. Hoink, J. Schmalhorst, and G. Reiss. Characterization of magnetic force microscopy probe tip remagnetization for measurements in external in-plane magnetic fields. *J. Appl. Phys.*, 104(12):123503–4, 2008.

[110] S. Y. Suck, V. Neu, U. Wolff, S. Bahr, O. Bourgeois, and D. Givord. Magnetic force microscopy analysis of magnetization reversal in exchange-biased Co/CoO nanostructure arrays. *Appl. Phys. Lett.*, 95(16):162503, 2009.

[111] F. Wolny, T. Mühl, U. Weissker, A. Leonhardt, U. Wolff, D. Givord, and B. Büchner. Magnetic force microscopy measurements in external magnetic fields - comparison between coated probes and an iron filled carbon nanotube probe. *J. Appl. Phys.*, 108:013908, 2010.

[112] M. V. Rastei, M. Abes, J. P. Bucher, A. Dinia, and V. Pierron-Bohnes. Field-dependent behavior of a magnetic force microscopy tip probed by means of high coercive nanomagnets. *J. Appl. Phys.*, 99(8):084316–6, 2006.

[113] K. L. Babcock, V. B. Elings, J. Shi, D. D. Awschalom, and M. Dugas. Field-dependence of microscopic probes in magnetic force microscopy. *Appl. Phys. Lett.*, 69(5):705–707, 1996.

[114] A. Carl, J. Lohau, S. Kirsch, and E. F. Wassermann. Magnetization reversal and coercivity of magnetic-force microscopy tips. *J. Appl. Phys.*, 89(11):6098, 2001.

[115] T. Wang, Y. Wang, Y. Fu, T. Hasegawa, F. S. Li, H. Saito, and S. Ishio. A magnetic force microscopy study of the magnetic reversal of a single fe nanowire. *Nanotechnology*, 20(10):105707, 2009.

[116] H. Fangohr, T. Fischbacher, M. Franchin, G. Bordignon, J. Generowicz, A. Knittel, and M. Walter. Nmag user manual, http://nmag.soton.ac.uk/nmag/0.1/manual/manual.pdf. Technical report, University of Southhampton.

[117] T. Fischbacher, M. Franchin, G. Bordignon, and H. Fangohr. A systematic approach to multiphysics extensions of finite-element-based micromagnetic simulations: Nmag. *IEEE Trans. Magn.*, 43(6):2896–2898, 2007.

[118] L. D. Landau and E. M. Lifshitz. Theory of the dispersion of magnetic permeability in ferromagnetic bodies. *Phys. Z. Sowietunion*, 8:153, 1935.

[119] T. L. Gilbert. Lagrangian formulation of the gyromagnetic equation of the magnetization field. *Phys. Rev.*, 100:1243, 1955.

[120] O. Ertl, T. Schrefl, D. Suess, and M.E. Schabes. Influence of the Gilbert damping constant on the flux rise time of write head fields. *J. Magn. Magn. Mater.*, 290-291:518, 2005.

[121] F. Ott, T. Maurer, G. Chaboussant, Y. Soumare, J. Y. Piquemal, and G. Viau. Effects of the shape of elongated magnetic particles on the coercive field. *J. Appl. Phys.*, 105(1):013915, 2009.

[122] T. Alvarez, S. V. Kalinin, and D. A. Bonnell. Magnetic-field measurements of current-carrying devices by force-sensitive magnetic-force microscopy with potential correction. *Appl. Phys. Lett.*, 78:1005, 2001.

[123] R. Yongsunthon, J. McCoy, and E. D. Williams. Calibrated magnetic force microscopy measurement of current-carrying lines. *J. Vac. Sci. Technol., A*, 19(4):1763–1768, 2001.

[124] F. Wolny, T. Mühl, U. Weissker, K. Lipert, J. Schumann, A. Leonhardt, and B. Büchner. Iron filled carbon nanotubes as novel monopole-like sensors for quantitative magnetic force microscopy. *Nanotechnology*, 21(43):435501, 2010.

[125] S. Vock, F. Wolny, T. Mühl, R. Kaltofen, L. Schultz, B. Büchner, C. Hassel, J. Lindner, and V. Neu. Monopole-like probes for quantitative magnetic force microscopy: calibration and application. *Appl. Phys. Lett.*, 97:252505, 2010.

[126] C. Hassel, M. Brands, F. Y. Lo, A. D. Wieck, and G. Dumpich. Resistance of a single domain wall in $(Co/Pt)_7$ multilayer nanowires. *Phys. Rev. Lett.*, 97(22):226805, 2006.

[127] H. Stillrich, C. Menk, R. Fromter, and H. P. Oepen. Magnetic anisotropy and spin reorientation in Co/Pt multilayers: Influence of preparation. *J. Magn. Magn. Mater.*, 322:1353, 2010.

[128] F. Wolny, Y. Obukhov, T. Mühl, U. Weissker, S. Philippi, A. Leonhardt, P. Banerjee, A. Reed, G. Xiang, R. Adur, I. Lee, A. Hauser, F. Yang, D. V. Pelekhov, B. Büchner, and P. C. Hammel. Quantitative magnetic force microscopy on permalloy dots using an iron filled carbon nanotube probe. *Ultramicroscopy*, 2011. doi:10.1016/j.ultramic.2011.05.002.

[129] C. L. Degen, M. Poggio, H. J. Mamin, C. T. Rettner, and D. Rugar. Nanoscale magnetic resonance imaging. *Proceedings of the National Academy of Sciences of the United States of America*, 106(5):1313–1317, 2009.

[130] L. Sun, F. Banhart, A. V. Krasheninnikov, J. A. Rodriguez-Manzo, M. Terrones, and P. M. Ajayan. Carbon nanotubes as high-pressure cylinders and nanoextruders. *Science*, 312(5777):1199–1202, 2006.

LIST OF PUBLICATIONS

Publications

1. **F. Wolny**, U. Weissker, T. Mühl, A. Leonhardt, S. Menzel, A. Winkler and B. Büchner, *Iron-filled carbon nanotubes as probes for magnetic force microscopy*, J. Appl. Phys. **104**, 064908 (2008).

2. U. Weissker, M. Löffler, **F. Wolny**, M. U. Lutz, N. Scheerbaum, R. Klingeler T. Gemming, T. Mühl, A. Leonhardt and B. Büchner, *Perpendicular magnetization of long iron carbide nanowires inside carbon nanotubes due to magnetocrystalline anisotropy*, J. Appl. Phys **106**, 054909 (2009).

3. **F. Wolny**, U. Weissker, T. Mühl, M. U. Lutz, C. Müller, A. Leonhardt and B. Büchner, *Stable magnetization of iron filled carbon nanotube MFM probes in external magnetic fields*, J. Phys.: Conf. Ser. **200**, 112011 (2010).

4. M.U. Lutz, U. Weissker, **F. Wolny**, C. Müller, M. Löffler, T. Mühl, A. Leonhardt, B. Büchner and R. Klingeler, *Magnetic properties of α-Fe and Fe_3C nanowires*, J. Phys.: Conf. Ser. **200**, 72062 (2010).

5. **F. Wolny**, T. Mühl, U. Weissker, A. Leonhardt, U. Wolff, D. Givord and B. Büchner, *Magnetic force microscopy measurements in external magnetic fields - comparison between coated probes and an iron filled carbon nanotube probe*, J. Appl. Phys. **108**, 013908 (2010).

6. P. Banerjee, **F. Wolny**, D. Pelekhov, M.R. Herman, K.C. Fong, U. Weissker, T. Mühl, Y. Obukhov, A. Leonhardt, B. Büchner and P. Hammel, *Magnetization reversal in an individual 25 nm iron-filled carbon nanotube*, Appl. Phys. Lett. **96**, 252505 (2010).

7. **F. Wolny**, T. Mühl, U. Weissker, K. Lipert, J. Schumann, A. Leonhardt and B. Büchner, *Iron filled carbon nanotubes as novel monopole-like sensors for quantitative magnetic force microscopy*, Nanotechnology **21**, 435501 (2010).

8. K. Lipert, S. Bahr, **F. Wolny**, P. Atkinson, U. Weissker, T. Mühl, O. Schmidt, B. Büchner and R. Klingeler, *An individual iron nanowire-filled carbon nanotube probed by micro-Hall magnetometry*, Appl. Phys. Lett. **97**, 212503 (2010).
9. S. Vock, **F. Wolny**, T. Mühl, R. Kaltofen, L. Schultz, B. Büchner, C. Hassel, J. Lindner and V. Neu. *Monopole-like probes for quantitative magnetic force microscopy: calibration and application*, Appl. Phys. Lett. **97**, 252505 (2010).
10. **F. Wolny**, Y. Obukhov, T. Mühl, U. Weissker, S. Philippi, A. Leonhardt, P. Banerjee, A. Reed, G. Xiang, R. Adur, I. Lee, A. Hauser, F. Yang, D. V. Pelekhov, B. Büchner and P. C. Hammel. *Quantitative magnetic force microscopy on permalloy dots using an iron filled carbon nanotube probe*, Ultramicroscopy, 2011. doi:10.1016/j.ultramic.2011.05.002.

Invited Talks

1. **F. Wolny**, T. Mühl, U. Weissker: *Iron filled carbon nanotubes as probes in magnetic force microscopy*, Forschungszentrum Dresden-Rossendorf, 09.04.2008
2. **F. Wolny**: *Kohlenstoffnanoröhren - Vielfalt in Form und Funktion*, Exhibition "nano and art", Kugelhaus am Wiener Platz, Dresden, 23.09.2009

Conference Contributions

1. **F. Wolny**, T. Mühl, U. Weissker, A. Leonhardt, B. Büchner, *Iron-filled carbon nanotubes as probes for magnetic force microscopy*, DPG Spring Meeting 2008, Berlin, Germany, 25.-29.02.2008
2. **F. Wolny**, T. Mühl, U. Weissker, K. Lipert, A. Leonhardt, B. Büchner, *Iron-filled carbon nanotubes as probes for magnetic force microscopy*, DPG Spring Meeting 2009, Berlin, Germany, 23.-27.03.2009
3. **F. Wolny**, T. Mühl, M. Lutz, C. Müller, A. Leonhardt, B. Büchner, *Stable magnetization of iron filled carbon nanotube MFM probes in external magnetic fields*, International Conference on Magnetism 2009, Karlsruhe, Germany, 26.-31.07.2009
4. **F. Wolny**, T. Mühl, U. Weissker, K. Lipert, S. Vock, J. Schumann, A. Leonhardt, B. Büchner, *Iron filled carbon nanotubes - Novel high resolution high stability probes for quantitative magnetic force microscopy*, DPG Spring Meeting 2010, Regensburg, Germany, 21.-26.03.2010

ACKNOWLEDGEMENTS

I like to thank Prof. Bernd Büchner for the possibility to write my thesis on a promising application of carbon nanostructures at the IFW Dresden. I am very grateful for his guidance and encouragement.

My gratitude goes to Dr. Thomas Mühl, who has been a great supervisor with never-ending optimism and enthusiasm for this topic and always took the time to discuss big and small problems related to my work. I also want to thank him for the thorough proof-reading of this thesis.

I want to thank Dr. Albrecht Leonhardt and Dr. Christine Täschner for their supervision and useful discussions regarding the growth and properties of carbon nanotubes. Many thanks also to all the colleagues in the CVD department for the support and good collaboration.

I would like to thank Prof. P. Chris Hammel for the invitation to the Ohio State University for two fruitful research stays and his willingness to act as a referee. I also thank Palash Banerjee, Yuri Obukhov, Denis Pelekhov and the other members of the research group for the very good cooperation.

Furthermore I thank Uhland Weissker, Matthias Lutz, Silvia Vock, Markus Löffler, Stefan Philippi, Andreas Winkler and Kamil Lipert for their support concerning samples, sample preparation, measurement techniques, proof reading and helpful discussions on CVD, MFM and the physics of FeCNT.

I am also grateful to Dr. Siegfied Menzel, Dr. Joachim Schumann, Dr. Ingolf Mönch, Dr. Hartmut Vinzelberg, Dr. Ulrike Wolff, Dr. Mark H. Rümmeli, Dr. Daniel Grimm, Dr. Volker Neu, Barbara Eichler, Jürgen Wagner and Ronny Schönfelder for their assistance whenever needed.

Thank you also to Kerstin Höllerer and Manja Maluck for their help regarding all administrative questions.

Last but not least, I want to thank my family and friends for their continuous support and understanding.

VERSICHERUNG

Die von Franziska Wolny vorgelegte Arbeit "*Magnetic properties of individual iron filled carbon nanotubes and their application as probes for magnetic force microscopy*" wurde unter der Betreuung von Prof. Dr. B. Büchner am Leibniz Institut für Festkörper- und Werkstoffforschung Dresden angefertigt.

Hiermit versichere ich, dass ich die vorliegende Arbeit ohne unzulässige Hilfe Dritter und ohne Benutzung anderer als der angegebenen Hilfsmittel angefertigt habe. Die aus fremden Quellen direkt oder indirekt übernommenen Gedanken sind als solche kenntlich gemacht. Die Arbeit wurde bisher weder im Inland noch im Ausland in gleicher oder ähnlicher Form einer anderen Prüfungsbehörde vorgelegt. Des Weiteren erkenne ich die Promotionsordnung der TU Dresden an.

....

Dresden, 16. Dezember 2010